

Optical Spectroscopy of a single GaAs Quantum Ring



Hee Dae Kim

Supervised by Prof. Robert A. Taylor

Department of Physics

Doctor of Philosophy

Trinity Term 2013

Abstract

Since their unique structure properties, quantum rings (QRs) structure has been of particular interest for investigating quantum interference which is called neutral charge exciton optical Aharnov-Bohm (AB) effect recently. A delocalized wavefunction around the rim is a prerequisite for the AB effect, but asymmetry and anisotropy seem to have been overlooked in the spectroscopy of QRs. In this thesis, the presence of a localized state in a single GaAs QR has been presented.

The volcano-like ring structure was modelled in cylindrical coordinates ($z = z(r, \phi)$) based on atomic force microscope (AFM) images of uncapped GaAs QRs, where both anisotropy and asymmetry are present. Based on this AFM images, the adiabatic potential $\varepsilon_{e,h}^k(r, \phi)$ can be obtained for the electron and hole separately by solving the vertical part of the Schrödinger equation, where the vertical confinement is represented by the vertical quantum number k to present the presence of localized state.

Polarization resolved spectroscopy of a single QR is investigated to support the localized state. An asymmetric electron-hole exchange interaction leads to a splitting (Δ_{XY}) of the double exciton state ($|\pm 1\rangle$) into two singlet states ($|X, Y\rangle = (|+1\rangle \pm |-1\rangle)/\sqrt{2}$), where two linearly and orthogonally polarized dipoles ($|X\rangle$ and $|Y\rangle$) are defined along the principal axes. Consequently, the strong polarization is strongly supporting the presence of localized state in a single QR.

Also, the micro-photoluminescence and temperature dependence results from a single GaAs QR are presented to show the excited ($X^{N=2}$) and bi-exciton (XX) states of the localised ground state exciton ($X^{N=1}$). Time-resolved studies show that saturation of the $X^{N=1}$ is dominated by fast dissociation of XX and slow intra-relaxation of $X^{N=2}$.

Publications

- *Asymmetry of localized states in a single quantum ring: Polarization dependence of excitons and biexcitons*
H.D. Kim, K. Kyhm, R.A. Taylor, G. Nogues, K.C. Je, E.H. Lee and J.D. Song, Applied Physics Letters **102**, 033112 (2013).
- *Excited exciton and bi-exciton localized states in a single quantum ring*
H.D. Kim, K. Kyhm, R.A. Taylor, A. Nicolet, M. Potemski, G. Nogues, K. C. Je, E. H. Lee and J. D. Song, Applied Physics Letters **103**, 173106 (2013).
- *Aharonov-Bohm effect on irradiation induced bound excitons in individual carbon nanotubes*
J.A. Alexander-Webber, C. Faugeras, P. Kossacki, M. Potemski, X. Wang, H.D. Kim, S.D. Stranks, R.A. Taylor and R.J. Nicholas, Nature Photonics under review (2013).
- *Optical studies on a single GaN nanocolumn containing a single InGaN quantum disk and effect of strain relaxation on the carrier distribution.*
M.J. Holmes, Y.S. Park, X. Wang, C.C.S. Chan, B.P.L. Reid, H.D. Kim, R.A. Taylor, J.H. Warner and J. Luo, Physica Status Solidi C, **9**, 635 (2012).
- *Optical studies of Quantum Dot-like Emission from Localization Centres in In-GaN/GaN Nanorod Array LEDs*
C.C.S. Chan, P.A. Shields, M.J. Holmes, Y. Zhuang, B.P.L. Reid, H.D. Kim, W.E. Allsopp and R.A. Taylor, Physica Status Solidi C, **9**, 635 (2012).
- *Optical studies on a single GaN nanocolumn containing a single InGaN quantum disk*

M.J. Holmes, Y.S. Park, X. Wang, C.C.S. Chan, B.P.L. Reid, H.D. Kim, R.A. Taylor, J.H. Warner and J. Luo, Applied Physics Letters **98**, 251908 (2011).

- *Polarization asymmetry and optical modal gain saturation via carrier-photon interaction in ZnO*

B.J. Kim, H.D. Kim, K.S. Kyhm, C.Y. Cho, Applied Physics Letters **97**, 041115 (2010).

Contents

1	Introduction	1
1.1	Motivation and Introduction	1
1.2	Why the droplet method ?	3
1.3	Einstein coefficient	5
1.4	Fermi's Golden Rule	9
1.5	Basic theory of exciton	10
1.6	Band structure	12
2	Sample Growth and experimental setup	17
2.1	Single GaAs Quantum Ring growth procedure	17
2.2	Grown Single GaAs Quantum Rings and measurement	27
2.3	Experiemntal Setup	31
2.3.1	Time Integrated μ -Photoluminescence	31
2.3.2	Time resolved μ -Photoluminescence	32
3	Polarization dependence of the $k=3$ localized state	37
3.1	Theoretical calculations for the localized state inside a single quantum ring	37
3.2	The Polarization dependence in exciton and biexciton states	48
3.3	Polarization dependent time-resolved photoluminescence (TRPL) in exciton and biexciton states	50
3.4	Chapter Summary	53
4	Excited excitons and biexcitons in localized states in a single quantum ring	55
4.1	Power dependence of $X^{N=1}$, $X^{N=2}$, and XX	57

CONTENTS

4.2	Polarization dependence of $X^{N=1}$, $X^{N=2}$, and XX	61
4.3	GaAs Q-ring PL temperature dependence measurements	63
4.3.1	Temperature dependent PL spectrum	63
4.3.2	Homogeneous linewidth and emission energy variation by temperature dependence	65
4.4	Time-resolved PL between X (N=1), XX and X (N=2)	67
4.5	Chapter Summary	70
5	Optical properties of the k=2 delocalized state	71
5.1	Power dependent micro PL in the k=2 delocalized state	72
5.2	Polarization dependence by power dependence	73
5.3	Polarization dependence on ring size	79
5.4	Conclusion	79
6	Aharnov-Bohm effect in a single QR	81
6.1	Why Aharnov-Bohm oscillation in a single QR	81
6.2	The Aharnov-Bohm oscillation in a localized state $k = 3$	84
6.3	Chapter summary	86
7	Optical properties of other samples	87
7.1	Single Walled Carbon Nanotubes	87
7.1.1	Introduction to single walled carbon nanotubes	87
7.1.2	Micro-photoluminescence of SWCNTs	90
7.1.3	Photoluminescence excitation of SWCNTs	94
7.1.4	Quantum dot confined in single-walled carbon nanotubes	95
7.2	Future work for a single CdSe nanocrystal	97
7.2.1	Theoretical background	99
7.2.2	Single QD micro photoluminescence on a sapphire plate	101
8	Summary of the thesis and future work	103
	References	105

1

Introduction

1.1 Motivation and Introduction

Thanks to the droplet epitaxy, quantum rings (QR) have become an alternative in the study of Aharonov-Bohm (AB) oscillations (1, 2, 3). This has led to quantum ring (QR) structures becoming of great interest for investigating of the optical Aharonov-Bohm (AB) effect (4, 5, 6). While the rotating charge in the shell of a type-II quantum dot (QD) determines the AB oscillation period, the orbital radius difference of the electrons and holes is the crucial parameter in a QR, for which the coupling to the magnetic flux is of opposite sign (7, 8). Nevertheless, the individual behaviour of each of the particles is not clear in a QR; either the radius is larger or one of them is localised as in the case of a type-II QD (9, 10).

Recent measurements have shown that the morphology of a QR is anisotropic, where the rim height is not constant around the azimuthal angle (13, 14). In the case of this so-called volcano-like structure (15), the azimuthal quantum number is no longer valid, and the wavefunction in the anisotropic QR can be either localised or delocalised through tunneling (16). The presence of localised states was addressed due to height anisotropy in the volcano-like QR morphology (16, 17, 18), and the disorder may cause a threshold magnetic field for AB oscillation, below which the localisation inhibits the rotational quantum coherence (19, 20). Nevertheless, a persistent current (21, 22, 23) can be observed in a QR as evidence of AB-oscillations, when an external magnetic field is large enough to overcome the anisotropy-induced potential barrier or

1. INTRODUCTION

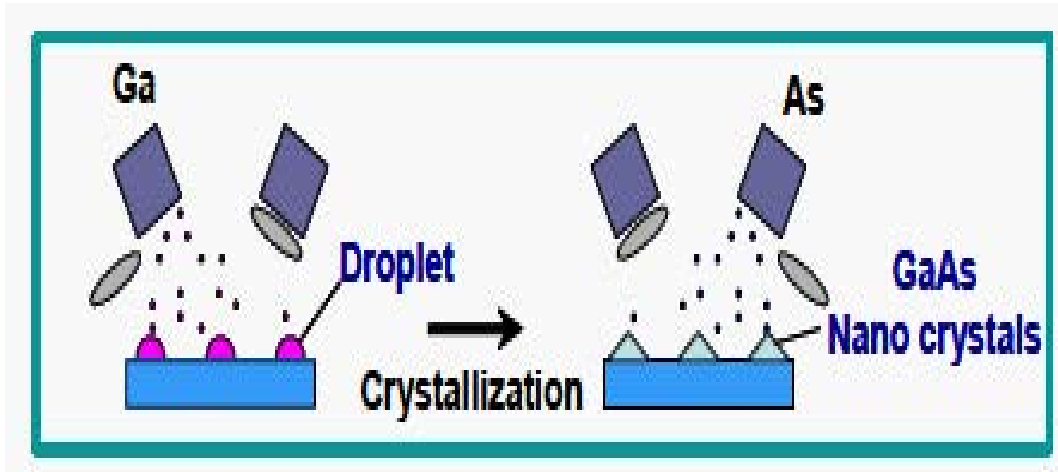


Figure 1.1: Schematic illustration of droplet epitaxy (11)

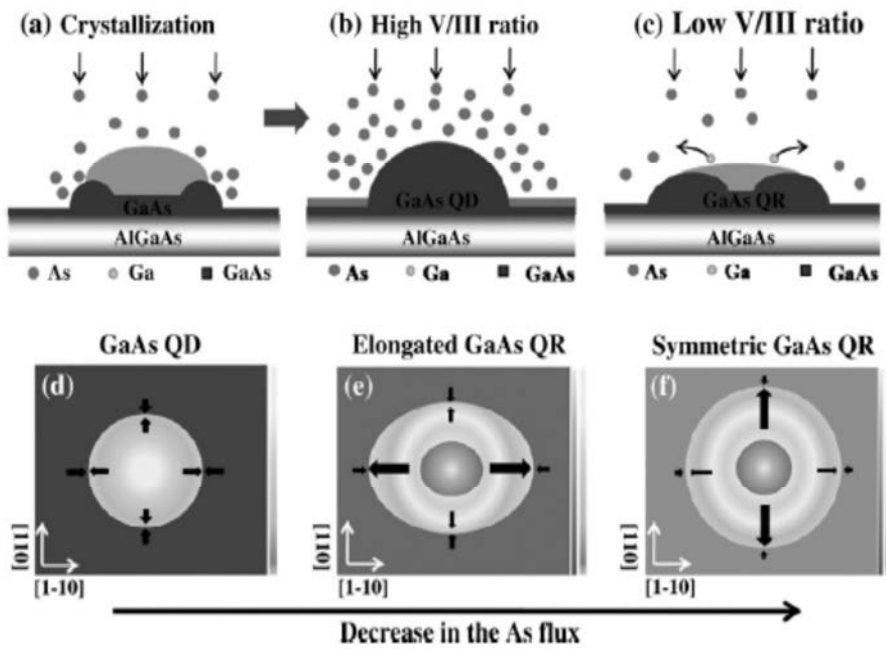


Figure 1.2: Schematic illustration of the formation of various GaAs quantum structures with different As fluxes (12)

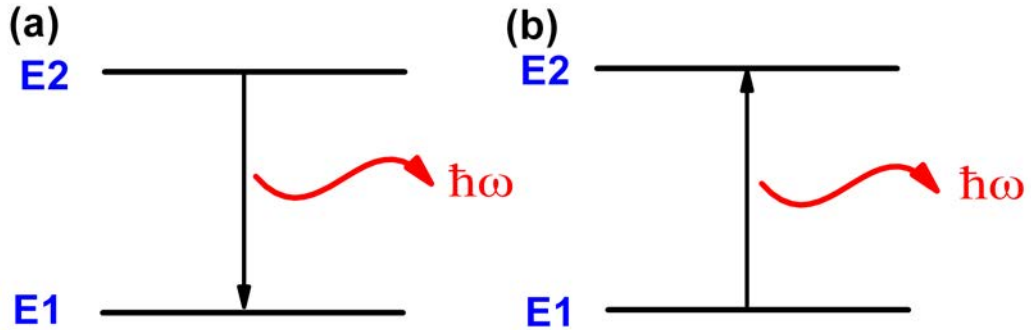


Figure 1.3: Optical transitions between two states (a): Spontaneous emission and (b) absorption

asymmetric exchange interaction (24, 25, 26). Asymmetry and anisotropy seem to have been overlooked in the spectroscopy of QRs (27, 28, 29). In this thesis, the presence of a localised state in a single GaAs/Al_{0.3}Ga_{0.7}As QR is claimed for a volcano-like QR structure, which corresponds to an excited state of the vertical confinement (30). The asymmetry of the localised state is investigated in terms of the polarization dependence of excitons and biexcitons in Chapter 3. Also, the presence of biexcitons and excited exciton states of the localised ground exciton is clarified in terms of their dependence on excitation power, temperature, polarization asymmetry, and time-resolved photoluminescence (PL) in Chapter 4. To investigate the delocalization of exciton states by tunnelling in the asymmetric structure, power dependent time-integrated and time-resolved photoluminescence is investigated at different power densities in Chapter 5 (31, 32, 33).

1.2 Why the droplet method ?

Developments of droplet epitaxy methods enabled the fabrication of various GaAs quantum nanostructures of high optical quality such as quantum dots, single quantum rings, and concentric double quantum rings (34, 35, 36). The droplet epitaxy that Dr. Nobuyuki Koguchi and his collaborators of National Research Institute for Metals (NIMS) invented in 1990 is an excellent self-assembly technique for the fabrication of

1. INTRODUCTION

nanostructures similar to the Stranski-Krastanow (S-K) growth mode (37, 38, 39). Although the S-K growth mode is often used for self-assembly, it can only be applied to lattice-mismatched systems for which the lattice constant of the substrate and that of the nanostructure are different from each other (40, 41). On the other hand, droplet epitaxy can be applied to both lattice-mismatched and lattice-matched systems like GaAs/AlGaAs. The lattice-matched systems are strain free in principle, and able to fabricate nanostructures with a relatively uniform size, a small number of non-radiative recombination sites, and various shapes (42, 43). These properties often help to simplify the interpretation of fundamental optical experiments (44, 45).

Droplet epitaxy consists of two main steps as shown in Fig.1.1. The first step is the fabrication of ultra-fine liquid droplets of a group-3 metal with a low melting point such as Ga and In on a certain substrate by supplying a molecular beam in ultra-high vacuum. The second step is the formation of nanocrystals of the compound semiconductor by irradiation by a molecular beam of a group-5 metal such as As.

Fig.1.2 shows a schematic illustration of the formation of various GaAs quantum structures as the As flux is varied. Fig.1.2 (a) shows conceptually the cross-sectional shape for the crystallization process of a Ga droplet and the change into the GaAs quantum structures during crystallization under the As supply. The crystallization process of the Ga droplets occurs preferentially around the edge region of the Ga droplets. As the GaAs crystal forms in this edge region, it becomes enlarged at the center (11, 27). Because the crystallization process of the edge region of the Ga droplet may be faster than that at the center, the GaAs crystal grows faster at the edge. This result can be explained by the V/III ratio, which effectively influences the GaAs crystallization. When the V/III ratio is relatively large, all the areas of the Ga droplets can be effectively crystallized. Also, the relatively large number of As atoms may block the migration of Ga atoms at the Ga droplets. As a result, the GaAs QDs with a symmetric shape can be formed as shown in Fig.1.2 (b) and (d) (46).

When the V/III ratio is small, the crystallization process may be slower than that for relatively high V/III ratio, because the incorporation rate between Ga and As is small. This slow process results in an increase in the migration probability of the Ga

atoms at the droplet, as schematically described in Fig.1.2 (c) and (e), resulting in formation of GaAs QRs with an asymmetric shape. In previous work on the migration properties of the Ga atoms on the $c(4 \times 4)$ reconstructed GaAs surface, the Ga migration is strongly dependent on the crystal direction. That is, the migration probability of the Ga atoms on the $c(4 \times 4)$ GaAs surface is higher in the $[1\bar{1}0]$ direction than in the $[110]$ direction. Similarly, the migration of the Ga atoms along the $[1\bar{1}0]$ direction for the Ga droplets in this work may also be compared with the $[110]$ direction. As a result, the shape of the GaAs QR can be asymmetric. With a further decrease in As flux, the shape of the asymmetric GaAs QRs becomes symmetric, as shown in Fig.1.2 (f). Because the migration length of the Ga atoms along the $[1\bar{1}0]$ direction reaches a limit, the migration of the Ga atoms toward the $[110]$ direction can be significantly increased, resulting in the formation of relatively symmetric QRs (12).

1.3 Einstein coefficient

Light can be emitted or absorbed whenever a transition in an atom occurs between two different energy states. Absorption happens when the atom moves to a higher energy level, while photon emission occurs when the atom falls down to a lower energy level. These transitions satisfy the energy conservation condition

$$\hbar\omega = E_2 - E_1, \quad (1.1)$$

Where E_2 is the higher energy level and E_1 is the lower energy level. The emission and absorption rates can be calculated by quantum mechanics.

Spontaneous emission is the radiative process by which an electron in a higher energy level states goes down to a lower energy level states. An electron which is in a high energy state is not stable, so this electron has a tendency to change its energy to the lowest state available. Spontaneous emission rates are determined by Einstein A coefficient. This coefficient provides the probability per unit time which the electron in high energy level falls down to the low energy level by photon emission. Therefore, the transition can be described by

1. INTRODUCTION

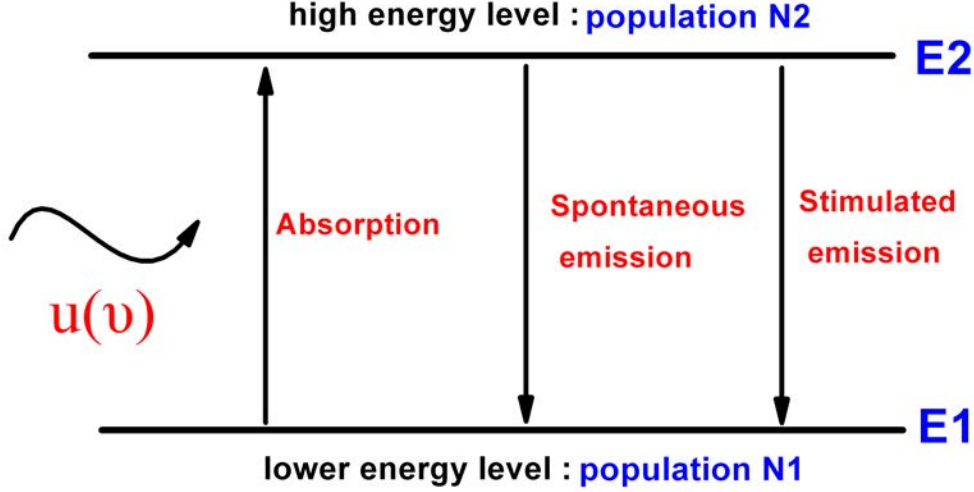


Figure 1.4: Absorption, spontaneous emission and stimulated emission transition between two level energy states with incoming energy density

$$\frac{dN_2}{dt} = -A_{21}N_2, \quad (1.2)$$

where N_2 is the number of atoms in the high energy state and A_{21} is the coefficient governing the transition from energy level E_2 to energy level E_1 in Fig.1.3.

The solution to equation (1.2) is

$$N_2(t) = N_2(0) \exp(-A_{21}t) = N_2(0) \exp\left(\frac{-t}{\tau}\right), \quad (1.3)$$

where

$$\tau = \frac{1}{A_{21}} \quad (1.4)$$

and τ is the radiative lifetime of the excited state.

Absorption occurs in Fig.1.3 (b). The atom moves up from low energy state to high energy state by absorbing a photon. This absorption transition rate per unit time can be expressed as

$$\frac{dN_1}{dt} = -B_{12}^\omega N_1 u(\omega), \quad (1.5)$$

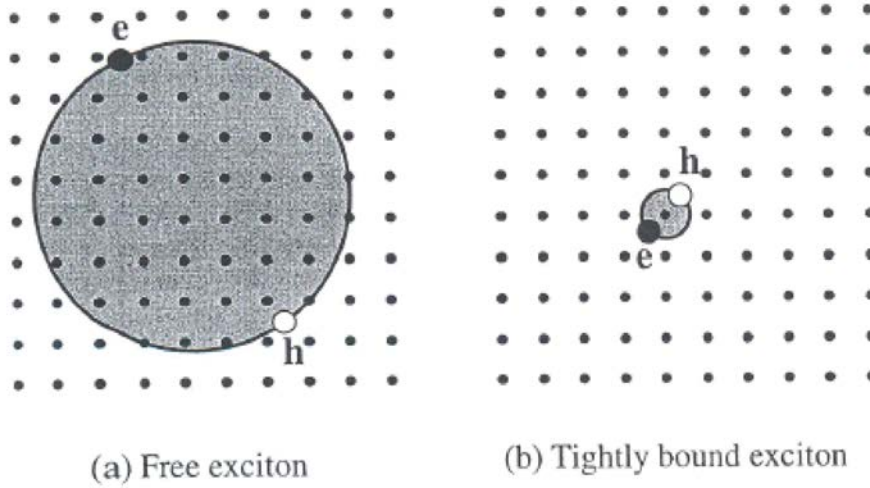


Figure 1.5: (a) a free exciton which is called Wannier-Mott excitons, (b) a tightly bound exciton which is called Frenkel excitons (47)

where $N_1(t)$ is the number of atoms in high energy state, B_{12}^ω is the Einstein coefficient, and $u(\omega)$ is the energy density of the electromagnetic field.

Einstein discovered that a third type of transition is needed, known as stimulated emission in order to understand the transition processes. In Fig.1.4, all possible optical transitions between the two different energy levels including this stimulated emission are shown. In the absorption process, the incoming photon energy can stimulate downward emission transition from high energy state to low energy state. This stimulated-emission can be expressed as

$$\frac{dN_2}{dt} = -B_{21}^\omega N_2 u(\omega), \quad (1.6)$$

where $N_2(t)$ is the number of atoms in low energy state, B_{21}^ω is the Einstein coefficient, and $u(\omega)$ is the energy density of the electromagnetic field.

These three Einstein coefficients are all connected to each other in the transition processes. Under steady-state conditions, the absorption should be balanced by the

1. INTRODUCTION

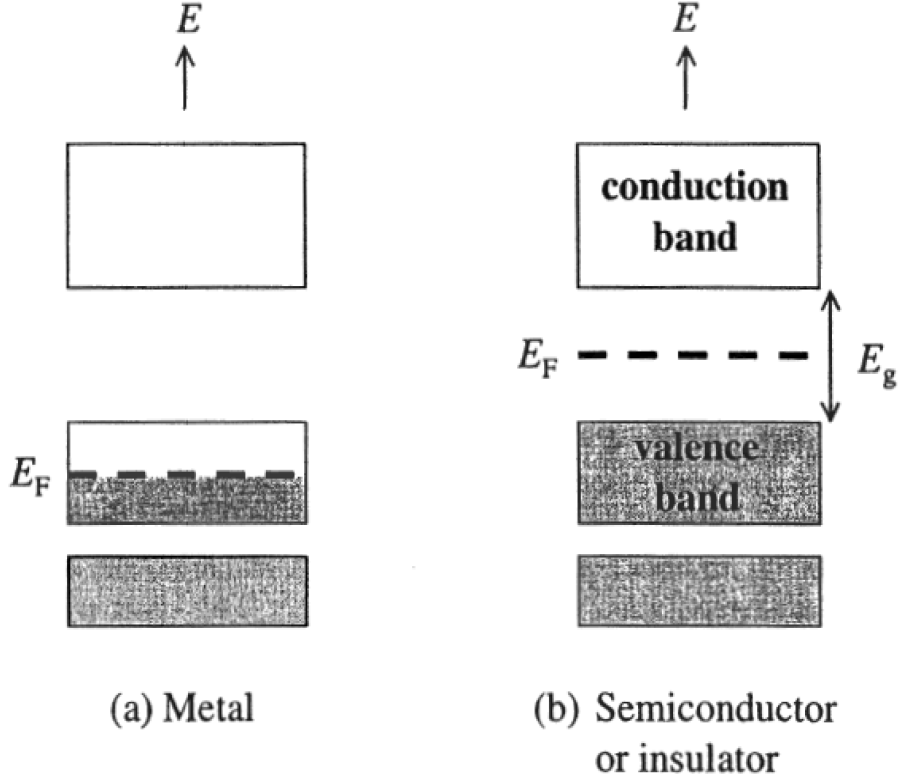


Figure 1.6: Energy level diagrams for (a) metal, and (b) a semi-conductor or insulator. The bands are filled with electrons up to the Fermi level E_F (47).

spontaneous and stimulated emission. Therefore,

$$B_{12}^{\omega} N_1 u(\omega) = A_{21} N_2 + B_{21}^{\omega} N_2 u(\omega), \quad (1.7)$$

From Boltzmann's law, the ratio of N_2 to N_1 is given by

$$\frac{N_2}{N_1} = \frac{g_2}{g_1} \exp\left(-\frac{\hbar\omega}{k_B T}\right), \quad (1.8)$$

where g_1 and g_2 are degeneracies of level 1 and 2. The energy density is also give by the Planck formula

$$u(\omega) = \frac{\hbar\omega^3}{\pi^2 c^3} \frac{1}{\exp\left(\frac{\hbar\omega}{k_B T}\right) - 1}, \quad (1.9)$$

under these conditions, the relationships of the Einstein coefficients are solved by

$$g_1 B_{12}^\omega = g_2 B_{21}^\omega, \quad (1.10)$$

$$A_{21} = \frac{\hbar\omega^3}{\pi^2 c^3} B_{21}^\omega, \quad (1.11)$$

so, we can understand that a high absorption probability will give a high emission probability, and also the relationship between spontaneous and stimulation emission by means of the Einstein coefficients.

1.4 Fermi's Golden Rule

The absorption transition coefficient $c_m(t)$,

$$c_m(t) = \frac{\langle \phi_m | H_I | \phi_n \rangle}{\hbar\omega_{mn}} \frac{e^{i(\omega_{mn}-\omega)t} - 1}{\omega_{mn} - \omega}, \quad (1.12)$$

$\hbar\omega = \hbar\omega_{mn} = E_m - E_n$, $E_m = E_n + \hbar\omega$, so equation (1.27) give us transition coefficient from Energy E_n to Energy E_m with absorption energy $\hbar\omega$.

The emission transition coefficient $c_m(t)$,

$$c_m(t) = - \frac{\langle \phi_m | H_I | \phi_n \rangle}{\hbar\omega_{mn}} \frac{e^{i(\omega_{mn}+\omega)t} - 1}{\omega_{mn} + \omega}, \quad (1.13)$$

$E_m = E_n - \hbar\omega$, so equation (1.28) give us transition coefficient from Energy E_n to Energy E_m with emission energy $\hbar\omega$.

Therefore, the absorption and emission transition probability density is

$$P_{n \rightarrow m} = |c_n(t)|^2 = \frac{|\langle \phi_m | H_I | \phi_n \rangle|^2}{\hbar^2} \frac{\sin^2[(\omega_{mn} \pm \omega)t/2]}{[(\omega_{mn} \pm \omega)/2]^2}, \quad (1.14)$$

At large times $t \rightarrow \infty$

$$\frac{|\langle \phi_m | H_I | \phi_n \rangle|^2}{\hbar^2} \frac{\sin^2[(\omega_{mn} \pm \omega)t/2]}{[(\omega_{mn} \pm \omega)/2]^2} \approx 2\pi\hbar t \delta(E_m - E_n \pm \hbar\omega), \quad (1.15)$$

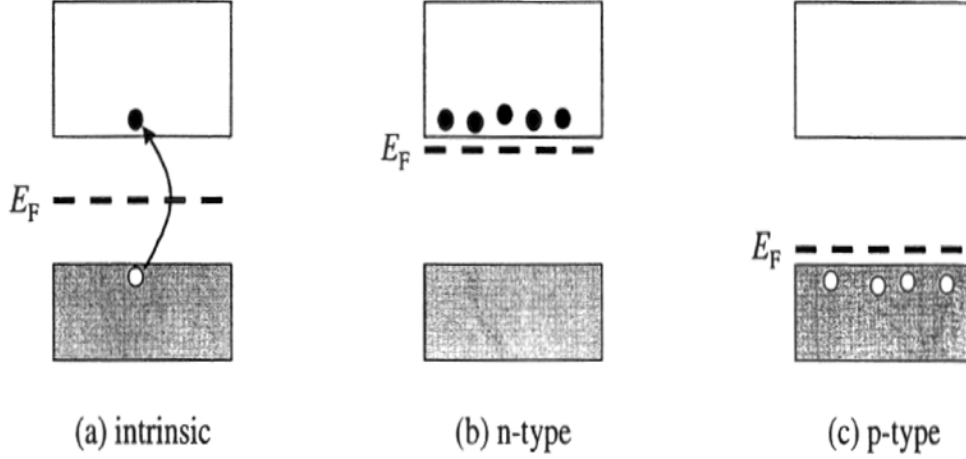


Figure 1.7: Valence and conduction bands for : (a) intrinsic semiconductor, (b) a semiconductor with n-type doping, and (c) a semiconductor with p-type doping(47).

So, the transition probability density is

$$R_{n \rightarrow m} = \frac{|c_n(t)|^2}{t} = \frac{2\pi}{\hbar} |\langle \phi_m | H_I | \phi_n \rangle|^2 \delta(E_m - E_n \pm \hbar\omega), \quad (1.16)$$

$R_{n \rightarrow m}$ is called the transition probability per unit time or transition rate. Formula (1.16) satisfies the energy conservation law and is called Fermi's Golden Rule.

1.5 Basic theory of exciton

The absorption of a photon in a semiconductor creates an electron in the conduction band and a hole in the valence band. The oppositely charged particles can attract each other through their Coulomb interaction. This attractive interaction makes an electron-hole pair. Also, if the right conditions are satisfied, a bound electron-hole pair can be formed. This neutral bound pair is called an exciton.

Normally, There are two basic types of exciton : Wannier-Mott excitons, called free excitons and Frankel excitons, called tightly bound excitons. The two different kinds of excitons are showed in Fig.1.5. The Wannier-Mott type excitons have a large radius, and they are delocalized states that can move freely. By contrast, Frenkel excitons

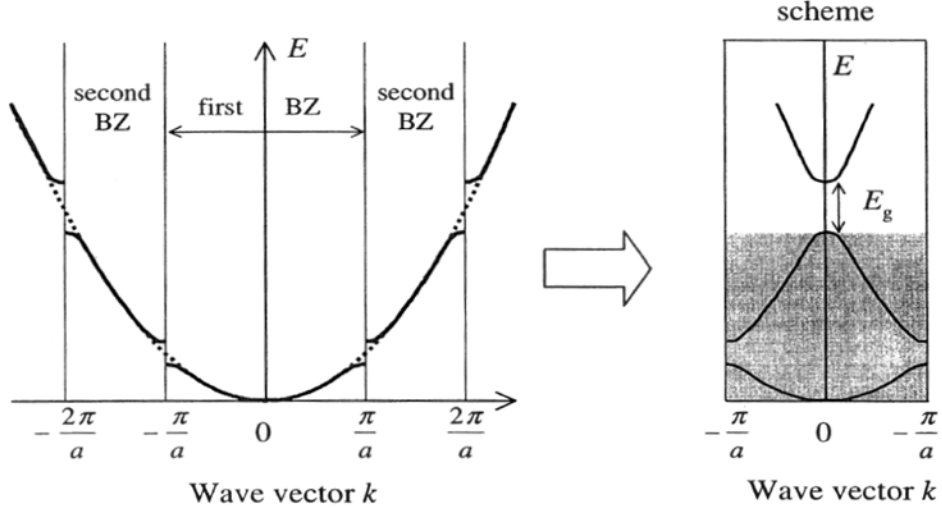


Figure 1.8: Band structure of a simple solid with a lattice constant of a . The left hand side of the figure shows the $E-k$ relationship across several Brillouin zones, while the right hand side replots the same band structure in the reduced zone. The dotted line indicates the parabolic dispersion of free electrons(47).

have a much smaller radius which is comparable to the size of the unit cell. This makes them localized states which are tightly bound to specific atoms or molecules. Tightly bound excitons are much less mobile than free excitons. In applying the Bohr model to the exciton, the electron and hole are moving through a medium with a high dielectric constant ϵ_r . The bound states are characterized by the principal quantum number n . The energy of the n th level relative to the ionization limit is given by

$$E(n) = - \frac{\mu}{m_0} \frac{1}{\epsilon_r^2} \frac{R_H}{n^2} = - \frac{R_X}{n^2}, \quad (1.17)$$

where R_H is the Rydberg constant of the hydrogen atom ($\sim 13.6\text{eV}$). The quantity $R_X = (\frac{\mu}{m_0 \epsilon_r^2}) R_H$, reduced mass μ which is deduced by

$$\frac{1}{\mu} = \frac{1}{m_e^*} - \frac{1}{m_h^*}, \quad (1.18)$$

The radius of the electron-hole orbit is given by

$$r_n = \frac{m_0}{\mu} \epsilon_r n^2 a_H = n^2 a_X, \quad (1.19)$$

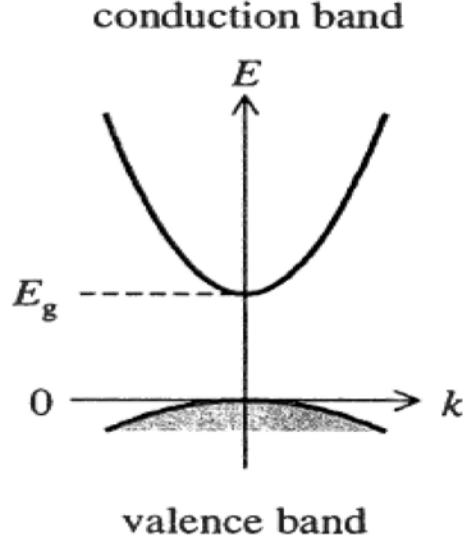


Figure 1.9: Band dispersion of a semiconductor or insulator near top of the valence band and the bottom of the conduction band(47).

where a_H is the Bohr radius of the hydrogen atom ($5.29 \times 10^{-11}\text{m}$) and $a_X = (\frac{m_0\epsilon_r}{\mu})a_H$ is the exciton Bohr radius. Generally, R_X tends to increase and a_X to decrease as E_g increases. This is explained by the fact that ϵ_r tends to decrease and μ to decrease as the band gap increases.

1.6 Band structure

A photon energy can be derived by Einstein's relativistic relation form $E^2 = p^2c^2 + m^2c^4$. The photon energy is $E = pc$ because a photon mass is 0. A electron energy is derived from electron's Schrödinger equation. The time-independent Schrödinger equation,

$$[-\frac{\hbar^2}{2m} \nabla^2 + V(r)]\psi(r) = E\psi(r) \quad (1.20)$$

where E , r , m , $\psi(r)$ are the particle's energy, position, mass and spatial wavefunction, $V(r)$ is the potential, ∇^2 is the Laplacian and \hbar is the reduced Planck's constant. Alternatively, this expression can be showed as an eigen-problem $H\psi(r) = E\psi(r)$ with the Hamiltonian H acting like eigen-operator, E as the eigen-value and $\psi(r)$ as the

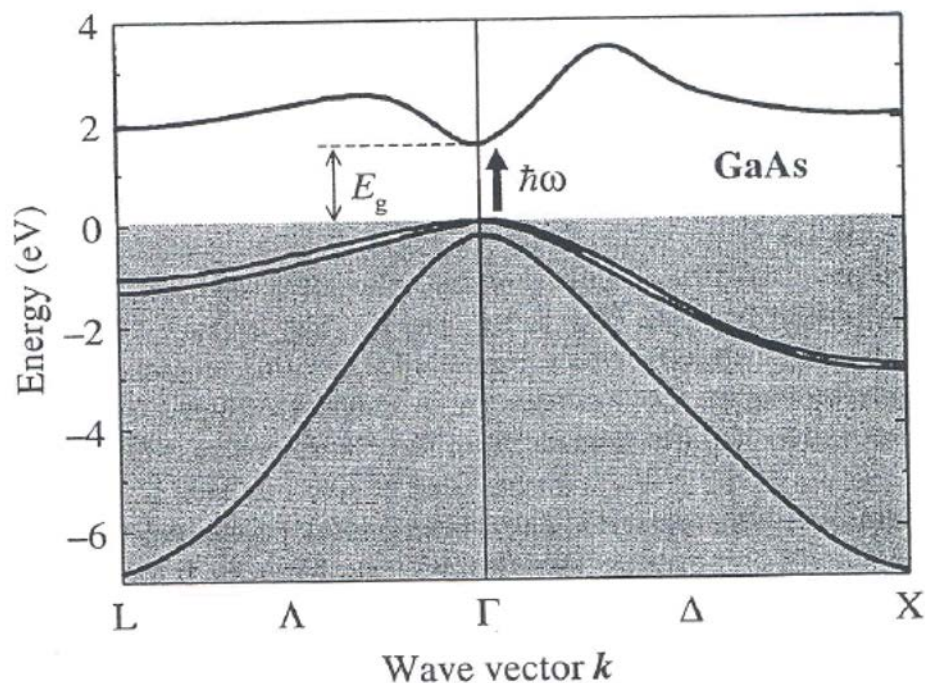


Figure 1.10: Band structure of GaAs. The valence bands are below the Fermi level and are full of electrons(47).

eigen-state. The free electron model gives us a solution of the equation, as eigen-state $\psi(r, t) = Ae^{ik \cdot r} e^{iEt/\hbar}$ and as eigen-value $E = \hbar^2 k^2 / 2m$ (where k is the wave vector and $|L| = 2\pi/\lambda$).

Fig.1.6(a) shows a energy diagram of a metal. These have an odd number of electrons per atom, which indicates that the highest occupied band will only be half full. The Fermi energy will lie in the middle of the highest occupied band. Electrons with energy just below E_F can easily be excited to empty states above E_F . Fig.1.6(b) indicates the energy diagram of a semiconductor. These have an even number of electrons per atom, and the highest occupied band is full of electrons. This highest occupied band is called the valence band, while the lowest unoccupied band is called the conduction band. The Fermi level lies somewhere within the energy gap between the valence and conduction bands. The first empty states for the electrons are in the conduction band, and it requires a minimum amount of energy equal to the band gap E_g to excite the electrons to available states. Therefore, semiconductors and insulators have much lower

1. INTRODUCTION

electrical conductivities than metal. Also, the difference between an insulator and a semiconductor is related to the size of band gap. Semiconductors have smaller band gaps than insulators. This makes it possible that a significant number of electrons are excited thermally from the valence band to the conduction band at room temperature.

Fig.1.7 shows the conduction and valence bands of a semiconductor. Fig.1.7(a) indicates a pure intrinsic semiconductor. The Fermi level lies about half between the two bands. The thermal excitation of an electron to the conduction band makes the empty space (hole) in the valence band. Fig.1.7(b) shows n-typed doping semiconductor. The impurities give one extra electron for each dopant atom. These extra electrons lie in donor levels, the electron states are filled up to the donor levels. So the Fermi energy should be lain very close to the donor level energies. The electrons in the donor levels can be easily excited into the conduction band. Fig.1.7(c) shows p-type doping semiconductor. In contrast to n-type semiconductors, p-type semiconductors have a larger hole concentration than electron concentration. In p-type semiconductors, holes are the majority carriers and electrons are the minority carriers in Fig.1.7(c). The Fermi energy level lies closer to the valence band than the conduction band.

If the electrons are moving completely free, the $E - k$ dispersion is governed by $E = \hbar^2 k^2 / 2m$, where $p = h/\lambda_e$ is the momentum of the electron, λ_e being the de-Broglie wavelength of the electron. In a crystal, the electrons are not really free, so $E - k$ dispersion should be modified. The valence electrons are released from their atoms and move through the crystal. This leaves behind a regular lattice of positively charged ions. The potential of the ion cores perturbs the motion of the electrons and changes the $E - k$ relationship. This modified $E - k$ relationship is called by nearly free electron model. Fig.1.8 indicates the typical band structure of a simple crystal. The $E - k$ diagram is divided by different Brillouin zones with reciprocal lattice vector G . The dotted line in the Fig.1.8 shows the band dispersion for free electrons, meanwhile the solid line shows the band dispersion for the nearly free electrons. The periodic lattice potential causes Bragg scattering of the electron waves. The scattering amplitude is small except in the region close to a Brillouin zone boundary. Therefore, the band dispersion departs significantly from that of free electrons near a zone boundary.

The band dispersion near $k = 0$ for a semiconductor or insulator is shown in more detail in Fig.1.9. The top valence band and the lowest conduction band states are shown in Fig.1.9. The bands are parabolic for small k , and dispersions given by

$$E_c(k) = E_c + \frac{\hbar^2 k^2}{2m_e^*} \quad (1.21)$$

$$E_v(k) = - \frac{\hbar^2 k^2}{2m_h^*} \quad (1.22)$$

where $E = 0$ corresponds to the top of the valence band. Equ.1.21 and 1.22 show the effective mass m_e^* and m_h^* of each band can determine the band dispersion. In general, the effective mass can be defined by the curvature of the $E - k$ diagram according to

$$m^* = \hbar^2 \left(\frac{d^2 E}{dk^2} \right)^{-1} \quad (1.23)$$

The effective mass is a band structure parameter as a consequence of the perturbation of the periodic lattice potential. The negative curvature of the valence band means a hole state. Electrons in the conduction band behave like negative particles of mass m_e^* , while the holes in the valence band behave like positive particles of mass m_h^* . Especially, Fig.1.10 shows band structure of GaAs.

1. INTRODUCTION

2

Sample Growth and experimental setup

2.1 Single GaAs Quantum Ring growth procedure

The samples were grown at Korea Institute of Science and Technology (KIST) and the sample growth procedure was given by Dr. J. D. Song and E. H. Lee. In this chapter, all growth of GaAs QRs on an $\text{Al}_{0.3}\text{Ga}_{0.7}\text{As}/\text{GaAs}$ substrate will be discussed (48, 49, 50). The growth parameters, such as the beam equivalent flux (BEF) of As_4 , the substrate temperature, the growth interruption time, and the size of Ga droplets, were varied. The structural properties of QRs were investigated by an scanning electron microscope (SEM) and an atomic force microscopy (AFM). The optical properties of QRs were observed by using macro-PL and micro-PL.

The QR samples were grown by the droplet epitaxy (DE) method. After deoxidation at $\sim 600^\circ\text{C}$ under As_4 , a $\sim 100\text{ nm}$ - thick GaAs buffer layer and $\sim 50\text{ nm}$ - thick $\text{Al}_{0.3}\text{Ga}_{0.7}\text{As}$ layer were grown sequentially at 580°C . Then, Ga droplets were formed on the $\text{Al}_{0.3}\text{Ga}_{0.7}\text{As}/\text{GaAs}$ substrate and crystallization by As_4 injection was performed (28, 29). Various parameters for the growth of QRs were changed for observation of the change of surface morphology at each fixed condition. The BEF of As_4 was varied in the range of As_4 $1.2 \times 10^{-7} \sim 1 \times 10^{-5}$ Torr. The substrate temperature at injection of As_4 was changed in the range $257^\circ\text{C} \sim 321^\circ\text{C}$. The change in the QRs was observed with an increase of the interruption time in a sequential injection of As_4 (51, 52). The

2. SAMPLE GROWTH AND EXPERIMENTAL SETUP

2 ML, 0.5 ML/s, 309°C for metal droplets, As_4 X Torr @ near RT

Ga droplets

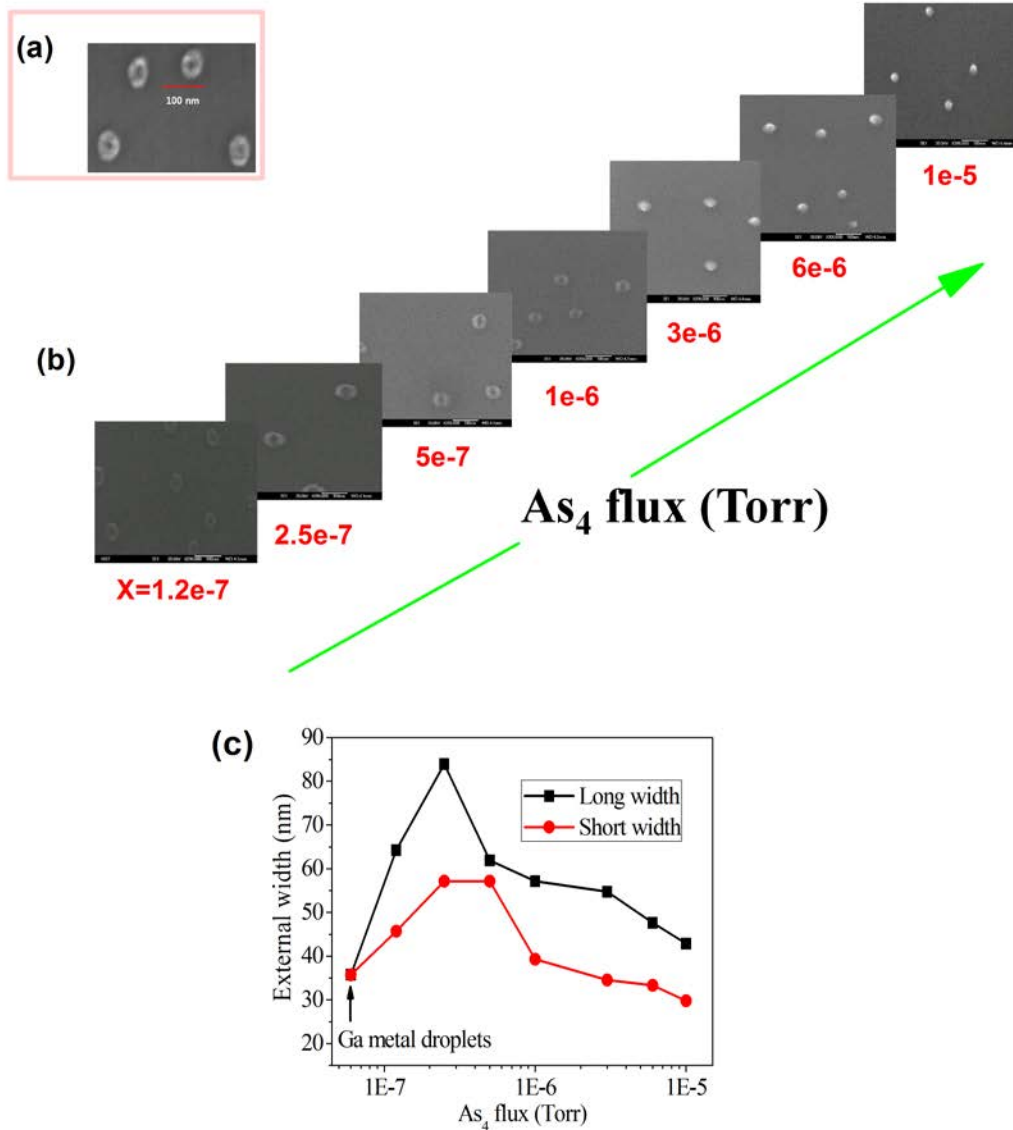


Figure 2.1: (a) SEM image of Ga droplets, (b) SEM images of the evolution of the GaAs nanostructures from QDs to QRs as a function of As_4 BEF. (c) Statistical graphs of the long/short external width of the QRs.

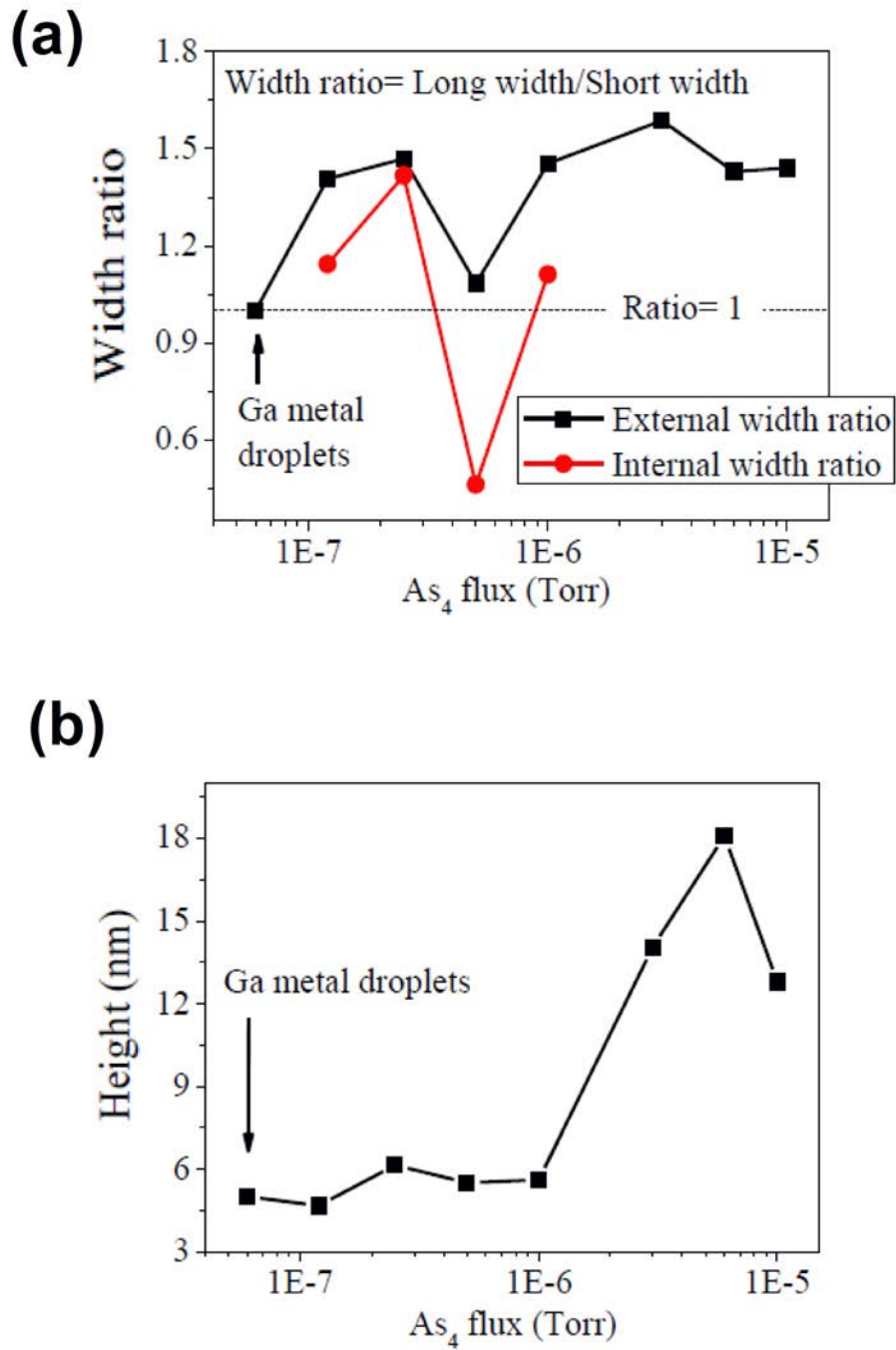


Figure 2.2: (a) the external/internal width ratio and (b) the height of the GaAs nanostructures as a function of As₄ BEF.

2. SAMPLE GROWTH AND EXPERIMENTAL SETUP

interruption time was in the range of 0 s \sim 30s. The flux of As₄ was introduced on two kinds of Ga droplets with different diameters, heights, and densities (53, 54). The surfaces of the Ga droplets and GaAs QRs were observed by an AFM and SEM. The PL of typical GaAs QDs and GaAs QRs, including a DBR structure, was investigated by macro-PL and μ -PL.

Fig.2.1 (a) shows an SEM image of Ga droplets with the growth conditions of $T_s=309^\circ\text{C}$, $F_{Ga}=0.5\text{ML/s}$, and $C_{Ga}=2\text{ML}$. Fig.2.1 (b) presents a change of the surfaces for a change of the BEF at As₄ $1.2\times 10^{-7}\sim 1\times 10^{-5}\text{Torr}$. The As₄ was injected at near room temperature without heating the substrate. With a decrease of the As₄, the shape of the GaAs nanostructures evolved into ring-like structures. Similar results to the formation of QRs have been reported. The critical BEF of As₄ for transformation into rings was $1\times 10^{-6}\text{Torr}$ (55, 56). Fig.2.1 (c) and Fig.2.2 show the statistical trends from the images in Fig.2.1 (a) and (b). Fig.2.1 (c) indicates a change of the external width of the QRs. The long and short external widths of the QRs measured, respectively. In the range of As₄ $1.2\times 10^{-7}\sim 1\times 10^{-6}\text{Torr}$, a slight difference in the trend between long and short external widths was observed. This difference points out that the external shape of the QRs at As₄ $2.5\times 10^{-7}\text{Torr}$ tends to be asymmetrical, compared to other QRs. On the other hand, the external shape of the QRs at As₄ $5\times 10^{-7}\text{Torr}$ was generally symmetrical. Fig.2.2 (a) shows the trends of the external/internal width ratio of GaAs QRs. The external width ratio is (long external width)/(short external width).

The internal width ratio is (internal width along the long external width)/(internal width along the short external width). As shown at Fig.2.2 (a), the internal width ratio of GaAs QRs at a function of As₄ $1.2\times 10^{-7}\text{Torr}$ was less than ~ 0.6 and the external width ratio was nearly 1 (symmetrical external shape). This result indicates that the shape of QRs at a function of As₄ $5\times 10^{-7}\text{Torr}$ is coffee bean-like. The origin of formation of such a shape for the QRs is not clear. However, recently, it has been reported that a relatively low V/III ratio tends to make the external shape of QRs symmetrical. Typically, the migration of Ga atoms along the $[1\bar{1}0]$ direction is preferred for the formation of QRs, compared with the $[110]$ direction (12, 57). Thus, Ga atoms would begin to migrate along the $[110]$, when the migration length of the Ga atoms along the $[1\bar{1}0]$ direction reaches a limit. Based on this process of migration, the

2.1 Single GaAs Quantum Ring growth procedure

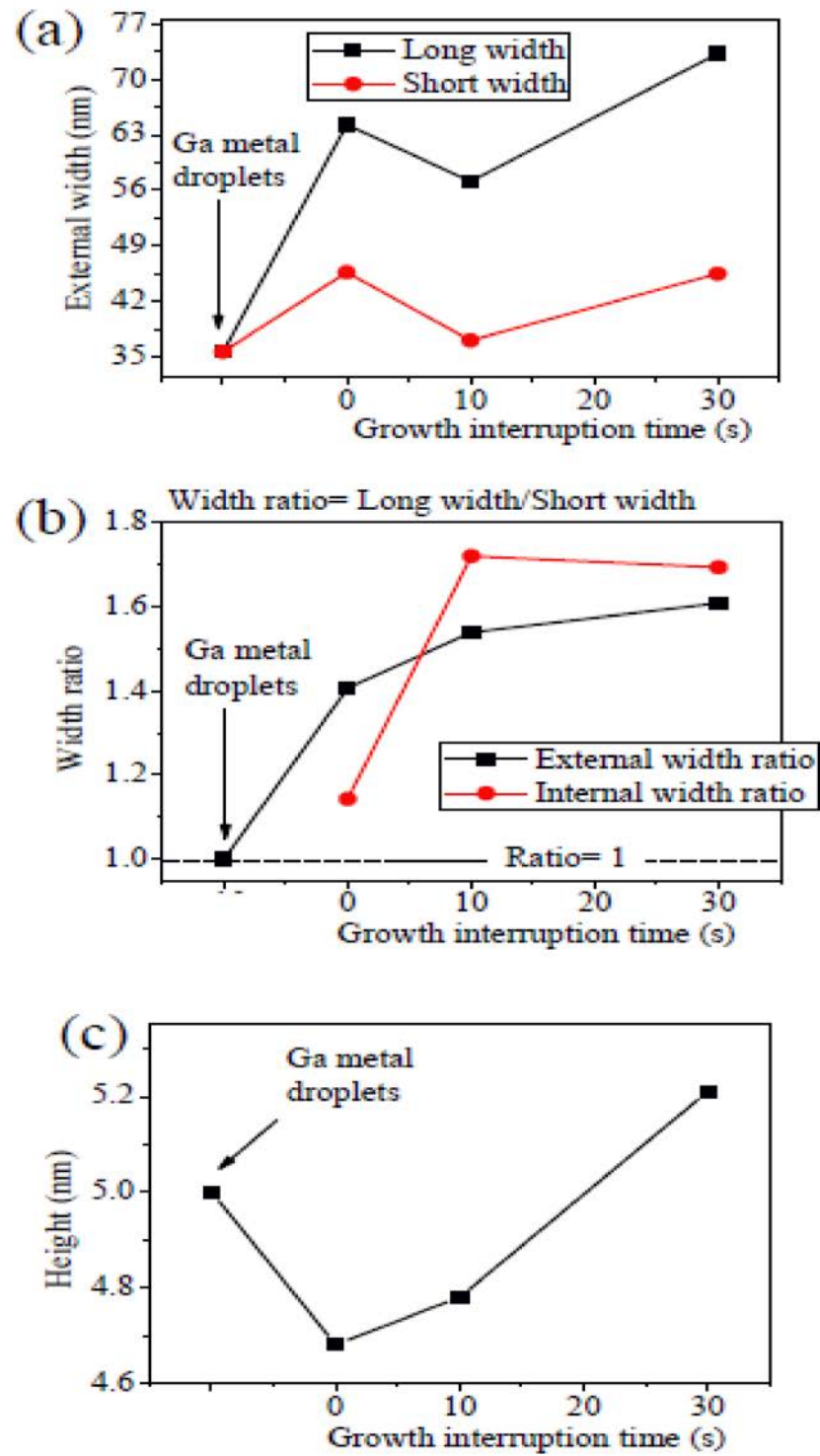


Figure 2.3: Statistical graphs of (a) the long/short external width, (b) the external/internal width ratio, and (c) the height of GaAs QRs for a change of the interruption time.

2. SAMPLE GROWTH AND EXPERIMENTAL SETUP

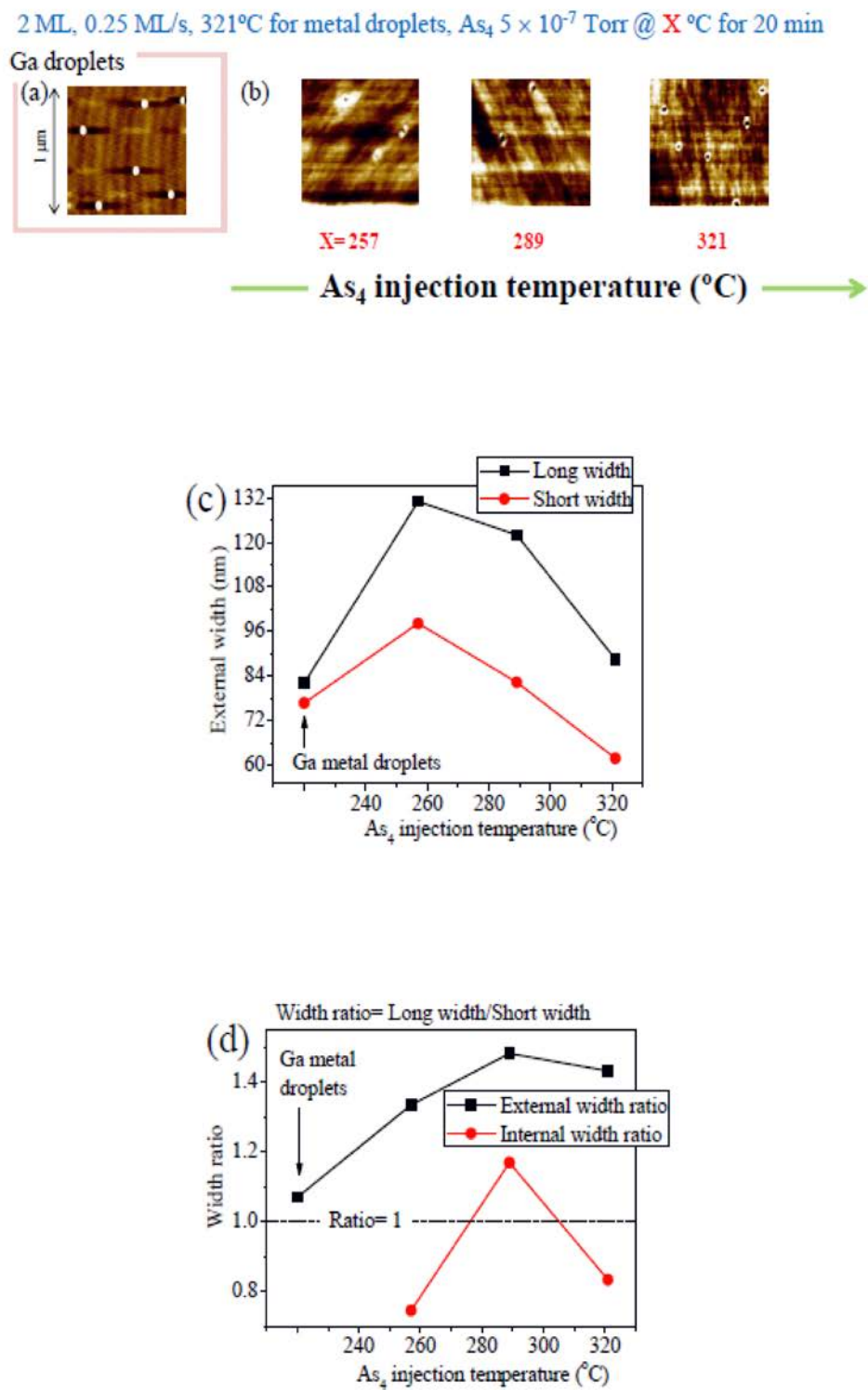


Figure 2.4: (a) AFM image of Ga droplets, (b) AFM images of GaAs QRs for the change of substrate temperature at As_4 injection. Statistical graph of (c) the long/short external width, (d) the external/internal width ratio

2.1 Single GaAs Quantum Ring growth procedure

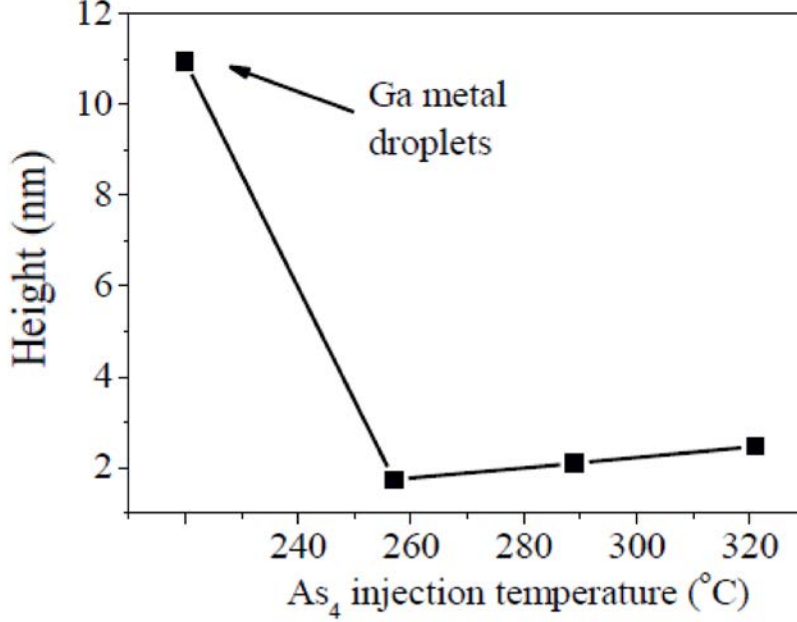


Figure 2.5: The height of GaAs QRs for a change in the substrate temperature at As₄ injection.

external shape of the QRs becomes relatively symmetrical. The present QRs at As₄ 5×10^{-7} Torr may be the result of such a migration. However, the origin of the coffee bean-like shape of the QRs at As₄ 5×10^{-7} Torr needs further investigation. Fig.2.2 (b) shows a trend of the height of the QRs for a change of the BEF of As₄. The change of the QRs height was negligible as a function of As₄ at less than 1×10^{-6} . However, the height of the GaAs nanostructures was lowered with the formation of QRs. The decrease in the height verifies that material is moving along the preferred direction to transform into QRs.

The growth interruption (GI) time could also make material move and this movement could help form QRs, since the formation of QRs mainly depends on movement of excess Ga atoms due to the relative lack of As₄ as mentioned in the previous paragraph. Fig.2.3 (a) ~ (c) show the statistics for GaAs QRs in width and height for a change of GI time. The sequence of As₄ injection including GI time is [As 10 s/ GI X s] \times 30. With an increase of GI time, the external widths of the QRs tend to generally

2. SAMPLE GROWTH AND EXPERIMENTAL SETUP

$X = \text{Metal } X$, $Y = t_{As_4}$ (As_4 1.2×10^{-7} Torr for Y s + As_4 $3e-6$ for 2 min) @ near RT

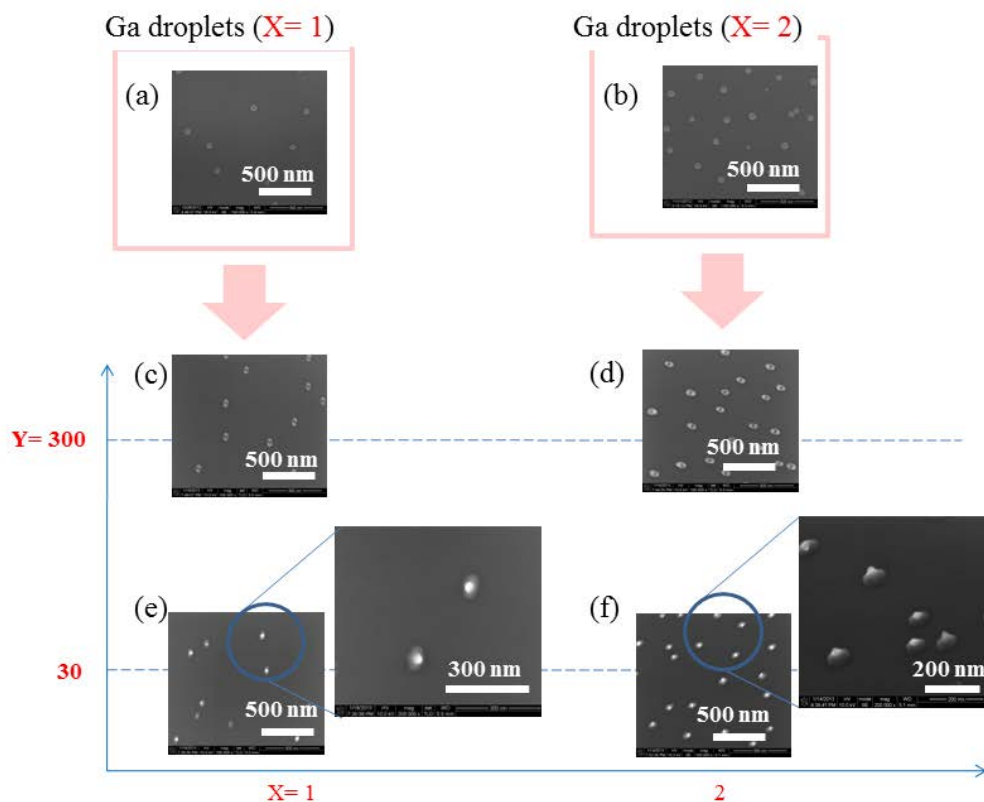


Figure 2.6: SEM images of (a) Ga droplet 1/(b) Ga droplet 2. The SEM results of As_4 injection for 300s on (c) Ga droplet 1/ (d) Ga droplet 2, for 30s on (e) Ga droplet 1/ (f) Ga droplet 2.

increase, as shown at Fig.2.3 (a). Slight lowering of the external width of QRs at GI 10 s indicates that the growth including GI time is based on different growth mechanism, compared to the case of the continuous injection of As.

Fig.2.3 (b) shows that the external/internal shape of QRs becomes more asymmetric with an increase of GI time, since the external and internal width ratio is increased. The notable thing is that the internal ratio for the QRs abruptly increased with a rise of GI time, compared to the increase of the external ratio. The origin of this phenomenon may be founded in the formation mechanism of the QRs. Since crystallization at the edge of QRs is faster than that at the center in the residual Ga atoms in the center

2.1 Single GaAs Quantum Ring growth procedure

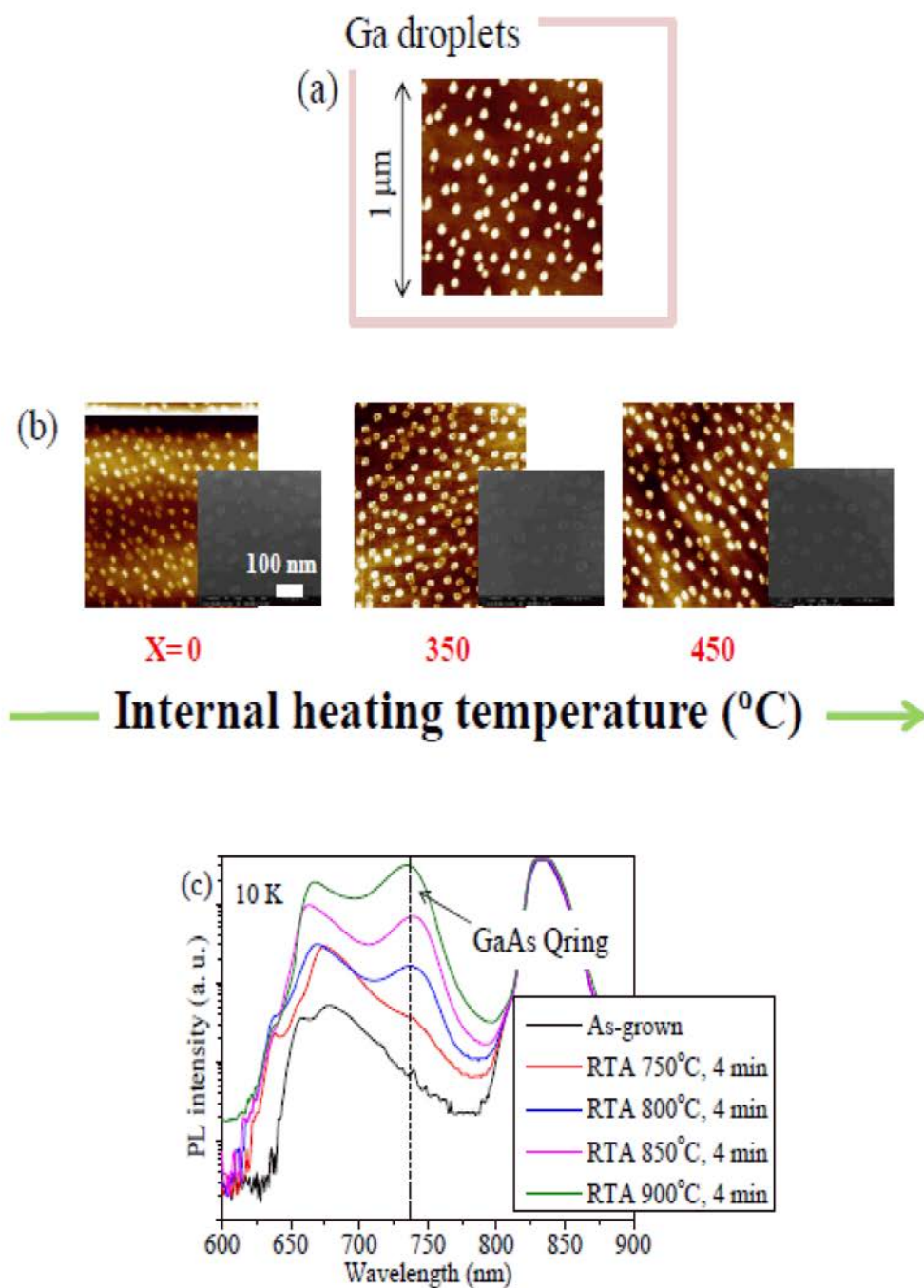


Figure 2.7: (a) AFM image of Ga droplet with 7~9 nm in height, 50~60 nm in width, and ~ 130 droplets/ μm^2 in density, (b) the results of GaAs QRs for increasing heating temperature, (c) PL of GaAs QRs at 10K for temperatures of 750 ~ 900 $^{\circ}\text{C}$

2. SAMPLE GROWTH AND EXPERIMENTAL SETUP

region can move to outside, thus the increase GI time might accelerate the movement of the Ga atoms in the center. This movement of Ga atoms in the center would increase the internal width ratio.

Fig.2.3 (c) shows that the height of the QRs increased with a rise in the GI time. This might be due to enhancement of crystallization at the rims of the QRs by piling up of Ga atoms. During the GI time, Ga atoms may move to the outside and the supply of Ga on the rim would help crystallization of QRs. The increase of the rim height would cause an increase of the height of QRs.

An increase of the substrate temperature at As_4 injection (T_{As}) can change the structural properties of GaAs QRs. Fig.2.4 (a) shows Ga droplets at $T_s = 321^\circ\text{C}$, $F_{\text{Ga}} = 0.25\text{ ML/s}$, and $C_{\text{Ga}} = 2\text{ ML}$ (58, 59). The arsenization results of Ga droplets in Fig.2.4 (a) are shown in Fig.2.4 (b). The BEF of As_4 was $5 \times 10^{-7}\text{ Torr}$. T_{As} increased from 257°C to 321°C . The change in the density of QRs was negligible, as shown at Fig.2.4 (b). A slight increase of the density at $T_{\text{As}} = 321^\circ\text{C}$ was observed. However, the density of QRs in the broader area was nearly constant. Fig.2.4 (c) ~ (d) and Fig.2.5 present trends in the formation of QRs (60, 61). With an increase of T_{As} , the external widths of the QRs were reduced as shown in Fig.2.4 (c). In Fig.2.4 (d), the external and the internal width ratios of the QRs show values around ~ 1.4 and ~ 1 , respectively. Meanwhile, the height of the QRs shows a slight increase with a rise of T_{As} . For this slight increase, it is assumed that an increase of T_{As} causes movement of Ga at the center. The piling up of Ga atoms on the rims at higher T_{As} might promote an As crystallization of QRs. In addition, it is shown that the heights of the present QRs at high substrate temperatures tend to be lower (approximately $2 \sim 3\text{ nm}$) than the heights of QRs grown at a low temperatures, as shown in Fig.2.1 ~ Fig.2.3. Compared to the QRs in Fig.2.1 ~ Fig.2.3, the decrease in the height of the QRs in Fig.2.5 may be due to a drilling effect on the surface.

The size of Ga droplets can affect As crystallization, since the solubility of As in Ga droplets is limited. Fig.2.6 (a) ~ (f) shows a change of As_4 injection time for two kinds of Ga droplets (Ga droplet 1 and 2). The Ga droplet 1 in Fig.2.6 (a) is $90 \sim 120\text{ nm}$ in width and $15 \sim 20\text{ nm}$ in height. The Ga droplet 2 of Fig.2.6 (b) is ~ 100

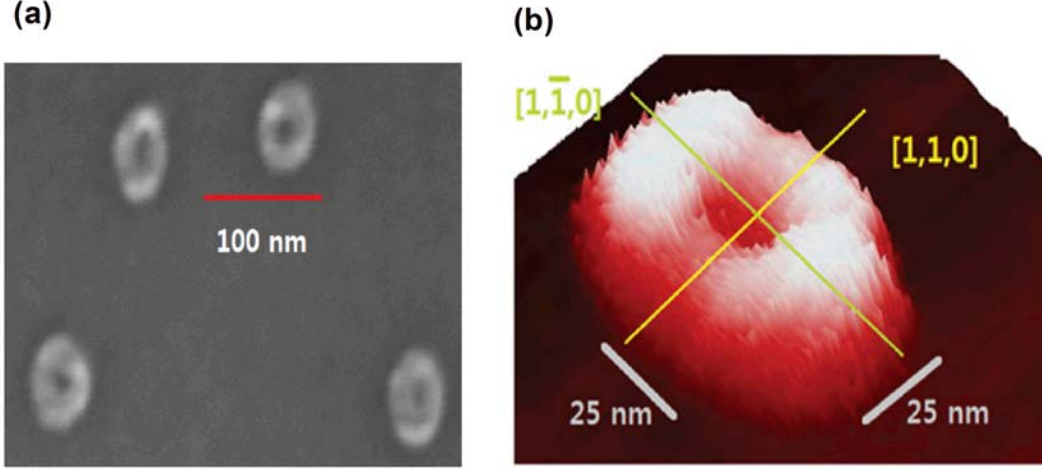


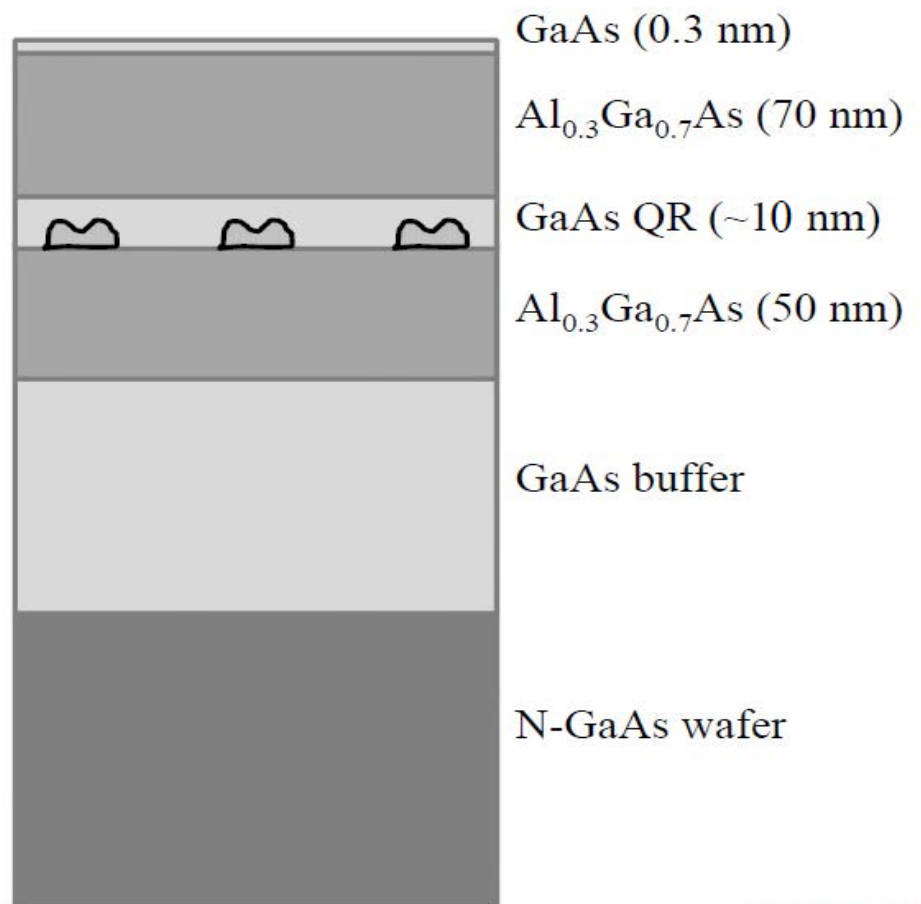
Figure 2.8: (a): A single ring structure observed by FESEM and AFM morphology (b)

nm in width and 20 ~ 30 nm in height. That is, the size of Ga droplet 2 is larger than Ga droplet 1. After As_4 injection at 1.2×10^{-7} Torr for 300s, both Ga droplet 1 and 2 was changed into the shape of rings or coffee beans, as shown at Fig.2.6 (c) and (d). However, for As injection for 30 s in Fig.2.6 (e) and (f), the GaAs nanostructures did not show ring shapes. The interesting thing is that the GaAs nanostructures in Fig.2.6 (f) have a protrusion in the center of the structures. This is due to the lack of As injection and residual Ga atoms in the center of the structures being crystallized at the final As_4 injection time under 3×10^{-6} Torr for 2 min. This result also proves that more Ga atoms leave the center in the case of larger Ga droplets.

2.2 Grown Single GaAs Quantum Rings and measurement

The GaAs rings investigated in this thesis were thus grown as follow on an n-doped GaAs (001). After thermal cleaning of the substrate under arsenic ambient at 600°C , a 100 nm-thick GaAs buffer layer and a 50 nm-thick $\text{Al}_{0.3}\text{Ga}_{0.7}\text{As}$ layer were grown successively at 580°C . The substrate temperature was decreased to 310°C , and Ga metal equivalent to 2 monolayer-thick GaAs was introduced to the substrate at the main chamber pressure of $\sim 3 \times 10^{-10}$ Torr. When the substrate temperature reached 200°C ,

2. SAMPLE GROWTH AND EXPERIMENTAL SETUP



#E10395

Figure 2.9: Capped GaAs quantum ring sample for optical measurement.

2.2 Grown Single GaAs Quantum Rings and measurement

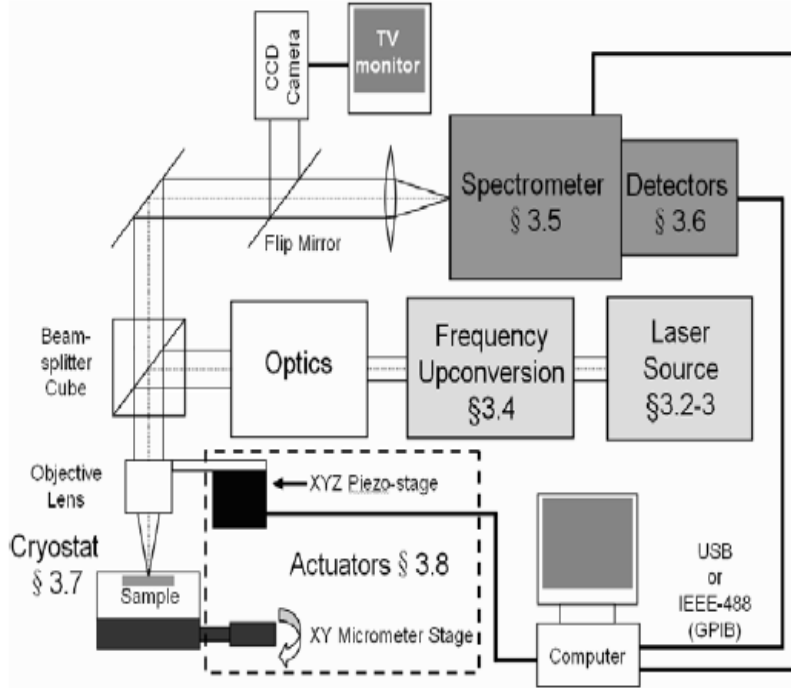


Figure 2.10: General micro-PL setup (62).

arsenic tetramers were introduced to form GaAs rings. Finally, the rings were capped with 60 nm-thick $\text{Al}_{0.3}\text{Ga}_{0.7}\text{As}$ and 3 nm-thick GaAs for optical measurements in Fig1. Also, asymmetric QR structures were observed in a field emission scanning electron microscope (FESEM) image and atomic force microscope (AFM) image of uncapped samples (Fig.2.8 (a),(b)).

The photoluminescence (PL) of a single QR was collected at 4 K using a confocal arrangement, where frequency-doubled (400 nm) Ti:sapphire laser pulses (120 fs pulse duration at a 80-MHz repetition rate) were focused on the QR sample ($\sim 6 \text{ QRs}/\mu\text{m}^2$) with a spot-size of $0.8 \mu\text{m}^2$. A time-correlated single photon counting system was used to obtain the time-resolved PL (TRPL).

2. SAMPLE GROWTH AND EXPERIMENTAL SETUP

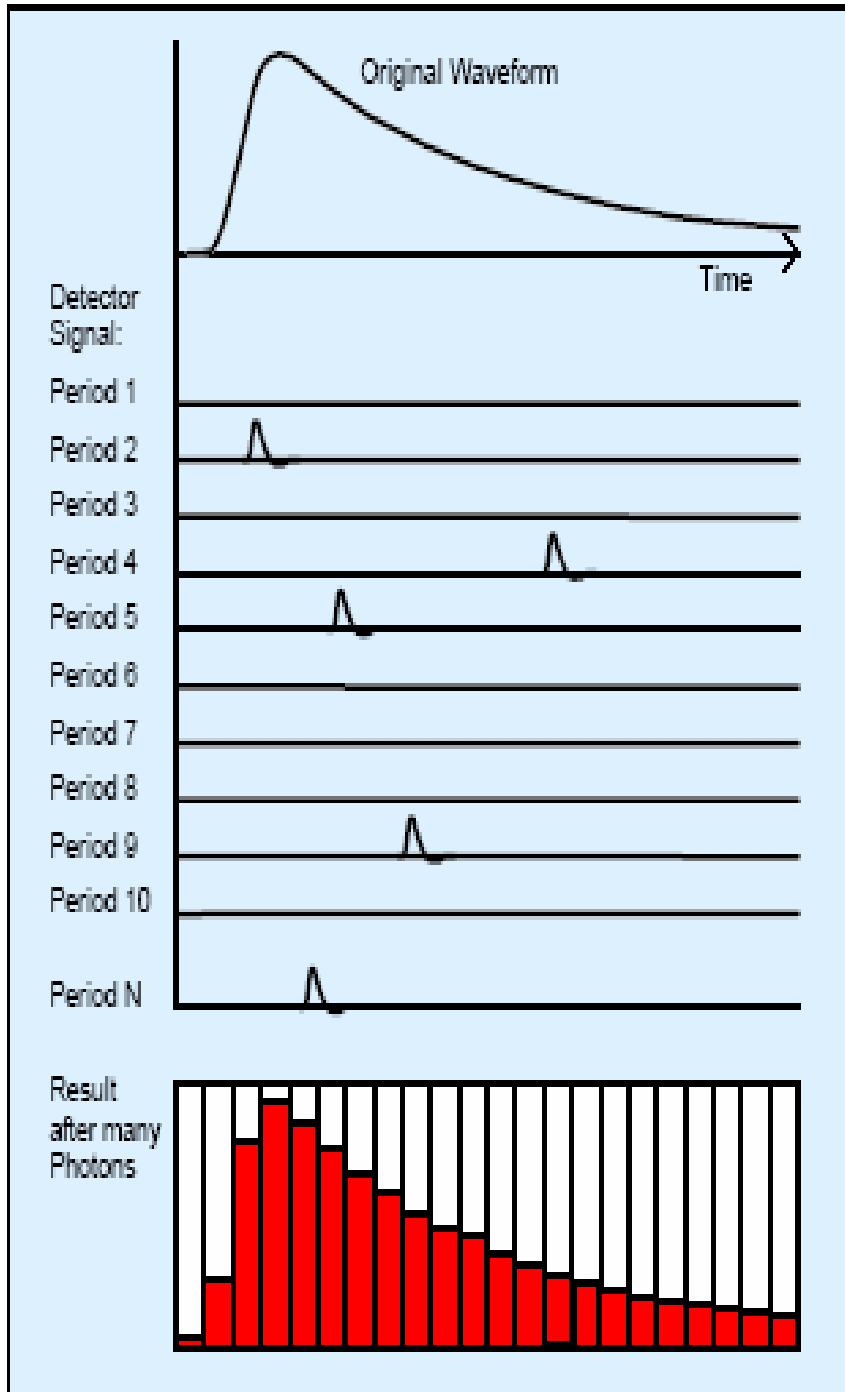


Figure 2.11: Schematic diagram of the waveform from the individual time measurements. The detection signal consists of a train of randomly distributed pulses due to the detection of the individual photons(62).

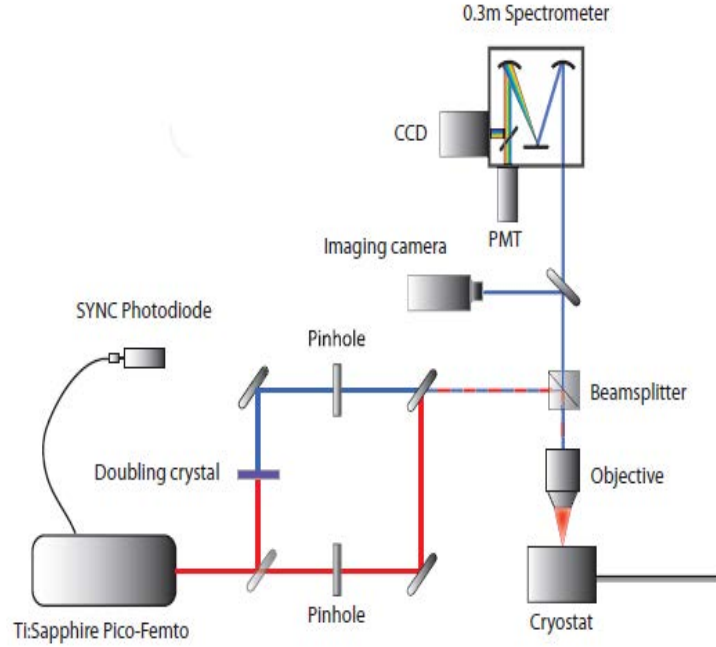


Figure 2.12: basic micro-photoluminescence setup for measurement single level structure. By flip mirror inside a spectrometer both time resolved and time integrated photoluminescence measurements are possible in this setup (63).

2.3 Experimental Setup

In μ PL spectroscopy, the sample is optically excited by laser sources with a microscope objective, then the PL from the sample is collected and dispersed. The objective lens produces a laser spot size of $1\mu\text{m}$. So as long as the density of QRs is low enough, this $1\mu\text{m}$ size laser spot enables to observe single QR structures.

2.3.1 Time Integrated μ -Photoluminescence

A typical setup is shown in Fig.2.10 and Fig.2.12, a frequency doubled Ti:Sapphire laser of 400nm is used as the excitation source. The photoluminescence from the sample is collected by an objective lens, then gathered by a grating spectrometer and spatially dispersed to detect on a charge coupled device (CCD). The Titanium Sapphire (Ti:S) laser has a titanium ion (Ti^{3+}) doped sapphire crystal as the active medium. In this study two different kinds of laser was used as excitation sources. First, a Coherent Mira

2. SAMPLE GROWTH AND EXPERIMENTAL SETUP



Figure 2.13: Hamamatsu C-4878 model PMT and power supply which are used for photon measurement(64).

900 was used producing both picosecond and femtosecond pulses. The Mira 900 which is pumped by coherent Verdi V8 diode laser can be tuned for emission in the range 700nm to 1000nm with an output of up to 1.5W. Second, a Mai-Tai Titanium: Sapphire (Ti:S) was used to investigate exciton dynamics in a single level structure. The Mai-Tai is pumped by a 532nm diode laser, and produces output pulses with 100fs duration at 80MHz. The output from this Mai-Tai mode-locked 100fs Ti:S is at 800nm with 1W average power. For measurement, this 800nm output was frequency doubled to 400 nm.

2.3.2 Time resolved μ -Photoluminescence

Time resolved photoluminescence techniques enable us to observe the decay dynamics of the photoluminescence from the observed sample. A pulsed laser source excited a single QR then a periodic decay signal come from excited single QR. The emitted single photon from the single QR is detected and gives statistical information to understand the life time of a single QR. Fig.2.11 shows statistical information for counted photons from the sample. A high level of timing accuracy is needed in the detector and correlation electronics if reliable results are to be obtained. Fig.2.14 and Fig.2.15 shows a detailed

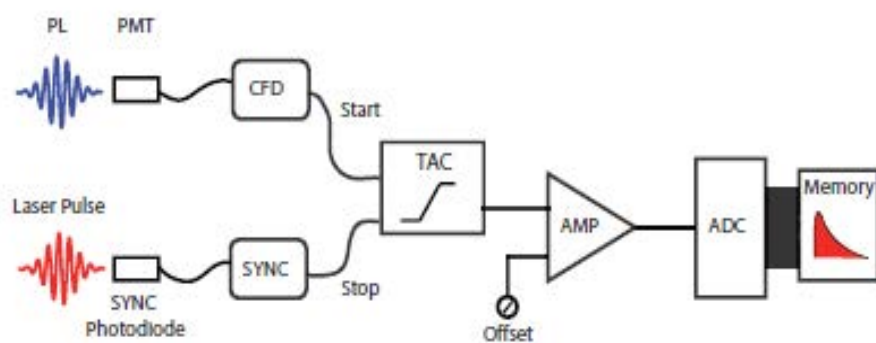


Figure 2.14: Outline of the TCSPC setup with the additional of an externally controlled amplifier which can be used for optimization of the recorded signal (63).

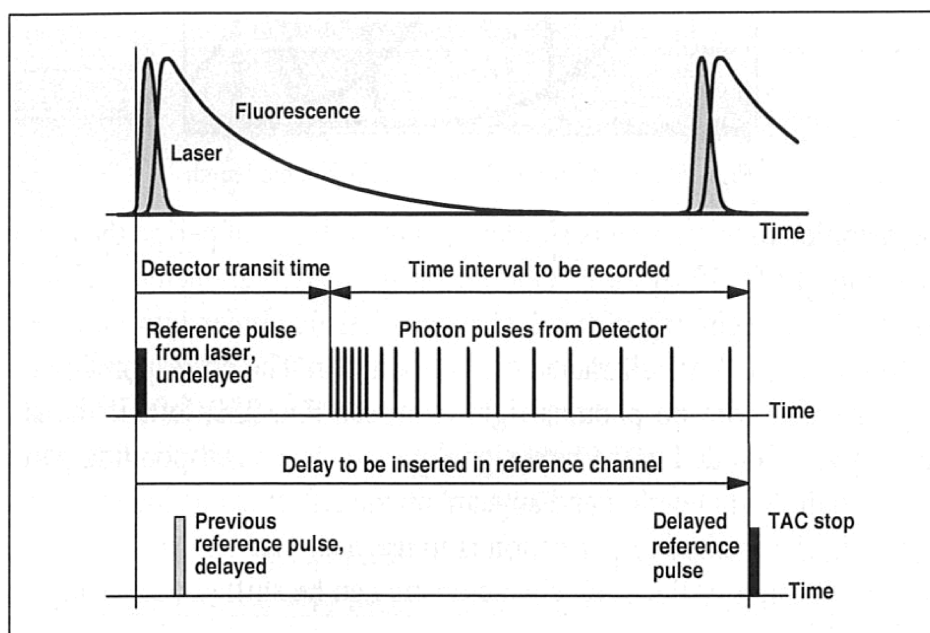


Figure 2.15: Reserved start-stop should be used with a delay in the reference channel to stop the Time to Amplitude Converter (TAC) with the correct laser pulse(64).

2. SAMPLE GROWTH AND EXPERIMENTAL SETUP

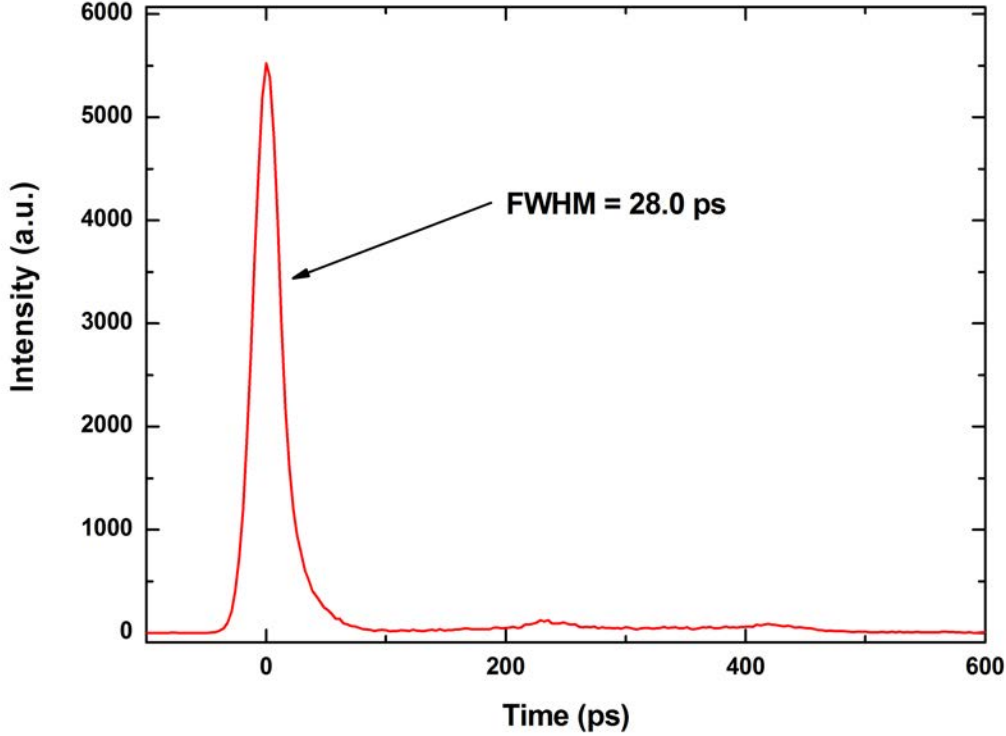


Figure 2.16: The Instrument response function of the FWHM limited by jitter is 45ps.

description of how to measure accurate photon numbers.

A commercial *Becker & Hickl SPC-630* single photon counting card which gives two inputs (one for the excitation laser source and another one for the detected PL from the photomultiplier tube (PMT) or avalanche photodiode (APD)) was used. The synchronisation (SYNC) is used to generate electrical pulses from the laser output. Then, the constant fraction discriminator (CFD) circuit delivers an output pulse correlated to detect accurate pulsed photon from PMT or APD. In this thesis, to measure fast decay dynamics from a single QR structure, a Hamamatsu C-4878 MCP- PMT with 50 ps time limit is usually used. The collected signals from the CFD and SYNC are fed to the Time to Amplitude Converter (TAC). The first pulse from the CFD activates a TAC circuit which is stopped by the SYNC photon from the second detector. The TAC determines the temporal position of the CFD signal relative to the SYNC pulse. Therefore, the TAC output is proportional to the temporal position of the photon. Thus the TAC gives us the time difference between the two different signals. Finally, this signal

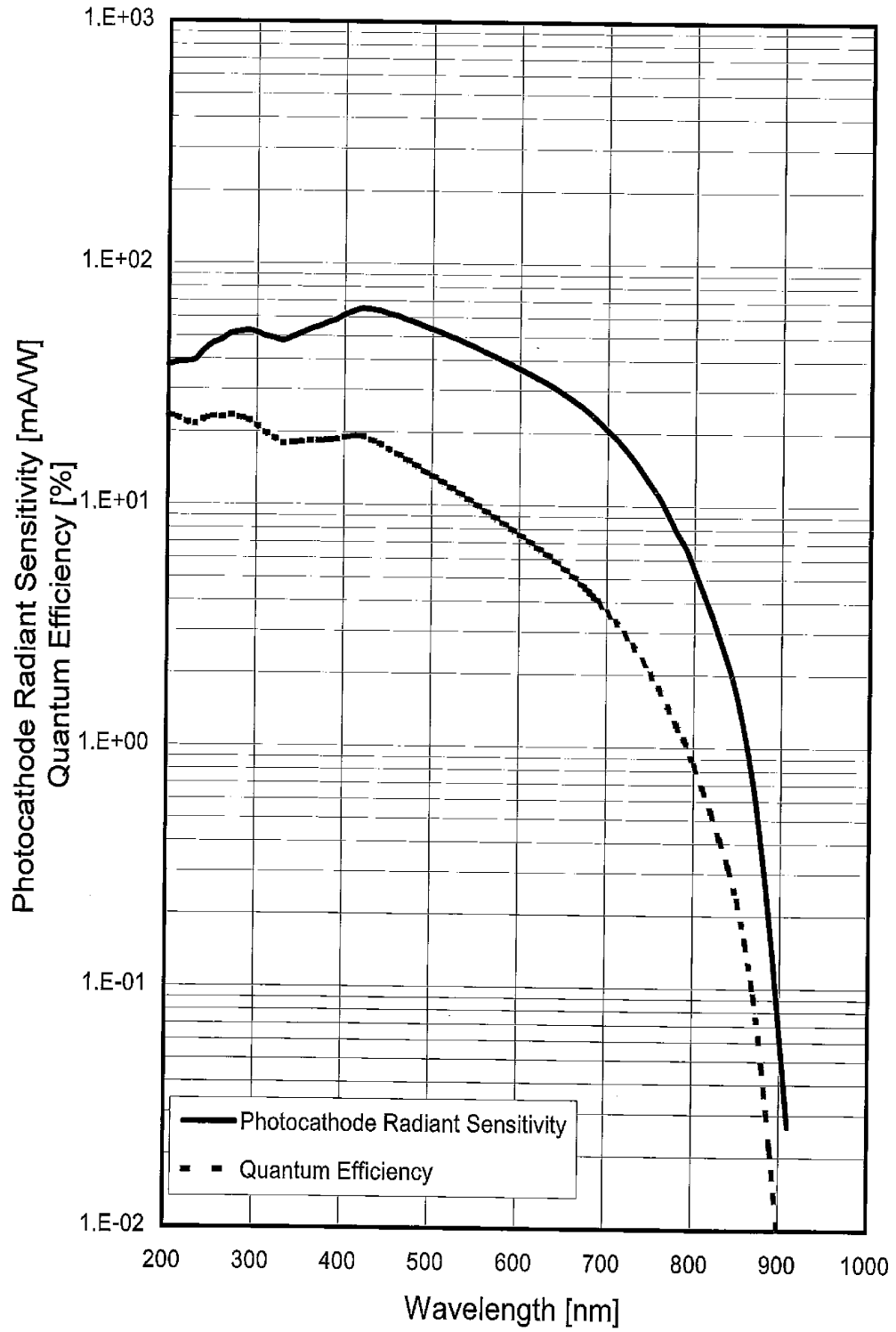


Figure 2.17: The quantum efficiency of Hamamatsu C-4878 MCP-PMT by wavelength(64).

2. SAMPLE GROWTH AND EXPERIMENTAL SETUP

is gathered at an analogue-to-digital converter (ADC). The ADC converts the signal from the TAC to a digital value to produce the photon statistics shown in Fig.2.11.

The PMT is an extremely sensitive light detectors and this is achieved by multiplying the signal produced by the incident light, from which a single photon can be resolved (65, 66, 67). The PMT consists of a glass vacuum tube which contains a photocathode (electron generator), several dynodes (electron multiplier), and an anode (electron collector). When an incident photon hits the photocathode material, an electron is produced. Then, the electron is directed towards the electron multipliers by the focusing electrode, where multiplication occurs through a secondary emission process. The multiplied secondary electrons are collected at the anode which produces an electron signal. Because of its high gain, low noise, high frequency response and a large collection area, the PMT remains popular for detecting photon counting. Fig.2.13 shows Hamamatsu C-4878 MCP-PMT with power supply which are used to investigate the decay dynamics in this thesis. The Hamamatsu C-4878 MCP-PMT is a thermoelectric cooler constructed with enhanced electrostatic and magnetic shielding for stable photon counting. This minimizes the influence of external noise on the photomultiplier tube and thus significantly improves photometric accuracy. Also, the detection range for incoming photons is 160nm-850nm, and has a time resolution corresponding to its instrument response function (IRF) of 28ps in Fig.2.16 with 5% quantum efficiency at 680nm in Fig.2.17 which is enough to resolve the fastest decay dynamics in GaAs QRs.

3

Polarization dependence of the $k=3$ localized state

We performed spectroscopic studies of a single GaAs quantum ring with an anisotropy in the rim height (68). The presence of an asymmetric localised state was suggested by the adiabatic potential (18, 69). The asymmetry was investigated in terms of the polarization dependence of excitons and biexcitons, where a large energy difference ($\sim 0.8\text{meV}$) in the exciton emission energy for perpendicular polarizations was observed and the oscillator strengths were also compared using the photoluminescence decay rate (70). For perpendicular polarizations, the biexciton exhibits twice the energy difference seen for the exciton, a fact that may be attributed to a possible change in the selection rules for the lowered symmetry (71, 72, 73).

3.1 Theoretical calculations for the localized state inside a single quantum ring

As shown in Fig.3.1(a) and Fig.3.2, the volcano-like ring structure was modelled in cylindrical coordinates ($z = z(r, \phi)$) based on atomic force microscope (AFM) images of uncapped GaAs QRs (Fig.2.8 (b)), where both anisotropy and asymmetry are present (17, 27). The rim height is a maximum at the azimuthal angles of 0° and 180° along the $[1\bar{1}0]$ direction, and a minimum at the perpendicular angles of 90° and 270° along the $[110]$ direction, respectively. The in-plane shape is elliptical with the

3. POLARIZATION DEPENDENCE OF THE $l=3$ LOCALIZED STATE

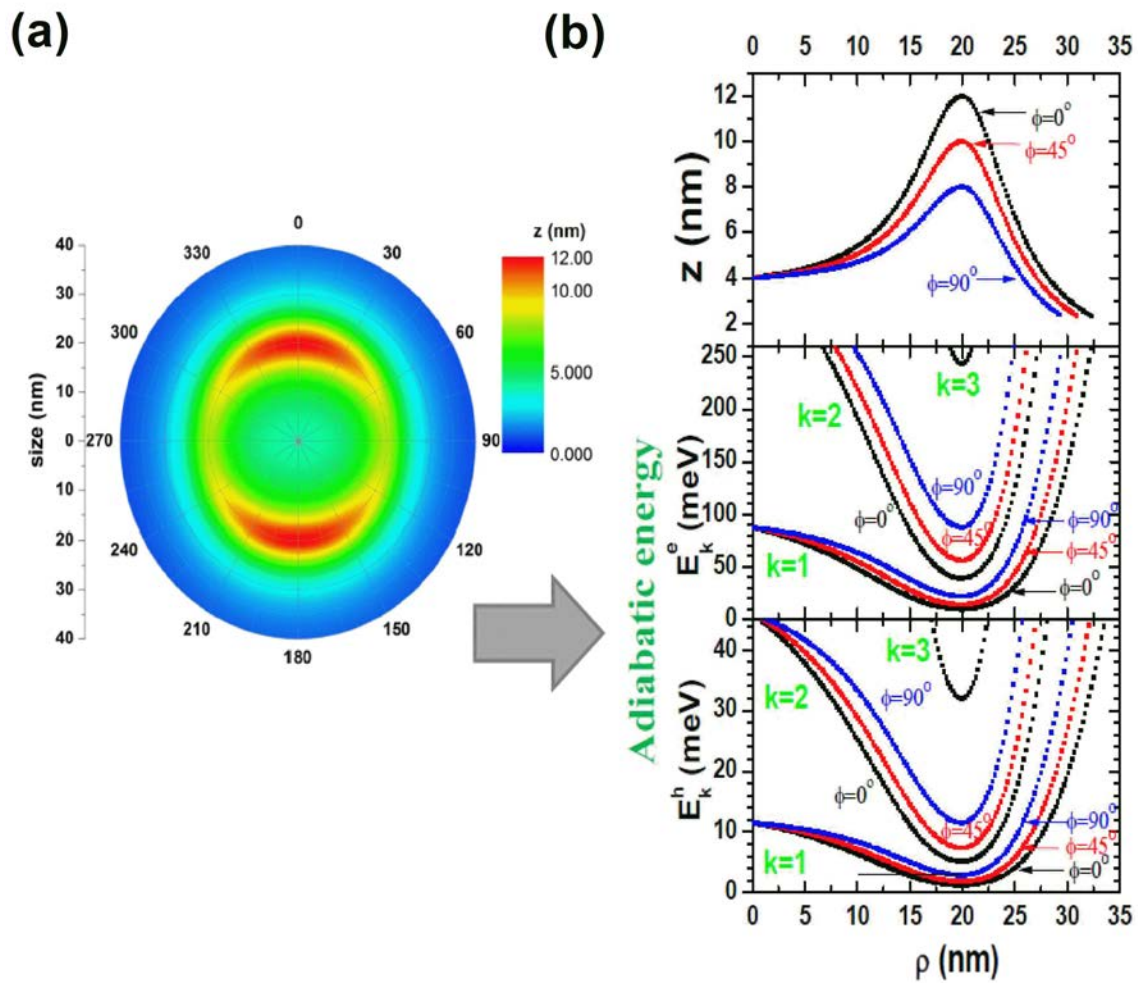


Figure 3.1: (a): Volcano-like ring model for the rim height based on the AFM morphology (b): the energy range of the radially confined orbitals for the azimuthal angle for the electron and the hole and rim height for the azimuthal angle

3.1 Theoretical calculations for the localized state inside a single quantum ring

long axis along $[1\bar{1}0]$, and the height in the middle of the QR is ~ 3 nm. Since the vertical height ($7 \sim 12$ nm) is smaller than the ring size (~ 50 nm), the fast vertical wavefunction can be separated by the adiabatic approximation (15, 74, 75), where the potential of electron and hole depends on the volcano-like ring structure respectively as $V_{e,h}(z, r, \phi) \simeq V_{e,h}(z(r, \phi))$. Consequently, the adiabatic potential $\varepsilon_{e,h}^k(r, \phi)$ can be obtained for the electron and hole separately by solving the vertical part of the Schrödinger equation, where the vertical confinement is represented by the vertical quantum number k . Fig.3.1 (b) shows adiabatic potential for different vertical quantum numbers.

In the case of an ideal isotropic ring, $\varepsilon_{e,h}^k(r)$ can be simplified by using a parabolic function ($\sim (r - r_0)^2$), where the maximum ring height is positioned at r_0 (76, 77). Although the fine structure of the PL spectrum in a QR has often been attributed to quantized rotational motion along the rim (27, 78), the cylindrical symmetry of a QR can easily break down, which is similar to the case of an elliptical QD (79, 80). Also, the anisotropy in the rim height requires an azimuthal angle-dependence of the vertical confinement (81). Both the asymmetry of the in-plane ellipticity and the height anisotropy have been mostly overlooked in previous spectroscopy (55, 82, 83). These effects can be parameterized in terms of $\varepsilon_{e,h}^k(r, \phi)$, which is similar to an inversion of the asymmetric and anisotropic structure morphology (84, 85, 86).

The Schrödinger equation,

$$H_e \psi^{(e)}(r) = E \psi^{(e)}(r) \quad (3.1)$$

is solved by the adiabatic approximation with ansatz

$$\psi^{(e)}(r) = \psi_k^{(e)}(z, \rho, \varphi) \phi_{kj}^{(e)}(\rho, \varphi) \quad (3.2)$$

index k numbers subbands due to the size quantization along z axis,

$$\left[-\frac{\hbar^2}{2} \frac{\partial}{\partial z} \frac{1}{m_e(\rho, \varphi, z)} + V_e(\rho, \varphi, z) \right] \psi_k^{(e)}(z, \rho, \varphi) = \varepsilon_k^{(e)}(\rho, \varphi) \psi_k^{(e)}(z, \rho, \varphi) \quad (3.3)$$

3. POLARIZATION DEPENDENCE OF THE K=3 LOCALIZED STATE

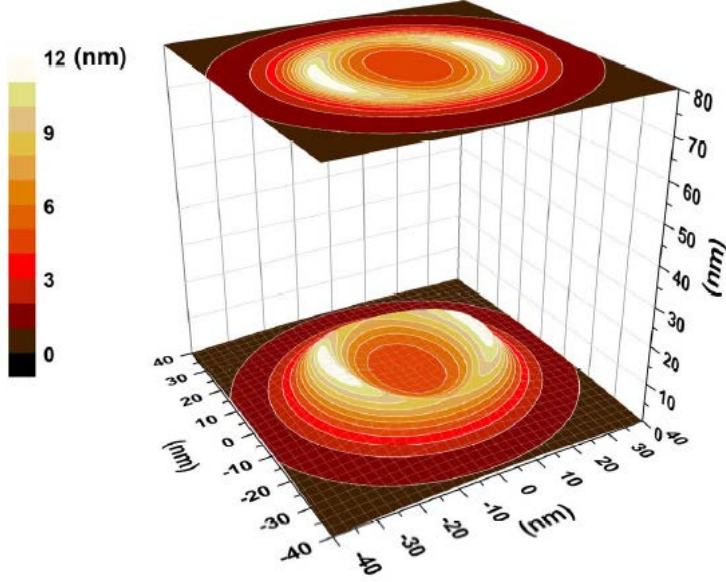


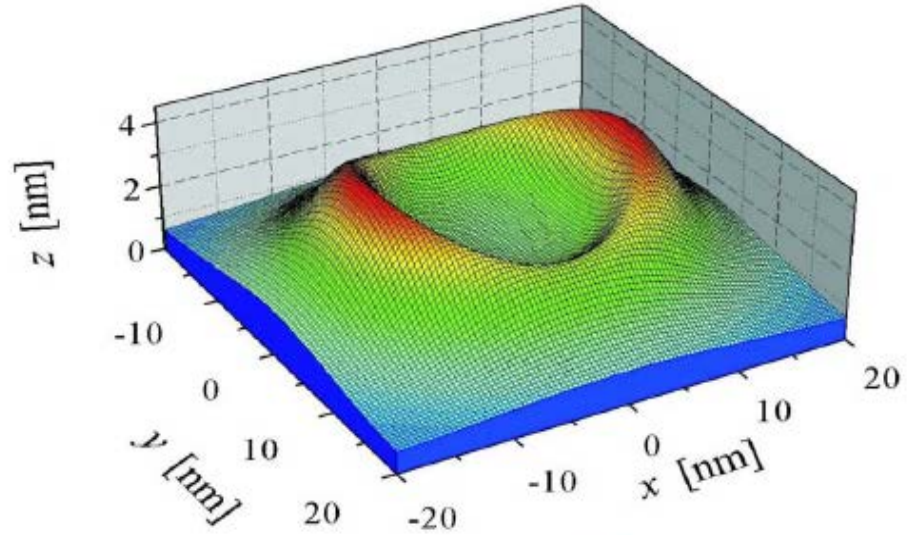
Figure 3.2: Volcano-like ring structure with height for calculation

We can understand the adiabatic potential $\varepsilon_k^{(e)}(\rho, \varphi)$ as corresponding to the global eigen energy $E_{kj}^{(e)}$ (87, 88, 89). The Schrödinger equation [Eq.3.3] gives us a fast degree of freedom (along the z axis) which is solved numerically in a two-dimensional grid in the (ρ, φ) plane. As a result, we can obtain the adiabatic potentials $\varepsilon_{e,h}^k(r)$. In Fig.3.3 (a), a real volcano like QR structure and corresponding adiabatic potential for the electron dynamics in a $\text{In}_x\text{Ga}_{1-x}\text{As}/\text{GaAs}$ self-assembled quantum ring is shown. If the central maximum of the adiabatic potential is sufficiently high, the adiabatic potential has two pronounced minima, which can be regarded as the potential distribution of two quantum dots and if the minima in the potential are sufficiently deep [shown in Fig.3.3 (b)], the electron can be localized in one of those quantum dots and in this case no persistent current occurs. When the depth of the potential minima is reduced, electron tunneling is possible over the two separate potential minima points.

To find the eigenstates for the in-plane electron dynamics, the Schrödinger equation for the slow degrees of freedom is

3.1 Theoretical calculations for the localized state inside a single quantum ring

(a)



(b)

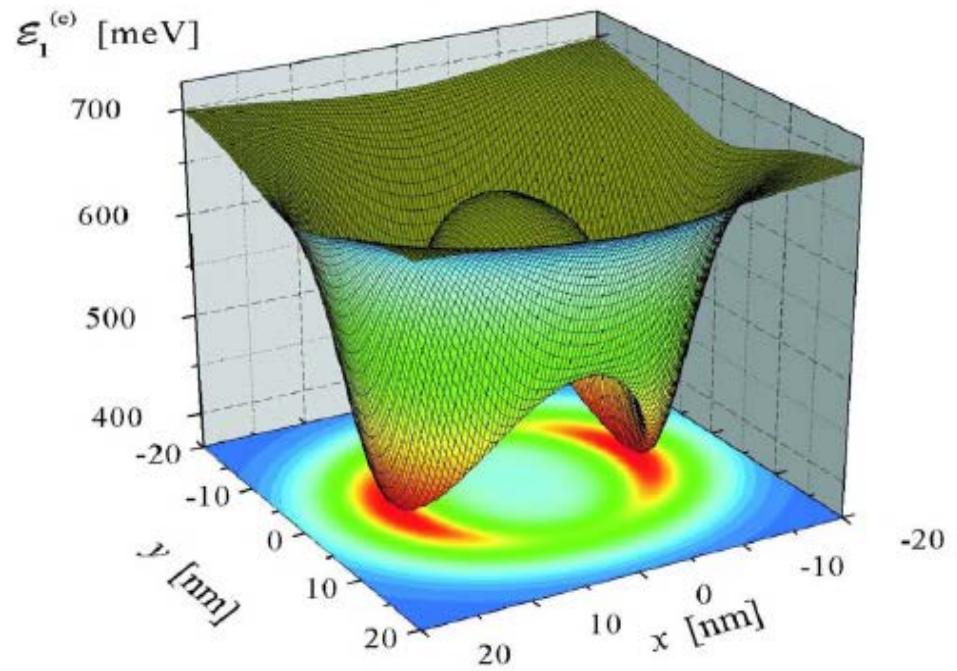


Figure 3.3: (a) ideal volcano like ring structure, (b) The adiabatic potential for the delocalized electron motion on the volcano like ring structure (11).

3. POLARIZATION DEPENDENCE OF THE K=3 LOCALIZED STATE

$$\begin{aligned} \left[-\frac{\hbar^2}{2} (\nabla_{\rho, \varphi} - \frac{e}{\hbar} A) \frac{1}{m_k^{(e)}(\rho, \varphi)} (\nabla_{\rho, \varphi} - \frac{e}{\hbar} A) + \varepsilon_k^{(e)}(\rho, \varphi) \right] \times \phi_{kj}^{(e)}(\rho, \varphi) \\ = E_{kj}^{(e)} \phi_{kj}^{(e)}(\rho, \varphi) \end{aligned} \quad (3.4)$$

with the effective mass

$$m_k^{(e)}(\rho, \varphi) = \int dz |\psi_k^{(e)}(z, \rho, \varphi)|^2 m_e(\rho, \varphi, z) \quad (3.5)$$

These give the eigenfunctions for the in-plane dynamics. Unfortunately, the slow degree Schrödinger equation with an adiabatic potential $\varepsilon_k^{(e)}(\rho, \varphi)$ and position-dependent effective mass $m_k^{(e)}(\rho, \varphi)$ can't be solved analytically (90, 91).

Therefore, we assume a simplified potential under a Fock-Darwin model to find the in-plane direction eigenfunctions (93, 94, 95, 96).

$$\bar{\varepsilon}_k^{(e)}(\rho) = \nu_k^{(e)} + \omega_k^{(e)} \rho^2 \quad (3.6)$$

This potential is isotropic, and the in-plane eigenfunctions can be expressed as

$$\bar{\phi}_{knL}^{(e)}(\rho, \varphi) = \bar{\chi}_{knL}^{(e)}(\rho) e^{iL\varphi} \quad (3.7)$$

where n labels the radial solutions. These basis eigenstates are the Fock-Darwin eigenfunctions in the two dimensional harmonic oscillator in a magnetic field which were used in the theory of quantum dots (97, 98, 99, 100). So, based on Eq.(3.6), (3.7), we can obtain the one-dimensional Schrödinger equation,

$$(\bar{\chi}_{knL}^{(e)})'' + \frac{1}{\rho} (\bar{\chi}_{knL}^{(e)})' + \left[\frac{2\bar{m}_k^{(e)}}{\hbar^2} (E_{knL}^{(e)} - \nu_k^{(e)}) + \frac{L}{l^2} - \frac{L^2}{\rho^2} - (\alpha_k^{(e)} \rho)^2 \right] \bar{\chi}_{knL}^{(e)} = 0 \quad (3.8)$$

where $l = \sqrt{\frac{\hbar}{eH}}$ is the magnetic length and

$$\alpha_k^{(e)} = \sqrt{\frac{1}{4l^4} + \frac{2\bar{m}_k^{(e)} \omega_k^{(e)}}{\hbar^2}} \quad (3.9)$$

3.1 Theoretical calculations for the localized state inside a single quantum ring

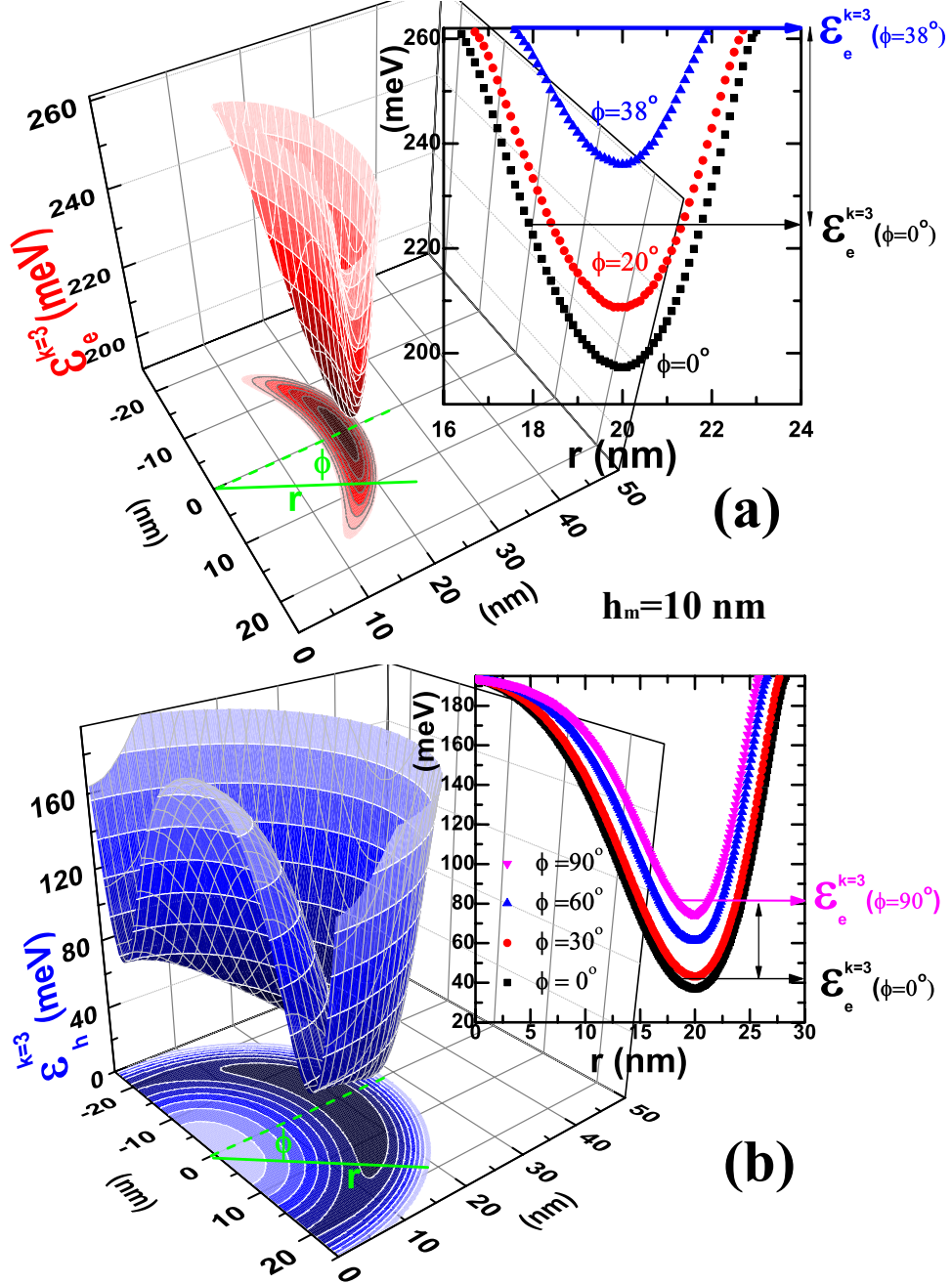


Figure 3.4: Adiabatic potentials ($\mathcal{E}_{e,h}^{k=3}$) of the electron (a) and the hole (b) for a vertical quantum number of $k = 3$ are shown, where the insets show the energy range of the radially confined levels for the azimuthal angle for the electron and the hole, respectively (92).

3. POLARIZATION DEPENDENCE OF THE $k=3$ LOCALIZED STATE

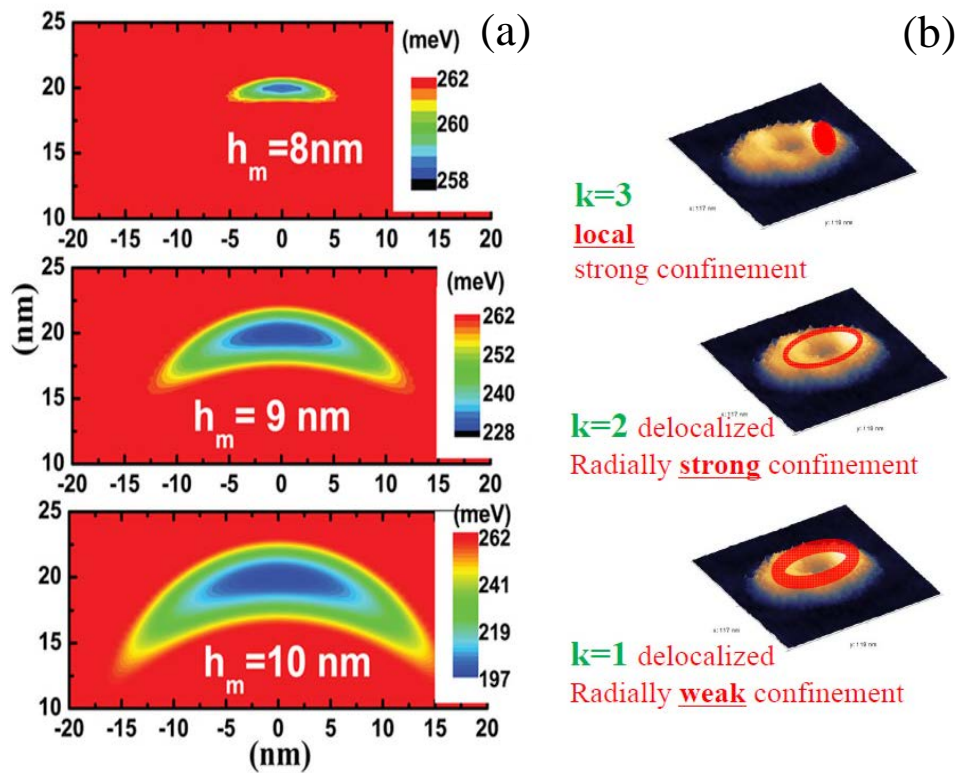


Figure 3.5: Adiabatic potentials ($\epsilon_{e,h}^{k=3}$) of the electron (a) and the hole (b) for a vertical quantum number of $k = 3$ are shown, where the insets show the energy range of the radially confined levels for the azimuthal angle for the electron and the hole, respectively.

3.1 Theoretical calculations for the localized state inside a single quantum ring

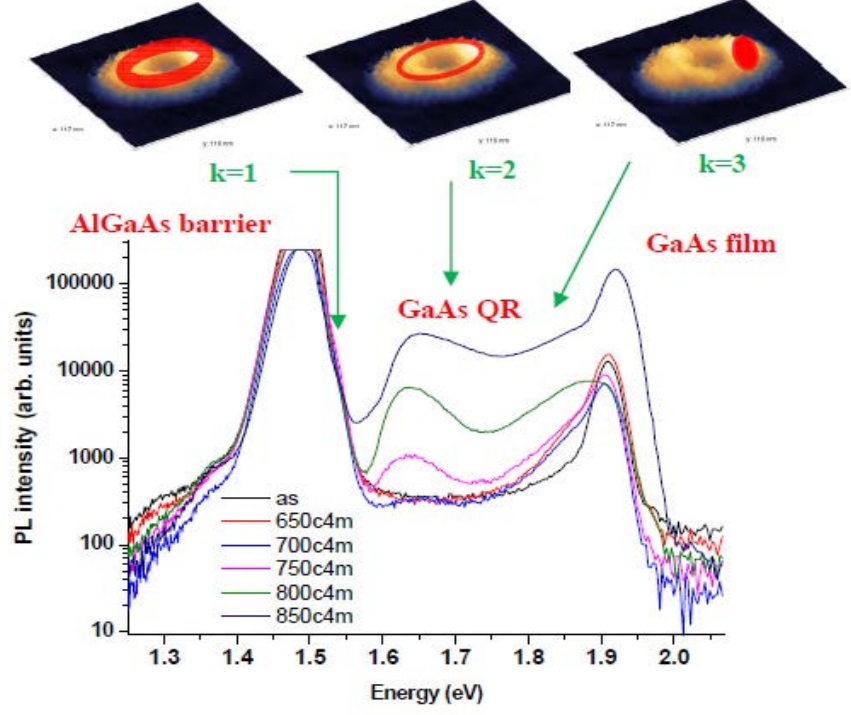


Figure 3.6: Energy ranges for vertical quantum number $k = 1, k = 2$ and $k = 3$ with quantum rings in an ensemble.

Eq.(2.8) gives eigenfunctions

$$\bar{\chi}_{knL}^{(e)}(\rho) = C_{knL} \rho^{|L|} \exp\left(-\frac{\alpha_k^{(e)} \rho^2}{2}\right) L_n^{(|L|)}(\alpha_k^{(e)} \rho^2), \quad (3.10)$$

$n=0,1,2,\dots,$

where $L_n^{(m)}(x)$ are generalized Laguerre polynomials and C_{knL} are normalization constants. The corresponding eigenenergies are

$$E_{knL}^{(e)} = \nu_k^{(e)} + \frac{\hbar^2}{m_k^{(e)}} \left[\left(n + \frac{1}{2} - \frac{L}{2}\right) \frac{1}{l^2} + |L| \alpha_k^{(e)} \right] \quad (3.11)$$

Provided that the potential hill of $\varepsilon_{e,h}^k(r, \phi)$ is found near the azimuthal angles 90° and 270° , the wavefunction delocalisation of the ground state depends on the tunnelling

3. POLARIZATION DEPENDENCE OF THE K=3 LOCALIZED STATE

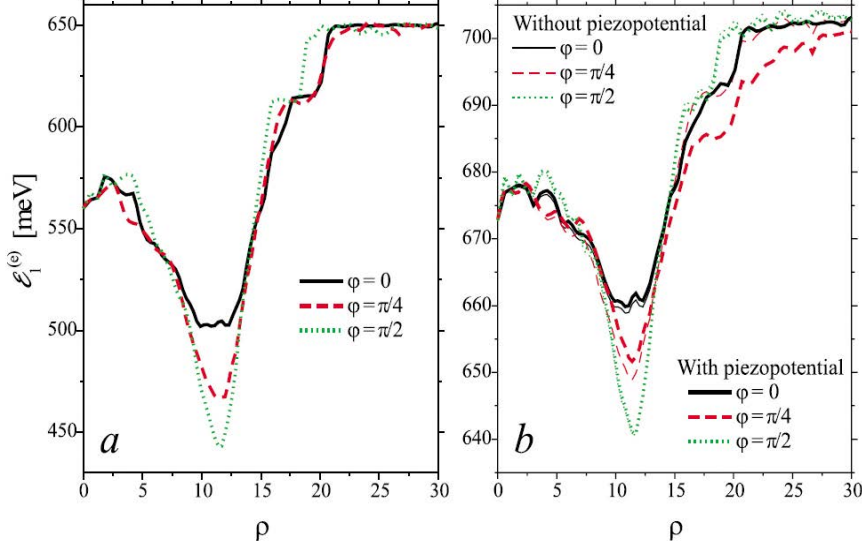


Figure 3.7: Adiabatic potential, calculated in the absence (a) and in the presence (b) of strain in the in-plane directions with angular coordinate φ (103, 104).

efficiency, which determines either localised (101, 102) or extended states. However, it should be remembered that the number of confinement states can be a measure of the confinement size, i.e., the higher rim (z) contains more vertical confinement states than the lower rim. In other words, excited confinement states are allowed only at the limited azimuthal angles of the high rim region as the k quantum number increases (17). We found that vertical confinement states can be defined at all of the azimuthal angles up to $k = 2$. Therefore, the vertical excited state of $k = 3$ is a criterion of the localisation. As shown in Fig.3.5, the electron adiabatic potentials for $k = 3$ ($\varepsilon_e^{k=3}(r, \phi)$) are localised at limited azimuthal angles for three different QR heights ($h_m = 8, 9, 10$ nm), where the rim height is characterized with a parameter h_m . As the QR height is decreased, the localized potential area becomes reduced.

The adiabatic potentials of the electron ($\varepsilon_e^{k=3}$) and hole ($\varepsilon_h^{k=3}$) are compared for $h_m = 10$ nm in Fig.3.4 (27). Also, the radially confined energy of the adiabatic potential for $\phi = 0^\circ$ and $\phi = 90^\circ$ are estimated with the parabolic approximation for the

3.1 Theoretical calculations for the localized state inside a single quantum ring

electron and the hole (insets in Fig.3.4), respectively. Whilst the holes are confined for all azimuthal angles (Fig.3.4 (b)), the electron is confined to the limited azimuthal angles ($-38^\circ \sim 38^\circ$) (Fig.3.4 (a)) due to the shallow potential well compared to the barrier energy in the conduction band (262 meV). Therefore, the ground eigen-energy of the electron and the hole should be located in the range of the radially confined levels for azimuthal angle ($\varepsilon_{e,h}^{k=3}(\phi)$). For example, suppose the ground level of the electron is located near 240 meV, the confined wavefunction becomes localised like a crescent structure. However, the tunnelling wavefunction is extended up to ~ 4.5 nm in the barrier. On the other hand, the hole wavefunction also becomes localised when the hole ground level is assumed to be ~ 60 meV, but the tunnelling length is small (~ 0.7 nm) as the barrier energy in the valence band (195 meV) is still large. Consequently, the localised area of the electron would be larger due to the large tunnelling and PL quenching becomes significant for increasing temperature. We found the PL intensity is nearly quenched beyond ~ 45 K.

The exact ground state energy of the electron-hole (e-h) pair can be refined by adding the Coulomb interaction to the independent e-h pair, i.e., the total energy is determined by the ground state energy sum of each adiabatic potential and the Coulomb energy. In the case of strong confinement, the effective Coulomb interaction was known to be enhanced with a factor of 1.786. However, both the vertical and the lateral confinement energy are far larger than the Coulomb interaction (~ 4.2 meV for bulk GaAs). Thus, the energy levels are dominated by the confinement effect, and this rough model predicts the range of the e-h pair at the $k = 3$ state (1.814 \sim 1.864 eV). As shown in Fig.3.9, the PL spectrum was measured near the barrier ($\text{Al}_{0.3}\text{Ga}_{0.7}\text{As}$) energy. It exhibits a strong polarization dependence for the exciton (X) and biexciton (XX) states at 1.6 kWcm^{-2} , where the nature of the XX emission appearing 5 meV below that of the X was characterised by a quadratic rise in its PL intensity and the fast decay of the TR-PL (Fig.3.9 (b)) relative to the X (105, 106). The X and XX emission spectra were both measured simultaneously at a series of analyzer angles. We also observed the PL spectrum in the predicted $k = 3$ range (1.813 eV, 1.821 eV, 1.832 eV, and 1.842 eV) at different QRs; they all show the similar polarization dependence (107, 108, 109).

3. POLARIZATION DEPENDENCE OF THE K=3 LOCALIZED STATE

The wavefunction of the electron and the hole can be imagined roughly as an inversion structure of the adiabatic potential in Fig.3.4. Since both $\varepsilon_e^{k=3}$ and $\varepsilon_h^{k=3}$ are anisotropic, the e-h pair is likely to be localised in either of the two crescent structures instead of delocalization around the whole rim (110, 111, 112). The localised e-h pair can be verified in terms of the large energy splitting for perpendicular polarizations. Since the localised states are of a crescent shape, the fine structure states resulting from various different confinement dimensions may depend on the analyzer angle. Additionally, during the sample growth, identical crescents are unlikely to be grown in an anisotropic QR and the energetic resonance at $k = 3$ state between the two crescents is vulnerable to small size differences (113). In this case, the e-h pair is favoured to be localised to the larger crescent-like structure.

3.2 The Polarization dependence in exciton and biexciton states

Whilst the two orthogonally polarized states of $|X\rangle$ and $|Y\rangle$ in an elliptical QD (114, 115, 116) can be spectrally isolated by a linear polarizer (117, 118, 119), the fine structure states at different angles in the asymmetric $\varepsilon^{k=3}(r, \phi)$ can overlap in the PL spectrum of X. Therefore, the analyzer angle dependence of the PL intensity is mapped at different energies in polar coordinates as shown in Fig.3.8 (b), where the maximum intensity of each PL spectrum is normalized to make a comparison possible. For example, the maximum PL intensity of X at 1.8208 eV measured at 0° is gradually reduced until the analyzer angle rotates to 90° , but increases again up to 180° . Consequently, this sinusoidal behavior gives rise to a dumbbell-like trace. All of the dumbbell-like traces obtained at different energies are similar, but rotated in a regular manner. The relative angular delay (θ) between the traces varies with emission energy. The trace at 1.8200 eV is 90° -rotated with respect to that at 1.8208 eV, and an energy difference (Δ) of 0.8 meV is obtained. This value is remarkably large in comparison to the asymmetric splitting ($\Delta_{XY} \sim 0.1$ meV) of an elliptical quantum dot (120, 121, 122, 123).

In the case of an elliptical quantum dot, an asymmetric electron-hole exchange interaction leads to a splitting (Δ_{XY}) of the double exciton state ($|\pm 1\rangle$) into two

3.2 The Polarization dependence in exciton and biexciton states

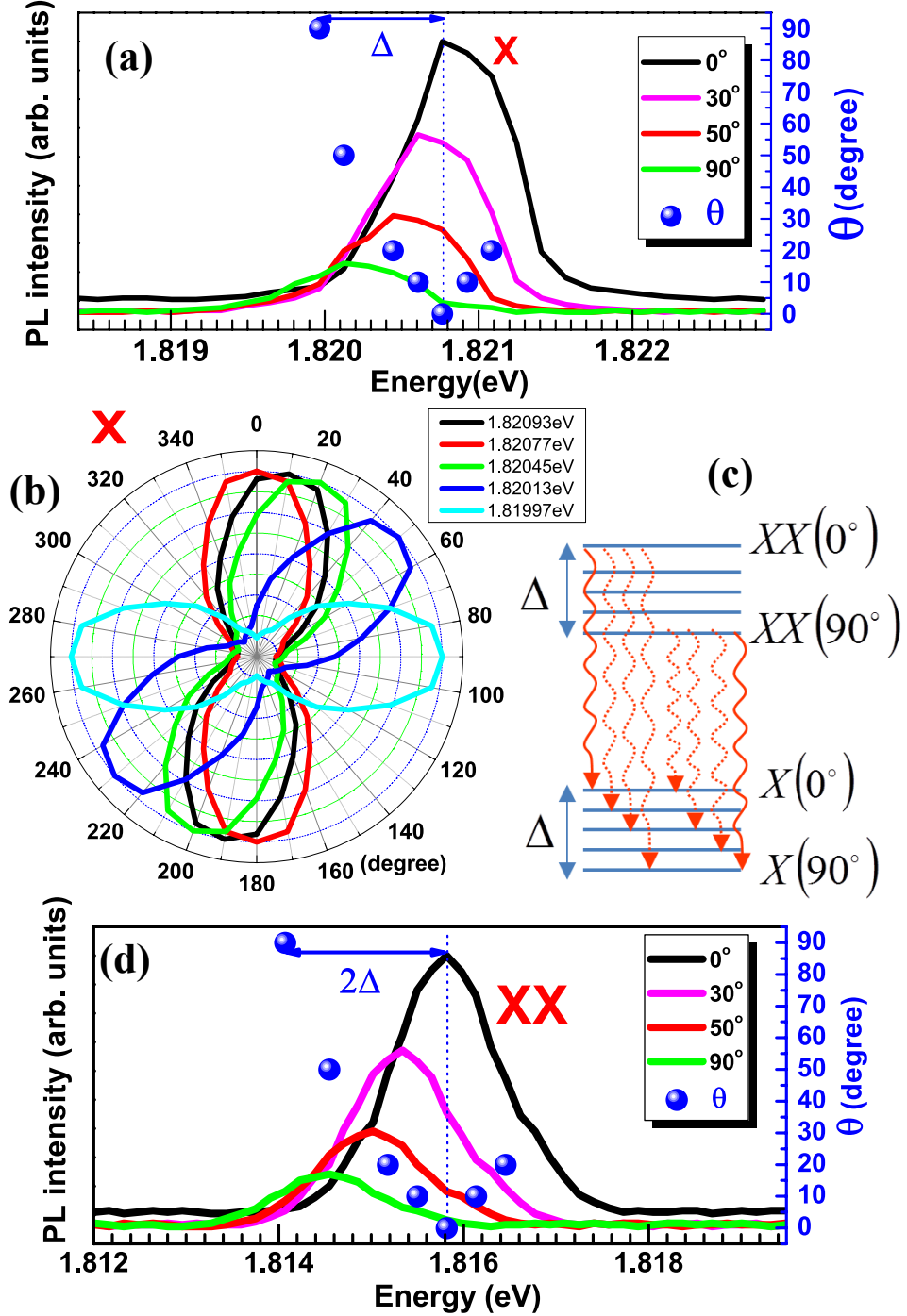


Figure 3.8: PL spectrum of the X (a) and XX (d) at various analyzer angles in a single QR. (b) Normalized PL intensity as a function of analyzer angle is mapped in polar coordinates at various energies, whereby the relative angular delay (θ) of each dumbbell-like trace can be obtained for the X and XX. (c) Schematic diagram of a multitude of transitions between the fine structure states of XX and X.

3. POLARIZATION DEPENDENCE OF THE K=3 LOCALIZED STATE

singlet states ($|X, Y\rangle = (|+1\rangle \pm |-1\rangle)/\sqrt{2}$), where two linearly and orthogonally polarized dipoles ($|X\rangle$ and $|Y\rangle$) are defined along the principal axes of an elliptical QD (117, 118, 124). This also gives rise to the same splitting of the biexciton emission (Δ_{XY}), which involves the transition from biexciton to two singlet exciton states ($|X, Y\rangle$), respectively (125, 126). However, the energy difference for the perpendicular polarization in the XX spectrum (Fig.3.8 (d)) is nearly twice (~ 1.75 meV) that of X, where the angular delay of 90° is measured by the dumbbell-like trace of XX. We have also confirmed this phenomenon in QRs of different sizes.

When considering XX in this structure, two kinds of generation are possible; either two Xs in the same localised crescent structure or separate Xs located in two identical crescent structures are bound, respectively. Although the binding energy of the latter case was known to be sub-meV(16), the generation can be inhibited by the small size difference between the two crescent structures. For large GaAs QDs ($30 \sim 40$ nm in radius), the XX binding energy is known to be a few meV (127, 128). Therefore, the large binding energy (~ 5 meV) in this result is likely to arise from a localised XX, which consists of two Xs localised at the same crescent structure. The large asymmetric splitting ($\Delta_{XY} \sim 1.75$ meV) of the XX also supports a localised XX. When the symmetry is lowered, it is known that the selection rules change significantly (129, 130). This can give rise to an increase in the number of dipole-allowed transitions, i.e., a multitude of transitions between the two-exciton and one-exciton states, resulting in a broad PL spectrum for the XX. It is also noticeable that the XX PL spectrum in Fig.3.8 (d) is rather broad. Consequently, as shown schematically in Fig.3.8 (c), a multitude of transitions between the fine structure states of XX and X, which are denoted by the relative angular delay (θ), may result in twice the splitting when compared to the X for perpendicular polarizations because of the change in the ideal selection rules.

3.3 Polarization dependent time-resolved photoluminescence (TRPL) in exciton and biexciton states

Although the wavefunction distribution of the fine structure states is not clear, the oscillator strength difference of these states can be observed in terms of the size depen-

3.3 Polarization dependent time-resolved photoluminescence (TRPL) in exciton and biexciton states

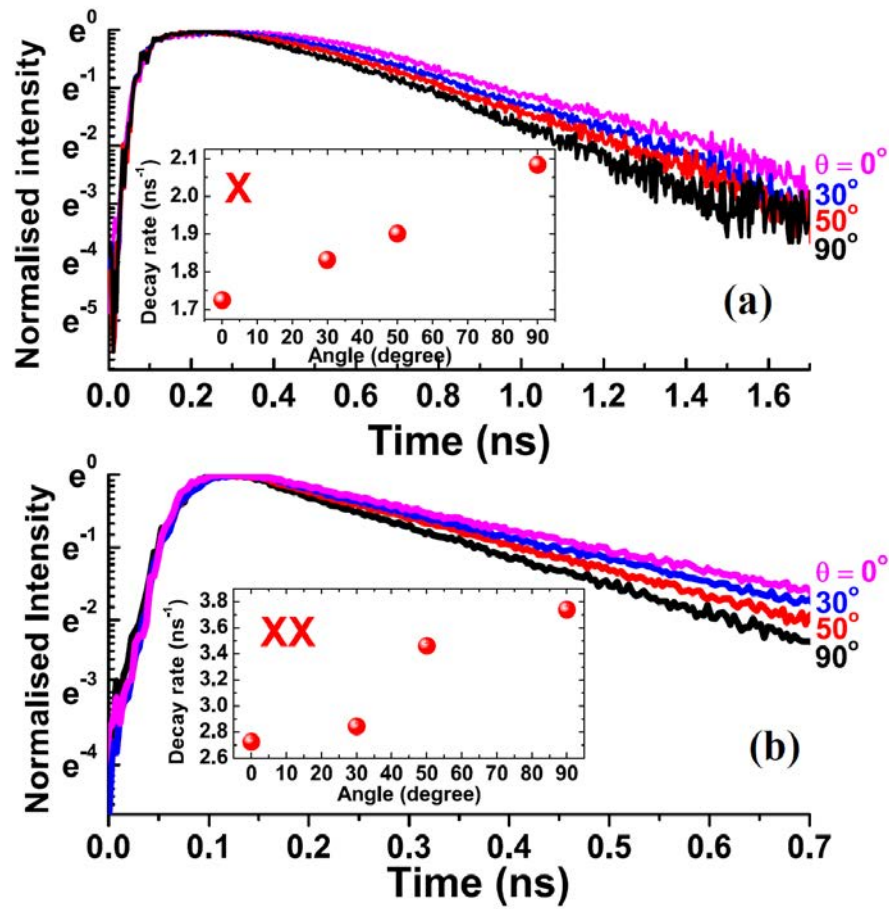


Figure 3.9: TRPL of the of the localised state of X (a) and XX (b) in a single QR measured at 1.6 kWcm^{-2} for various analyzer angles, where each PL rate shown in the inset.

3. POLARIZATION DEPENDENCE OF THE $k=3$ LOCALIZED STATE

dence of the PL decay rate, where the PL spectra for different confinement sizes are isolated by the analyzer angle. As shown in Fig.3.9, TRPL of X and XX was measured at various analyzer angles (θ), where the PL decay rates were obtained by a linear fit to the monotonic decay section on a log scale (shown in the inset). We found that the PL decay rates of both X and XX increase for increasing analyzer angle up to 90° . Interestingly, XX shows a novel feature in the size dependent oscillator strength. Since the vertical confinement is not ground state ($k = 3$), the size dependence is possibly dominated by lateral confinement. In the case of a disk-like QD structure formed at the interface fluctuation of a GaAs/AlGaAs quantum well, it was known that the oscillator strength goes to a minimum for a criterion QD radius $a_c \sim 6$ nm (131), which is smaller than the Bohr radius ($a_B = 13$ nm) of an exciton in bulk GaAs, and increases for both the small ($a < a_c$) and large radius ($a > a_c$). As shown in Fig.2.8 (b), the radial confinement size ($2a$) of a crescent-like structure is comparable to $2a_c \sim 12$ nm, which corresponds to the analyzer angle of 0° . On the other hand, for increasing the analyzer angle up to 90° , the states of larger confinement size ($a > a_c$) become resolved. Therefore, we conclude that these results are the case of large lateral confinement size ($a > a_c$), where the oscillator strength increases for size.

Whilst the radiative recombination of the e-h pair is characterized by a single exponential decay after ~ 400 ps, a plateau range is observed up to ~ 300 ps in Fig.3.9 (a). This may be associated with extended states of the electron. Initially, the e-h recombination occurs at the wavefunction overlap range between the localised electron and hole. However, extended state keep feeding the electrons to the localised state. State saturation in the plateau suggests the presence of a feeding source against the intra-relaxation of the localised electron ($k = 3$) to the lower states ($k = 2$ or $k = 1$). Furthermore, it is noticeable that the decay time (532 ± 56 ps) of the X is relatively longer than that seen in GaAs QDs (250 ± 50 ps) (124). When compared to the recombination rate of a hole near localised electrons, the recombination rate of a hole far from such localised electrons can be reduced. This effect possibly results in the reduction of the total decay rate in the $k = 3$ localised structure.

3.4 Chapter Summary

In conclusion, the presence of an asymmetric localised state in a single GaAs/Al_{0.3}Ga_{0.7}As QR was observed by its polarization dependence of the PL spectrum, which is in agreement with the adiabatic potential of a volcano-like anisotropic morphology and the polarization dependence of the PL spectrum. The fine structure states of the crescent-like adiabatic potential were resolved by changing the analyzer angle, whereby a large energy difference in the exciton (~ 0.8 meV) and biexciton (~ 1.75 meV) splitting was observed for perpendicular polarizations, and the analyzer-angle dependence of the PL intensity was mapped for an individual energy peak in the exciton PL spectrum, where a dumbbell-like trace was obtained with a 180°- period; the angular delay between traces varies with emission energy. Also, the oscillator strength differences were also compared in terms of the PL decay rate.

3. POLARIZATION DEPENDENCE OF THE $K=3$ LOCALIZED STATE

4

Excited excitons and biexcitons in localized states in a single quantum ring

In this chapter, the micro photoluminescence from a single GaAs quantum ring as a function of excitation power will be discussed. Excited and biexciton states of localised excitons in a single quantum ring have been investigated in terms of their dependence on excitation power, temperature, polarization asymmetry, and time-resolved photoluminescence (132, 133, 134). The excited and biexciton states are localised in a crescent-like structure in a quantum ring, and are observed to appear with increasing excitation power, whilst calculations show that saturation of the localised ground state exciton can be attributed to relatively fast dissociation of the biexciton (~ 430 ps) compared to the slow relaxation from the excited state to the ground state (~ 1000 ps), in agreement with time-resolved photoluminescence measurements. Large energy differences in the emission energy for perpendicular polarizations, a broad linewidth, and a large coefficient for optical-phonon interaction are found in the excited and biexciton states compared to the localised ground state. These results are attributed to a large polarity and selection rule change as a consequence of the asymmetric localised structure.

4. EXCITED EXCITONS AND BIEXCITONS IN LOCALIZED STATES IN A SINGLE QUANTUM RING

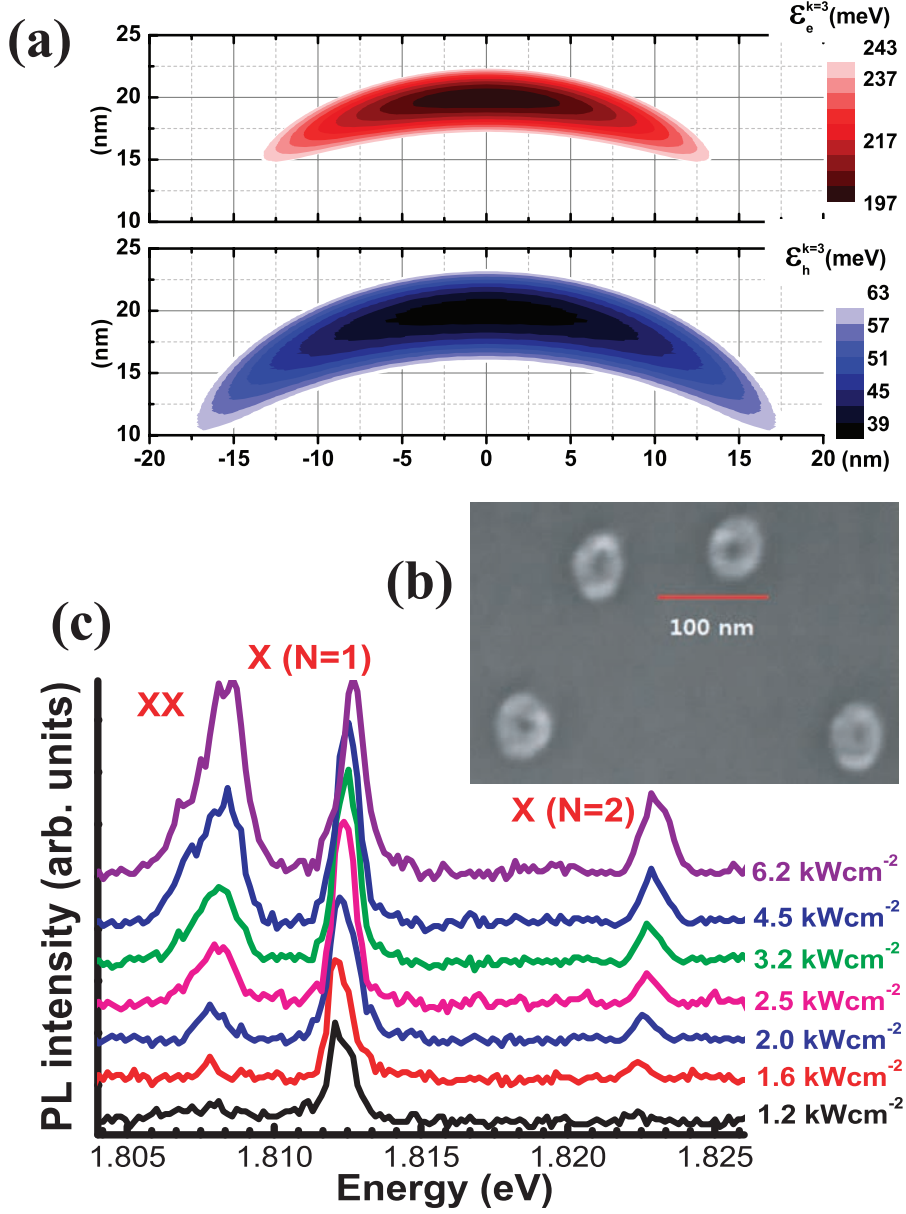


Figure 4.1: (a) Electrons and holes are localised in the crescent-like adiabatic potentials of the electron and the hole for a vertical quantum number $k = 3$ ($\epsilon_{e,h}^{k=3}$), respectively. (b) A single ring structure observed by FESEM. (c) Biexciton (XX) and excited-exciton ($X^{N=2}$) emission lines of the localised ground-state exciton ($X^{N=1}$) appear for increasing excitation power.

4.1 Power dependence of $X^{N=1}$, $X^{N=2}$, and XX

GaAs rings (27) were grown discussed in chapter 3. The sample was excited by frequency-doubled (400 nm) Ti:sapphire laser pulses (120 fs pulse duration at a 80-MHz repetition rate). The photoluminescence (PL) of a single QR was collected at 4 K using a confocal arrangement, and a time-correlated single photon counting system was used to obtain the time-resolved PL (TRPL) (135).

A volcano-like anisotropic morphology is present in the QR. The height anisotropy gives rise to a crescent-shaped adiabatic potential (18), and localisation of the potential becomes significant as the vertical quantum number is increased. For a QR with ~ 20 nm-radius and ~ 10 nm-height, the energy of the exciton states with vertical quantum numbers of $k = 1$ and $k = 2$ should be located near the bandgap of bulk GaAs and at ~ 1.7 eV, respectively. However, localised states for a vertical quantum number of $k = 3$ can be seen at an energy close to the barrier ($\text{Al}_{0.3}\text{Ga}_{0.7}\text{As}$) bandgap. As shown in Fig.4.1(a), localised adiabatic potentials ($\varepsilon_{e,h}^{k=3}$) of the electron and the hole for a vertical quantum number of $k = 3$ are crescent shaped up to an estimated ground state energy of (241 meV) for the electron and (60 meV) for the hole.

This leads to a predicted PL energy for the ground state exciton $X^{N=1}$ of ~ 1.812 eV, which is in excellent agreement with the PL spectrum in Fig.4.1 (c) and Fig.4.4 (a). It should be noted that the wavefunction contour areas should be larger than the localised potentials due to tunnelling effects. In particular, the tunnelling is dominant for the electron due to its shallow energy level with respect to the barrier. The blueshift in the PL from $X^{N=1}$ with increasing excitation power (Fig.4.1 (c)) suggests that fine structure states are filled in a sequential manner giving rise to the observed blueshift. Furthermore, the fine structure states of $X^{N=1}$ within the ~ 1.5 meV PL linewidth were observed by measuring the PL at different linear polariser angles (Fig.4.4 (a)), and are most likely associated with the crescent-like potentials (17, 136, 137, 138).

At previous reports ((27, 139, 140)), a single carrier level is calculated at both single QR and double QR structures with ignorance of the Coulomb interaction between an electron and a hole. In Figure 4.2, single carrier energy levels for electrons and heavy

4. EXCITED EXCITONS AND BIEXCITONS IN LOCALIZED STATES IN A SINGLE QUANTUM RING

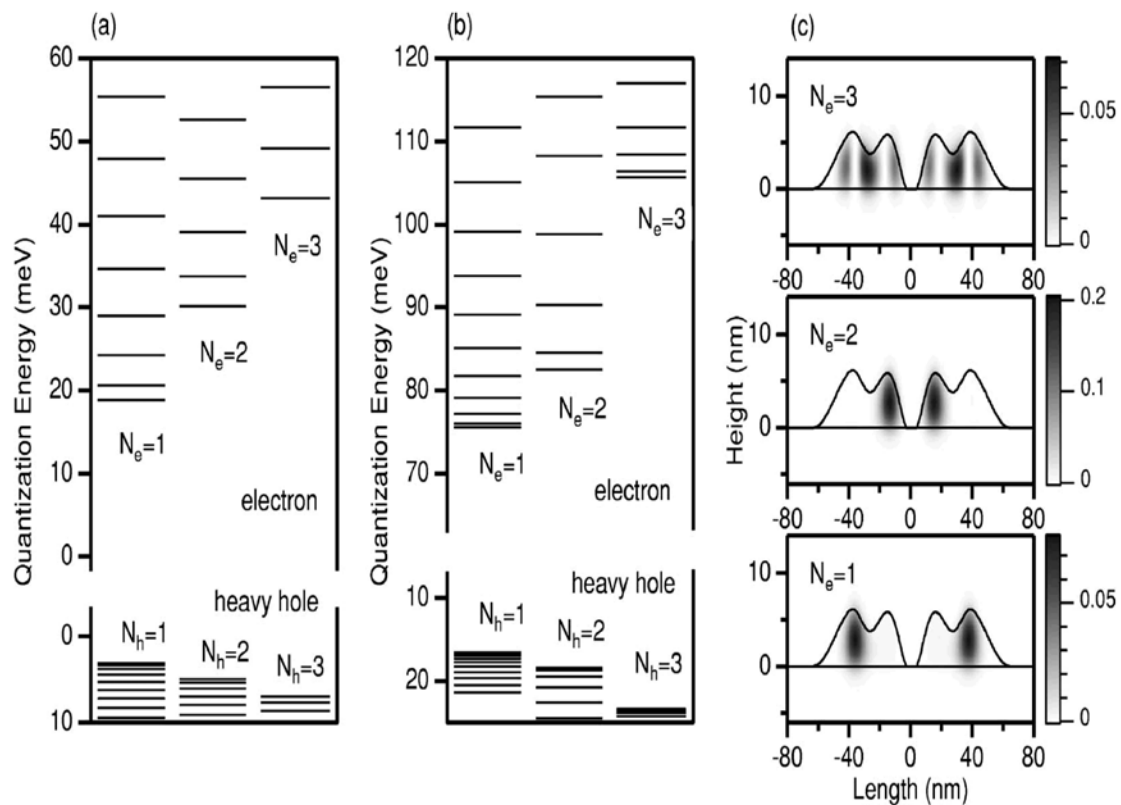


Figure 4.2: Single carrier energy levels in (a) QR and (b) DQR with lowest radial quantum numbers, $N_{e(h)}$, and various angular momentum (up to 10) are presented. (c) Electronic probability density in DQR for $N_e=1, 2,$ and 3 with $L=0$ (27).

4.1 Power dependence of $X^{N=1}$, $X^{N=2}$, and XX

holes are shown by radial quantum number $N_{e(h)}$ and azimuthal quantum number L which corresponds to the angular momentum. Two energy levels with $\pm L$ are degenerated at zero magnetic field (141, 142, 143). If the ring width is assumed negligible, energy levels are described by $E_{L_{e,h}} = (\hbar L_{e,h})^2 / (2m_{e,h}^* R^2)$. Based on these assumptions, the optical transition energies are calculated and shown in Figure 4.3 at both single and double QR structures. Even though the QR has an asymmetric structure, as long as a QR maintains cylindrical symmetry roughly, the exciton fine structure states (N, L) can be specified in terms of the additional azimuthal quantum number (L) , where the angular momentum of the rotational motion around a ring is quantized (144, 145, 146, 147). Given the ring radius ($R \sim 20$ nm) obtained from the FESEM image and the effective mass of electron (e) and heavy hole (h) in GaAs (27) ($m_e^* = 0.067m_0$ and $m_h^* = 0.51m_0$ with the electron rest mass m_0), up to seven degenerate fine structure levels ($L_{e,h} = 0, \pm 1, \pm 2, \pm 3$) are possible within the PL linewidth (~ 1.5 meV) of the X ($N = 1$) and X ($N = 2$) state. As the excitation power is increased, these fine structure states from X ($N = 1$) and X ($N = 2$) state are filled sequentially, giving rise to a blueshift (Figure 4.1 (c)).

As shown in Fig. 4.1(c), two additional PL peaks emerge at low (1.808 eV) and high energy (1.822 eV) with respect to $X^{N=1}$ (1.812 eV) as the excitation power (I_{ex}) is increased. The superlinear increase of the PL intensity ($\sim I_{\text{ex}}^\alpha$) was characterized in terms of the power factor (α) by integrating the PL spectrum. $\alpha \sim 2.3 \pm 0.1$ and $\sim 1.5 \pm 0.1$ were obtained for the low and the high energy peaks compared with $\alpha \sim 0.9 \pm 0.1$ measured for $X^{N=1}$ before saturation of the PL intensity. Therefore, the two additional peaks can be attributed to biexciton states (XX) and excited exciton states ($X^{N=2}$) of the localised $X^{N=1}$, respectively, where the radial quantum number N denotes the states defined in the adiabatic potential ($\varepsilon_{e,h}^{k=3}$) (148, 149, 150).

Both wavefunctions for XX and $X^{N=2}$ are possibly more extended and asymmetric than that of $X^{N=1}$. As $X^{N=2}$ is located ~ 10 meV above $X^{N=1}$, the range of $X^{N=2}$ is not extended significantly (\sim few nm) in the contour areas of $\varepsilon_e^{k=3}$ and $\varepsilon_h^{k=3}$. However, a node of the wavefunction must exist in the middle of the crescent structure similar to p -orbitals, possibly resulting in a large polarization dependence. On the other hand, since XX consists of two $X^{N=1}$ s, the area could be nearly doubled, but shrinks due

4. EXCITED EXCITONS AND BIEXCITONS IN LOCALIZED STATES IN A SINGLE QUANTUM RING

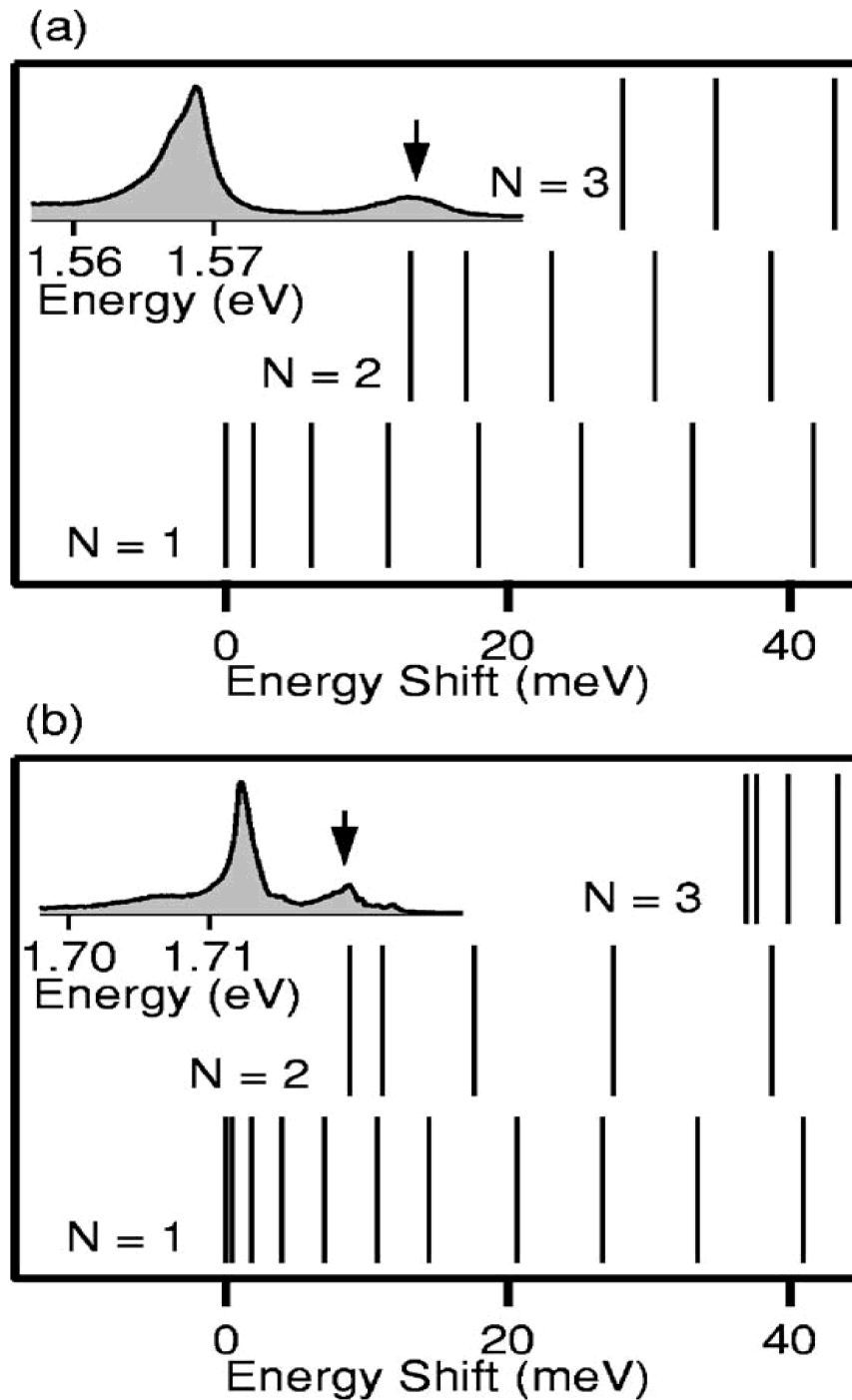


Figure 4.3: (a) Optical transition energies in a single QR at 15 kWcm^{-2} . (b) The energies of optical transitions in a DQR at 10 kWcm^{-2} (27).

4.2 Polarization dependence of $X^{N=1}$, $X^{N=2}$, and XX

to bonding. The observed binding energy of the XX (~ 4 meV) is comparable to the Coulomb interaction in bulk GaAs (~ 4.2 meV), but still far smaller than the confinement energy in this system. Therefore, the large range of XX in the crescent structure may also give rise to a large polarization asymmetry. In the following we have investigated effects of the range size and the asymmetry of the wavefunctions in terms of spectral linewidth, polarization asymmetry, and decay time.

4.2 Polarization dependence of $X^{N=1}$, $X^{N=2}$, and XX

Fig. 4.4 shows the polarization dependence in the PL for the $X^{N=1}$, $X^{N=2}$, and XX for an excitation power of 2 kWcm^{-2} . The presence of fine structure states associated with the crescent shape of the adiabatic potentials manifest themselves in the shape of the PL spectrum for different analyzer angles. The polarization dependence of the fine structure states was analyzed quantitatively by mapping the analyzer angle dependence of the PL intensity at different energies in polar coordinates. For instance, as shown in Fig.4.4 (d), dumbbell-like traces were obtained for $X^{N=2}$, where the maximum intensity of each PL spectrum is normalized. The relative azimuthal angle delay (θ) between the traces at different emission energies is compared to the PL spectrum at that analyzer angle. An energy difference for perpendicular polarizations (i.e., $\theta = 90^\circ$) can be used as a measure of the polarization asymmetry (18), whereby we found that XX and $X^{N=2}$ give a 2 and 1.5 times larger shift than that ($\Delta \sim 0.8$ meV) seen in $X^{N=1}$, respectively.

If the local structure was symmetric, selection rules would allow only transitions between $XX(\theta)$ and $X^{N=1}(\theta)$ with the same θ . Therefore, the same energy difference would be observed for perpendicular polarizations at $X^{N=1}$ and XX. However, the asymmetry in the crescent-like structure likely breaks down the selection rule (108, 110), whereby the increased number of transitions amongst the various $XX(\theta)$ and $X^{N=1}(\theta)$ transitions causes a broad linewidth and twice the splitting (2Δ) for perpendicular polarizations compared to that seen for $X^{N=1}$. On the other hand, the large polarization splitting (1.5Δ) of $X^{N=2}$ is possibly associated with the shape of the wavefunction, where a node is present as mentioned earlier. This may result in a relatively large level spacing between the fine structure states of $X^{N=2}$ compared to those of $X^{N=1}$ defined

4. EXCITED EXCITONS AND BIEXCITONS IN LOCALIZED STATES IN A SINGLE QUANTUM RING

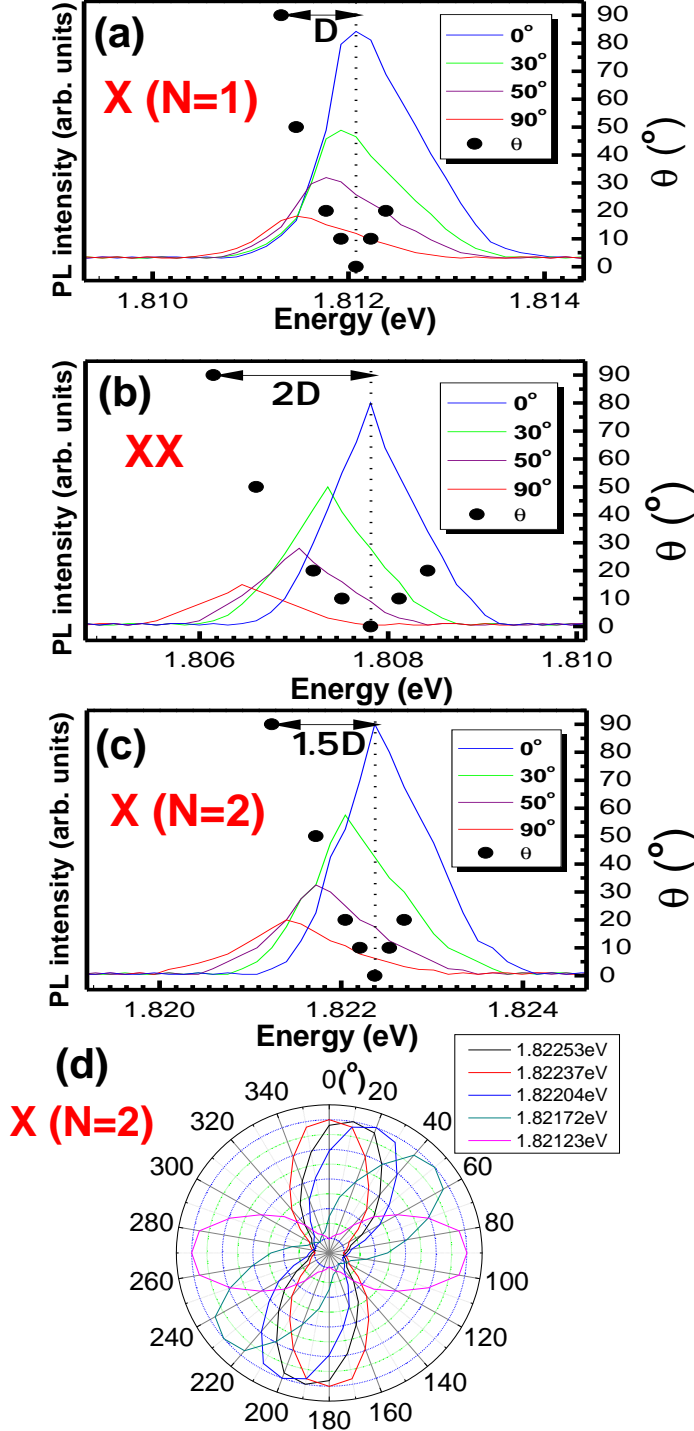


Figure 4.4: The PL spectrum of the $X^{N=1}$ (a), XX (b), and $X^{N=2}$ (c) at various analyzer angles in a single QR with an excitation power of 2 kWcm^{-2} . (d) Analyzer angle dependence of the PL intensity at different energies ($X^{N=2}$) gives dumbbell-like traces, where the maximum intensity of each PL spectrum is normalized, and the relative azimuthal angle delay (θ) between the traces is also plotted in the PL spectrum.

4.3 GaAs Q-ring PL temperature dependence measurements

in the asymmetric crescent-like structure. Additionally, the asymmetry possibly gives rise to a large polarity (18, 117, 118), whereby the optical-phonon interaction can be enhanced. This issue can be studied in terms of the broadening of the PL linewidth as a function of temperature (151).

4.3 GaAs Q-ring PL temperature dependence measurements

The ring's shape and size determine the energy levels of exciton states in our GaAs Q-ring. The shape of PL intensity curve by temperature dependence is similar to typical curves seen for the temperature dependence of QD samples (152, 153). In the low temperature regime, this curve tends towards a constant. At high temperatures, the curve tends towards a straight line. Above 90K, the GaAs Q-ring PL was quenched strongly. These results are well matched with our expectations of GaAs Q-ring. Because of strong confinement and increased exciton-exciton and exciton-phonon interactions, the Q-ring sample is much more sensitive to temperature than zero-dimensional QD samples.

We also cannot understand the intensity variation with temperature just based on thermal activation processes as in QD samples (154). In QD samples, the observed thermal quenching of the PL intensity is understood by an escape process of the dissociated excitons into the corresponding barriers. However, due to the ring structure (18), the escape process for a Q-ring of dissociated excitons is disturbed. The dissociated excitons can be trapped in the boundary between the Q-ring area and the barrier. Also, defects and dislocations in the AlGaAs/GaAs buffer will provide increased non-radiative channels to quench the luminescence and consequently reduce the efficiency of the thermal activation process. So it is not easy to deduce a thermal activation energy by only normal thermal activation processes in GaAs Q-rings, unlike GaAs QDs.

4.3.1 Temperature dependent PL spectrum

As shown in Fig.4.5 (a), the PL intensities for all three states decrease with increasing temperature, but the PL intensity of $X^{N=2}$ becomes relatively more dominant. As

4. EXCITED EXCITONS AND BIEXCITONS IN LOCALIZED STATES IN A SINGLE QUANTUM RING

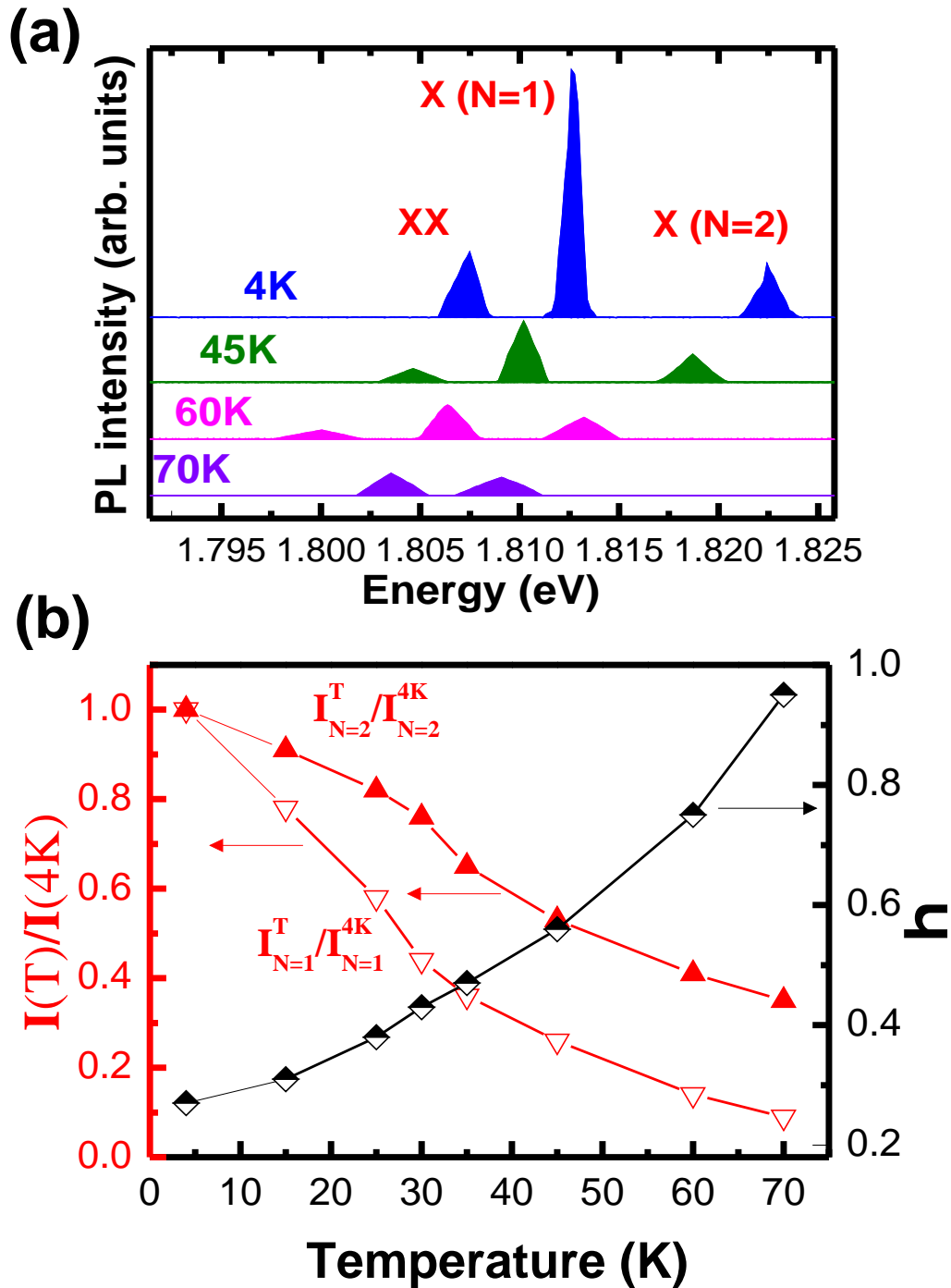


Figure 4.5: (a) Temperature dependence of the PL spectrum for $X^{N=1}$, $X^{N=2}$, and XX with the excitation of 2 kWcm^{-2} . (b) Temperature-dependent PL intensity normalized with respect to that at 4 K for $X^{N=1}$ and $X^{N=2}$, and the spectrally-integrated PL intensity ratio (η) of $X^{N=2}$ to $X^{N=1}$ for temperature.

4.3 GaAs Q-ring PL temperature dependence measurements

shown in Fig.4.5 (b), the dependence of the PL intensity on temperature, $I(T)$, is normalized with respect to that at 4 K, $I(4\text{K})$, and the ratio of the spectrally integrated PL intensity of the $X^{N=2}$ with respect to that of the $X^{N=1}$, $\eta(T) = \int I_{N=2}(T) d(\hbar\omega) / \int I_{N=1}(T) d(\hbar\omega)$, is also obtained as a function of temperature. In the case of strong excitation, both XX and $X^{N=2}$ are generated with the saturation of the $X^{N=1}$ states at low temperature. However, as the thermal energy becomes comparable to the binding energy of XX ($\gtrsim 67\text{K}$), the pairing of two $X^{N=1}$ states is significantly suppressed. On the other hand, the energy difference between $X^{N=1}$ and $X^{N=2}$ is reduced due to the larger γ_{ph} of $X^{N=2}$ compared to $X^{N=1}$, i.e. the difference in $\Delta E(T)$ in Fig.4.6. Consequently, thermal excitation from $X^{N=1}$ to $X^{N=2}$ becomes enhanced, giving rise to an increased growth rate for $\eta(T)$ as shown in Fig.4.5 (b).

4.3.2 Homogeneous linewidth and emission energy variation by temperature dependence

The temperature dependence of the homogeneous linewidth of the exciton is described by following formula:

$$\Gamma(T) = \Gamma(0) + S_{\text{ac}}T + S_{\text{op}} \frac{1}{\exp(\hbar\omega_{\text{LO}}/k_{\text{B}}T) - 1}, \quad (4.1)$$

(S_{ac} is exciton-acoustic phonon interaction coefficient, S_{op} is exciton-optical phonon interaction coefficient)

Here the linear term in temperature is due to exciton-acoustic phonon scattering, and the nonlinear term in temperature is due to exciton-LO phonon interaction. At low T ($k_{\text{B}}T \ll \hbar\omega_{\text{LO}}$), the linear scattering channel can contribute strongly. At high T , exciton-optical phonon interaction is more stronger than exciton-acoustic phonon interaction ($S_{\text{op}} \gg S_{\text{ac}}$). The linewidth broadening can be well fitted by formula (4.1) in Figure 4.5 with $\Gamma(0) \sim 0.79\text{ meV}$, $S_{\text{ac}} \sim 14\ \mu\text{eV/K}$ and $S_{\text{op}} \sim 132\text{ meV}$ for X ($N = 1$), $\Gamma(0) \sim 1.01\text{ meV}$, $S_{\text{ac}} \sim 14\ \mu\text{eV/K}$ and $S_{\text{op}} \sim 250\text{ meV}$ for X ($N = 2$) and $\Gamma(0) \sim 1.2\text{ meV}$, $S_{\text{ac}} \sim 14\ \mu\text{eV/K}$ and $S_{\text{op}} \sim 240\text{ meV}$ for XX. Where the temperature-independent linewidth ($\Gamma' = 1.51\Gamma_0(\text{XX}), 1.27\Gamma_0(X^{N=2})$) and the coefficient of optical phonon scattering ($S_{\text{op}} = 1.81S_0(\text{XX}), 1.89S_0(X^{N=2})$) for XX and $X^{N=2}$ were both found to be large compared to those for $X^{N=1}$ ($\Gamma_0 \sim 0.79\text{ meV}$, $S_0 \sim 132\text{ meV}$),

4. EXCITED EXCITONS AND BIEXCITONS IN LOCALIZED STATES IN A SINGLE QUANTUM RING

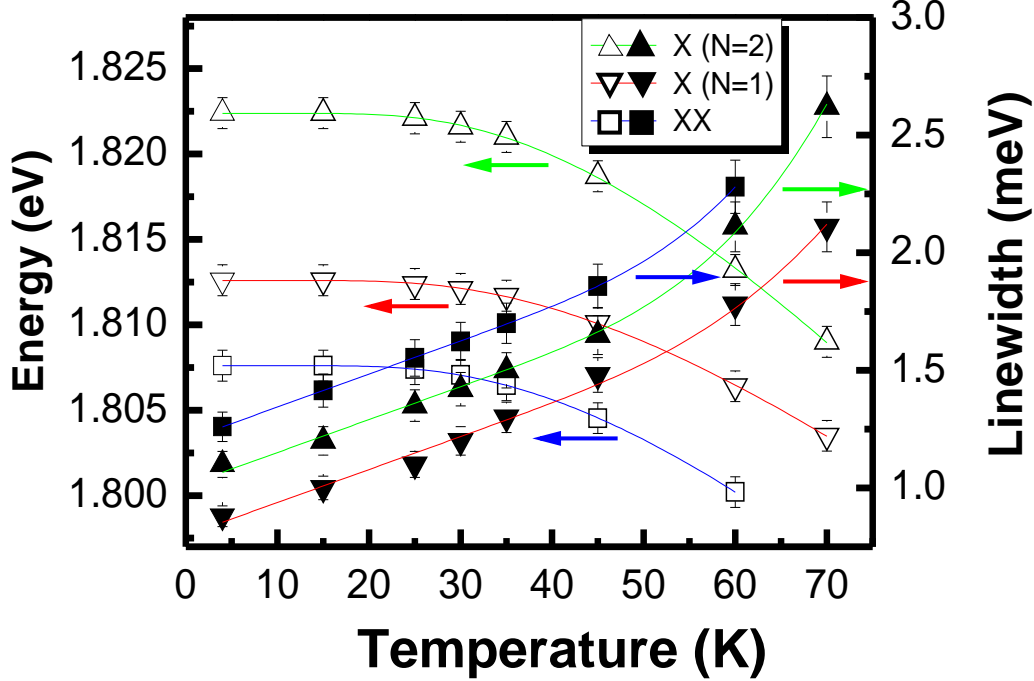


Figure 4.6: Temperature dependence of the PL energy (open) and the linewidth (filled) for $X^{N=1}$, $X^{N=2}$, and XX compared with Eq.4.1 and Eq.4.3

but no significant difference was found in the coefficient of acoustic phonon scattering ($S_{ac} \sim 14 \mu\text{eV}/\text{K}$) amongst all three lines $X^{N=1}$, $X^{N=2}$, and XX.

The temperature dependence of the exciton emission energy in the GaAs Q-ring is described in Figure 4.5. Below 20 K, the shift of the Q-ring gap is weaker than the shift at high temperature. At low temperatures, only long wavelength phonons can be excited. So the exciton-phonon interaction is weak below 20 K in GaAs Q-rings. We investigated the temperature-induced change in the band gap energy by the Bose-Einstein model. Usually, the band gap energy by temperature dependence is described by Varshni's formula.

$$E_g(T) = E_0 - aT^2/(T + b), \quad (4.2)$$

E_0 is the band gap energy at 0 K, a and b are Varshni's coefficients, b is proportional to the Debye temperature. However, if we consider phonon emission and absorption to

4.4 Time-resolved PL between X (N=1), XX and X (N=2)

understand the band gap change, the Bose-Einstein model (155) can well describe the temperature dependence of the band gap. In Figure 4.6, Bose-Einstein model describe the band gap energy variation in temperature dependence.

$$E_g(T) = E_0 - 2a_{\text{ph}}/(\exp(\theta_B/T) - 1), \quad (4.3)$$

Under Bose-Einstein model (Eq.4.3), E_0 is the band gap energy at 0K, a_{ph} represents the strength of exciton-average phonon (optical and acoustic) interaction and the fitting parameter θ_B is the average temperature of both acoustic and optical phonons. In Fig.3 (b), the obtained parameters are $E_0 \sim 1.8126$ eV, $a_{\text{ph}} \sim 34$ meV and $\theta_B \sim 150$ K for X ($N = 1$), $E_0 \sim 1.8224$ eV, $a_{\text{ph}} \sim 51$ meV and $\theta_B \sim 150$ K for X ($N = 2$) and $E_0 \sim 1.8076$ eV, $a_{\text{ph}} \sim 43$ meV and $\theta_B \sim 150$ K for XX. Where the coupling energy to the phonon bath for XX and $X^{N=2}$ ($a_{\text{ph}}=1.26a_0$ (XX), $1.50a_0$ ($X^{N=2}$)) was found also to be large compared to that of $X^{N=1}$ ($a_0 \sim 34$ meV) with an optimum effective phonon temperature of $\theta_B \sim 150$ K. As expected, these results confirm the stronger phonon interaction of XX and $X^{N=2}$ compared to that of $X^{N=1}$. It is also interesting that $X^{N=2}$ has a slightly larger S_{op} and a_{ph} than XX. This supports the conjecture of a large polarity in the $X^{N=2}$ state. We can confirm stronger linewidth broadening is attributed to strong exciton-LO phonon interaction and scattering between X($N = 1$), X($N = 2$) and XX, also stronger exciton-average phonon interaction is contributed to faster band gap change at X ($N = 2$) and XX.

4.4 Time-resolved PL between X (N=1), XX and X (N=2)

In order to investigate the relaxation amongst the three exciton states, time-resolved photoluminescence (TRPL) was measured at $X^{N=1}$ (1.8122 ± 0.0007 eV), $X^{N=2}$ (1.8225 ± 0.0005 eV), and XX (1.8078 ± 0.0003 eV), respectively. The excitation powers used in the measurements presented in Fig.4.7 (b) and Fig.4.7 (c) correspond to the onset of XX emission (1.6 kWcm^{-2}) and the saturation of the $X^{N=1}$ emission (6.2 kWcm^{-2}), respectively. As shown schematically in Fig.4.7 (a), the underlying dynamics can be

4. EXCITED EXCITONS AND BIEXCITONS IN LOCALIZED STATES IN A SINGLE QUANTUM RING

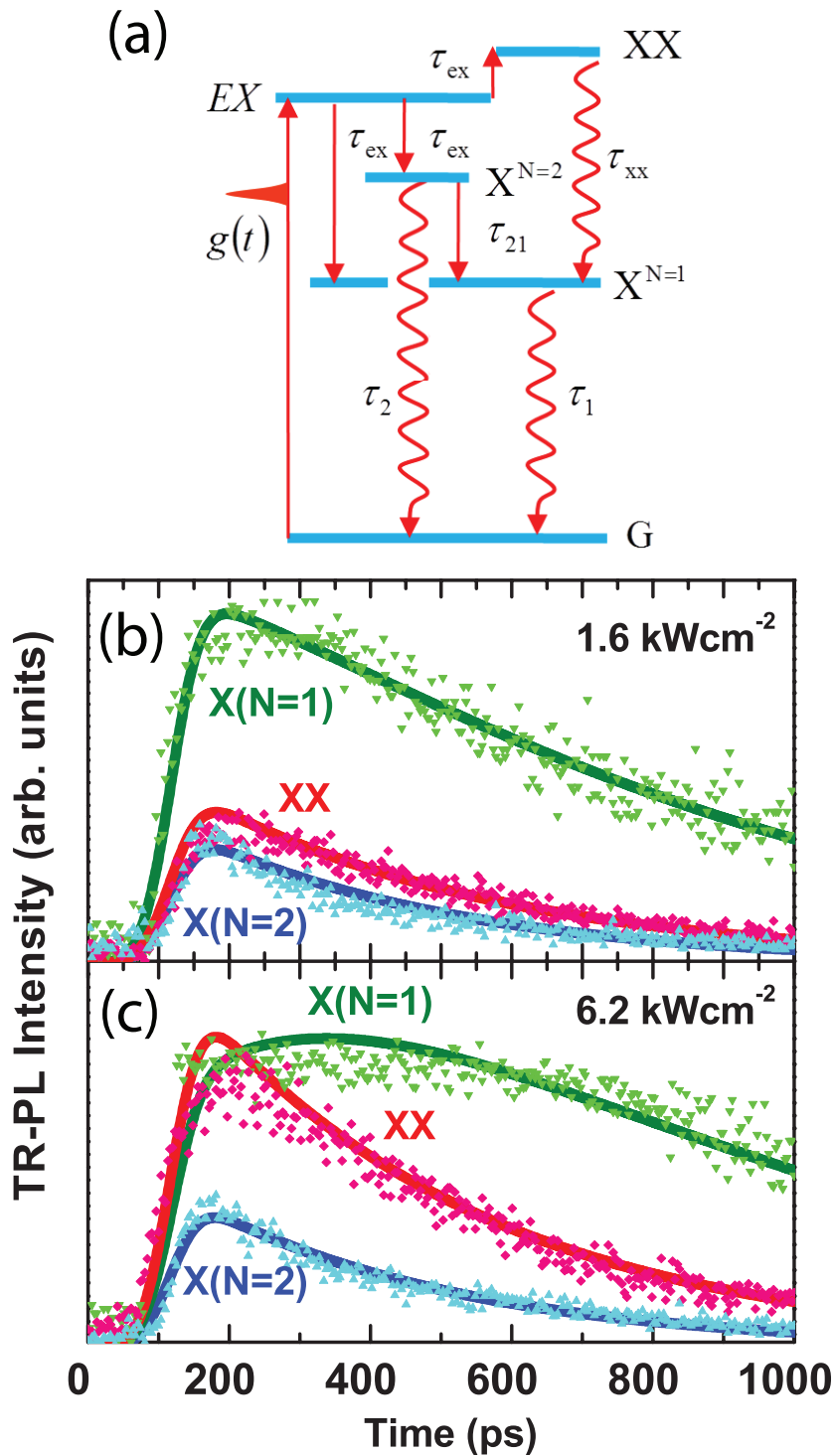


Figure 4.7: (a) Schematic diagram of the transitions between the energy levels of the excited (EX) state, $X^{N=1}$, $X^{N=2}$, and XX, where each of TR-PL was measured for an excitation power of 1.6 kWcm^{-2} (b) and 6.2 kWcm^{-2} (c). The calculations (solid lines) are in agreement with the experimental results (dots).

4.4 Time-resolved PL between X (N=1), XX and X (N=2)

modelled by using coupled rate equations for $X^{N=1}$, $X^{N=2}$, and XX:

$$\frac{dN_{\text{ex}}}{dt} = g(t) - \frac{N_{\text{ex}}}{\tau_{\text{ex}}}, \quad (4.4)$$

$$\frac{dN_{\text{xx}}}{dt} = \gamma \frac{N_{\text{ex}}}{\tau_{\text{ex}}} - \frac{N_{\text{xx}}}{\tau_{\text{xx}}}, \quad (4.5)$$

$$\frac{dN_{x_2}}{dt} = \alpha \frac{N_{\text{ex}}}{\tau_{\text{ex}}} - \frac{N_{x_2}}{\tau_2} - \frac{N_{x_2}}{\tau_{21}}, \quad (4.6)$$

$$\frac{dN_{x_1}}{dt} = \beta \frac{N_{\text{ex}}}{\tau_{\text{ex}}} + \frac{N_{\text{xx}}}{\tau_{\text{xx}}} + \frac{N_{x_2}}{\tau_{21}} - \frac{N_{x_1}}{\tau_1}. \quad (4.7)$$

Initially, carriers are generated in the excited state (denoted by ex) from the ground state by injection of a laser pulse ($g(t)$), which then relax quickly to $X^{N=1}$, $X^{N=2}$, and XX in a relaxation time (τ_{ex}). In the case of strong confinement, $X^{N=1}$ can be filled quickly in a few picoseconds via fast Auger scattering rather than by cascade relaxation (156). Because of the limited time-resolution of our TCSPC system (~ 50 ps), we cannot determine τ_{ex} , therefore the initial population of the $X^{N=1}$ (N_{x_1}), $X^{N=2}$ (N_{x_2}), and XX (N_{xx}) are given by multiplying the intra-relaxation rate ($1/\tau_{\text{ex}}$) by the weight factors (β , α , and γ), respectively, i.e., the initial carriers are distributed among $X^{N=1}$, $X^{N=2}$, and XX such that $\alpha + \beta + \gamma = 1$.

The XX dissociates into $X^{N=1}$ by radiative recombination during τ_{xx} , $X^{N=2}$ however, can either relax into $X^{N=1}$ or decay radiatively to the ground state. As a result, N_{x_1} can be enhanced by the intra-relaxation of $X^{N=2}$ or the radiative dissociation of XX. At an excitation power near the XX onset (1.6 kWcm^{-2}) (Fig.4.7 (b)), the PL decay time of $X^{N=2}$ is comparable to that of XX despite the presence of the two kinds of processes in the $X^{N=2}$. Therefore, the intra-relaxation between $X^{N=2}$ and $X^{N=1}$ is possibly slow, otherwise, N_{x_2} would show a faster decay than that of XX. When the initial weight factors ($\alpha = 0.2$ and $\gamma = 0.26$) of $X^{N=2}$ and XX are used, optimum time constants for the intra-relaxation ($\tau_{21} = 1000 \pm 20$ ps) and radiative recombination times of $X^{N=2}$ ($\tau_2 = 600 \pm 20$ ps), $X^{N=1}$ ($\tau_1 = 500 \pm 15$ ps), and XX ($\tau_{\text{xx}} = 450 \pm 10$ ps) are obtained. These results confirm that the N_{x_1} enhancement is dominated by N_{xx} .

A similar result has been obtained at the higher excitation power of 6.2 kWcm^{-2} , where the PL intensity of $X^{N=1}$ is saturated. When compared with the data for

4. EXCITED EXCITONS AND BIEXCITONS IN LOCALIZED STATES IN A SINGLE QUANTUM RING

1.6 kWcm⁻², the initial TRPL intensity of both X^{N=2} and XX is increased with respect to that of X^{N=1}, but no significant change in the decay dynamics of X^{N=1} and XX is seen (a slight change in the error bar; $\tau_{xx} = 430 \pm 10$ ps is observed). This result also agrees with our calculations. We found again that the N_{x_1} enhancement is attributed to N_{xx} ; the weight factor increase of XX ($\gamma = 0.44$) is critical whilst other constants barely change within the fitting error. Those results suggest that the relatively fast dissociation of XX fills up the X^{N=1} states, then the occupied states of X^{N=1} block the intra-relaxation between X^{N=2} and X^{N=1}.

4.5 Chapter Summary

In conclusion, we claim the presence of excited (X^{N=1}) and bi-exciton (XX) states of the localised ground state exciton (X^{N=1}) in a volcano-like single QR structure. Both X^{N=2} and XX show a large polarization asymmetry, a broad linewidth, and a strong optical phonon-interaction when compared to X^{N=1}. These are attributed to selection rule changes and a large polarity induced by the asymmetry arising from a local crescent-like structure in the QR. We also find that saturation of the X^{N=1} is dominated by fast dissociation of XX and slow intra-relaxation of X^{N=2}.

5

Optical properties of the $k=2$ delocalized state

Based on the theoretical calculations in Chapter 3, we deduce that the localization states of excitons are changed by the vertical quantum number. At the delocalized state ($k = 2$), micro photoluminescence (μ -PL) is observed as the excitation power is increased and shows a different trend when compared with that at the $k = 3$ localized state. Fine structure in the energy levels of the exciton and biexciton states is measured with a red shift seen when the excitation power is increased (157, 158, 159, 160, 161). This red shift is attributed to wavefunction delocalization as the power density increases. The polarization dependence is reduced by an increase in the power density. To help confirm this apparent power-dependent delocalization, time-resolved photoluminescence (TR-PL) measurements were undertaken at different power densities. We find an increased life time with increasing excitation power. Also, the QR size dependent polarization splittings are reduced from 0.8meV to 0.1meV as the exciton confinement energy is decreased (162, 163). These polarization splittings strongly support the variation of localization by vertical quantum number k .

5.1 Power dependent micro PL in the $k=2$ delocalized state

The power dependent photoluminescence is presented in Fig.5.1 (a). As shown Fig.5.1 (a), two additional PL peaks appear at lower (1.680 eV) and higher (1.688 eV) energy with respect to the ground state exciton (1.682 eV) as the excitation power is increased. The PL peak distribution looks similar to that seen for the $k = 3$ localized state in Chapter 4. However, the excess energy (6 meV) of the higher energy peak is decreased in comparison to the 10 meV excess energy for the excited exciton state ($N = 2$) in the $k = 3$ localized state for asymmetric single GaAs QRs.

The lower energy behaves as biexciton (XX) emission, due to its rapid rise relative to the exciton peak and the fast decay of the TR-PL (Fig.5.2 (a),(b)). Also, the superlinear increase of the PL intensity ($\sim I_{\text{ex}}^\alpha$) was characterized in terms of the power factor (α) by integrating the PL spectrum. $\alpha \sim 2.1 \pm 0.1$ and $\sim 1.5 \pm 0.1$ were obtained for the low and the high energy peaks compared with $\alpha \sim 1 \pm 0.1$ measured for $X^{N=1}$ before saturation of the PL intensity. The biexciton binding energy (2 meV) is also decreased at the delocalized $k = 2$ state when compared to the 5 meV biexciton binding energy at the localized $k = 3$ state (18). The decreased excited state binding energy and biexciton binding energy at the delocalized $k = 2$ state can be attributed to weak confinement due to wavefunction delocalization.

Asymmetry and anisotropy can also affect exciton energy levels which are calculated by the principal (radial) quantum number N ($=1,2,\dots$), and an azimuthal quantum number L , corresponding to the angular momentum (27, 34). Selection rule breaking for asymmetric and anisotropic structures was already reported in our previous results (18). Also in Fig.5.1 (a), the XX PL spectrum is rather broad. We already mentioned that if the QR symmetry is lowered, significant selection rule breaking from ideal optical transitions is expected by valence-band mixing and Coulomb interaction (108, 110). At the delocalized $k = 2$ state, this selection rule breaking is also observed because of asymmetry and anisotropy. Particularly in Fig.5.2 (b), a delay between the X ($N = 1$) and XX decay trace and a rounding of the X ($N = 1$) decay trace is observed. Both the delay time and the rounding effect can be explained by the refilling of X states by

5.2 Polarization dependence by power dependence

radiative decay of XX states which is described by the process $XX \rightarrow X + \text{photon}$. These effects have already been reported for both CdSe QDs (133) and InGaN QDs (164).

In Fig.5.1(a), as the excitation power is increased, exciton state and biexciton state peaks show a redshift. The fine structure energy levels of the ground state exciton ($N = 1$) are examined in more detail in Fig.5.1 (b). The ground state exciton ($N = 1$) peak shifts from 1.6820 eV to 1.6816 eV (0.4 meV red shift) with increasing excitation power density. A similar redshift is also measured at the excited state exciton ($N = 2$) and biexciton (XX) energy peaks. This redshift can be attributed to an increase of the wave function density. At low excitation power, carrier wave function is existed as a delocalized state. However, as the excitation power is increased, the carrier density will increase continuously. In other words, the carrier wave function will be delocalized more at high excitation power than that at low excitation power in delocalized $k = 2$ state. At low excitation power, the carrier wave function is distributed in a shape like a collapsed donut on the volcano-like QR structure. As the excitation power is increased, the carrier wave function changes to a complete donut-shaped wave function for the QR. To confirm this wave function state variation, power dependence polarization change and time-resolved PL at $X(N = 1)$ is presented in Fig.5.3. If the wave function is delocalized by excitation power increase, the polarization dependence will decrease and life time will increase.

5.2 Polarization dependence by power dependence

As shown in Fig.5.3, the PL spectrum was measured at different power densities. It exhibits a polarization dependence change for the ground exciton state ($X (N = 1)$) from 1.6 kWcm^{-2} to 6.2 kWcm^{-2} . In Fig.5.3 (a), the polarization-dependent energy difference is 0.27 meV for the ground state exciton ($X (N = 1)$) at 1.6 kWcm^{-2} . This energy difference is attributed to an asymmetric electron-hole exchange interaction. The two orthogonally polarized states of $|X\rangle$ and $|Y\rangle$ can be spectrally isolated by a linear polarizer. A splitting (Δ_{XY}) of the double exciton state ($|\pm 1\rangle$) into two singlet states ($|X, Y\rangle = (|+1\rangle \pm |-1\rangle)/\sqrt{2}$) is possible, where two linearly and orthogonally

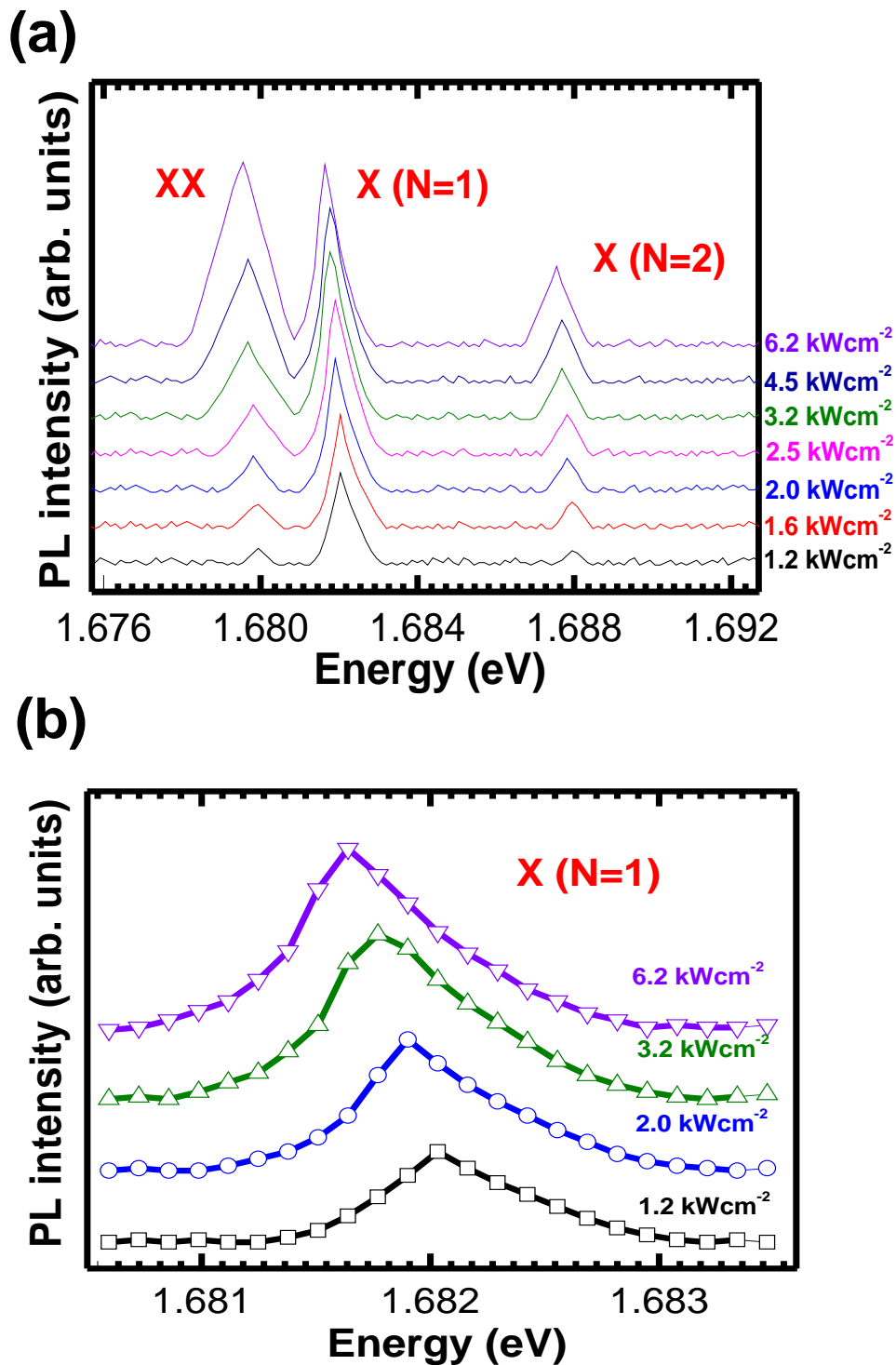


Figure 5.1: (a) Excited X ($N = 2$) and XX states appear from a single GaAs QR with increasing excitation power. The exciton and biexciton states are also red-shifted due to the delocalized wave function. (b) The fine structure of the X ($N = 1$) state PL spectrum, which red-shifts.

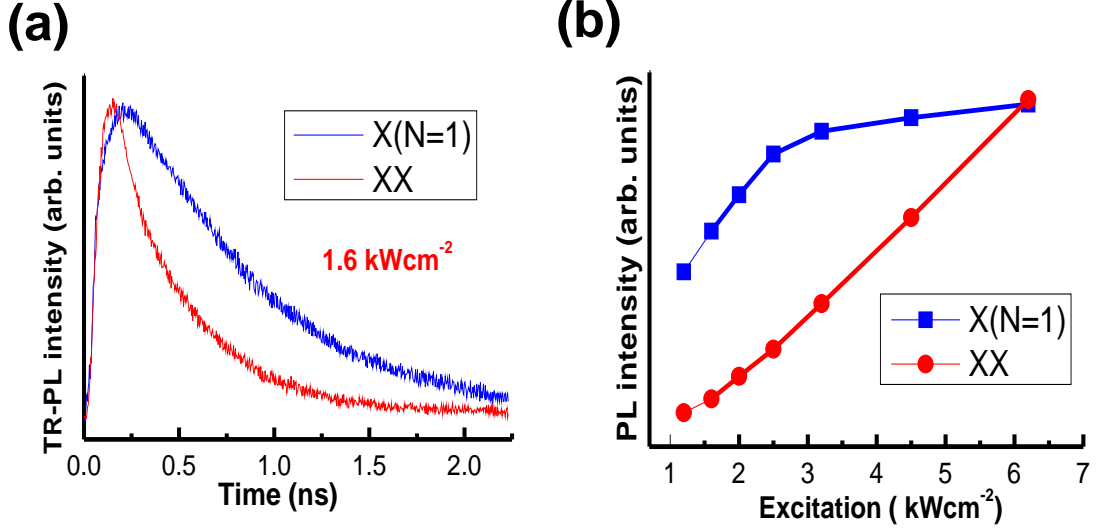


Figure 5.2: (a) TRPL of X ($N = 1$) and XX. (b) PL intensity from XX is compared with that from X ($N = 1$) as the excitation power is increased at the delocalized state $k = 2$.

polarized dipoles ($|X\rangle$ and $|Y\rangle$) are defined along the principal axes of an asymmetric structure.

The PL spectrum exhibits a weak polarization dependence relative to that at the localized $k = 3$ state. The energy difference by polarization angle change was 0.8 meV for the ground state exciton (X ($N = 1$)) at the localized $k = 3$ state with excitation density of 1.6 kWcm^{-2} as shown in Fig.5.5 (b) (18). In Fig.5.3 (a), the polarization splittings were measured to be 0.27 meV at 1.6 kWcm^{-2} , 0.18 meV at 3.2 kWcm^{-2} and 0.1 meV at 6.2 kWcm^{-2} , respectively. The polarization dependence decreased as the exciton power increased. This means that the energy differences between lineally and orthogonally polarized dipoles decrease as the wave function is delocalized. The PL spectrum indicates a red-shift as the analyser angle increases, but the PL intensity decreases significantly at all different excitation power densities. At the low excitation power density (1.6 kWcm^{-2}), the measured life time is 870 ps which is longer than the 650 ps seen for the $k = 3$ localized state with 1.6 kWcm^{-2} excitation Fig.5.3 (b). It is expected that the carrier life time will increase as the wave function is delocalized due to a decrease in the confinement energies. In Fig.5.3 (a), we already confirmed

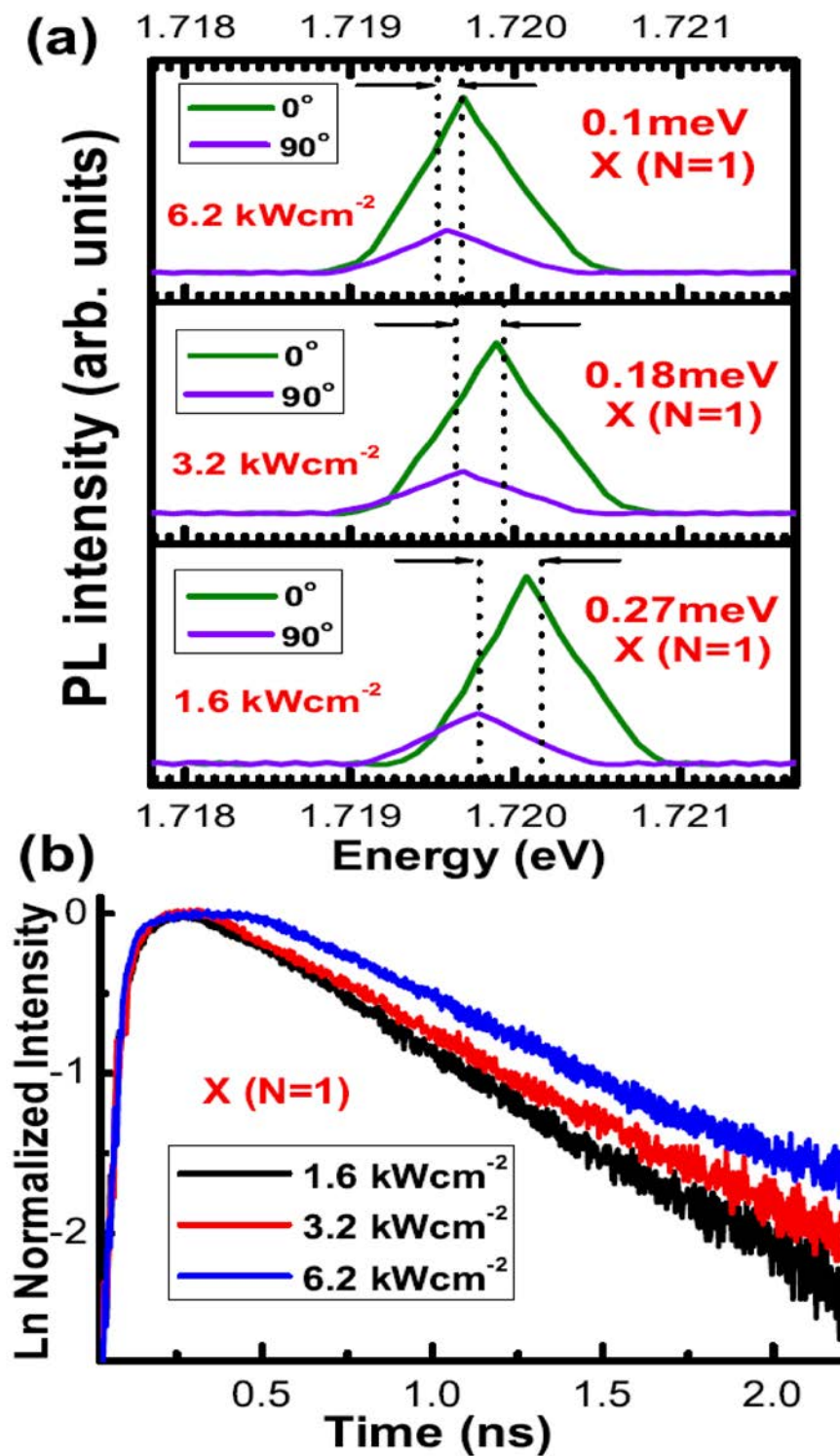


Figure 5.3: (a) PL spectrum of the X ($N = 1$) from 1.6 kWcm^{-2} to 6.2 kWcm^{-2} under rotating analyzer angles in a single QR. (b) TRPL of the delocalized state of X ($N = 1$) from 1.6 kWcm^{-2} to 6.2 kWcm^{-2} .

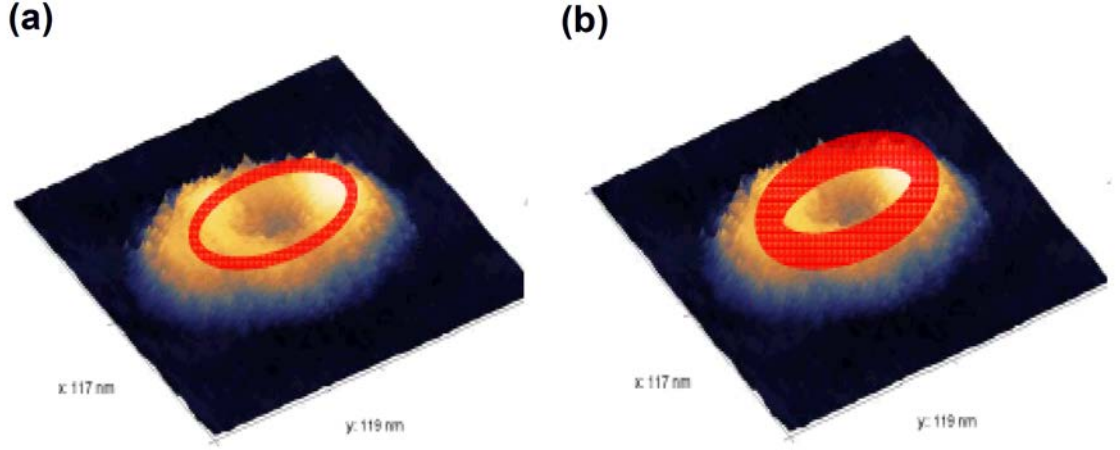


Figure 5.4: (a) localization for low power density (b) localization for high power density.

that the carrier wave function was extended and delocalized following an increase in the excitation power density. To verify the wave function delocalization, time-resolved decay traces for X ($N = 1$) were measured at different power densities and presented in Fig.5.3 (b). As the excitation power is increased, the life time of X ($N = 1$) state increases from 870ps at 1.6 kWcm^{-2} to 1ns at 6.2 kWcm^{-2} . This increased life time supports the delocalization of the wave function with increasing power density. If the wave function of the carriers were not delocalized, the life time would be expected to be shortened as the power density increased. However, an increased life time is seen as the carrier wavefunction is delocalised as shown in Fig.5.3 (b).

These polarization-dependence and time-resolved results with increasing excitation power density strongly support the variation of the carrier wave function. Fig.5.4 shows how the carrier wave functions change with excitation power density. It shows a delocalized carrier distribution at the delocalized $k = 2$ state which was expected from the theoretical calculations in Chapter 3 for the low excitation power density in Fig.5.4 (a). The carrier wave function is definitely covered the whole area. However, as the excitation power density is increased, the carrier wave function becomes more delocalized. Fig.5.4(b) shows that the carrier wave function is strongly delocalized at high excitation power density.

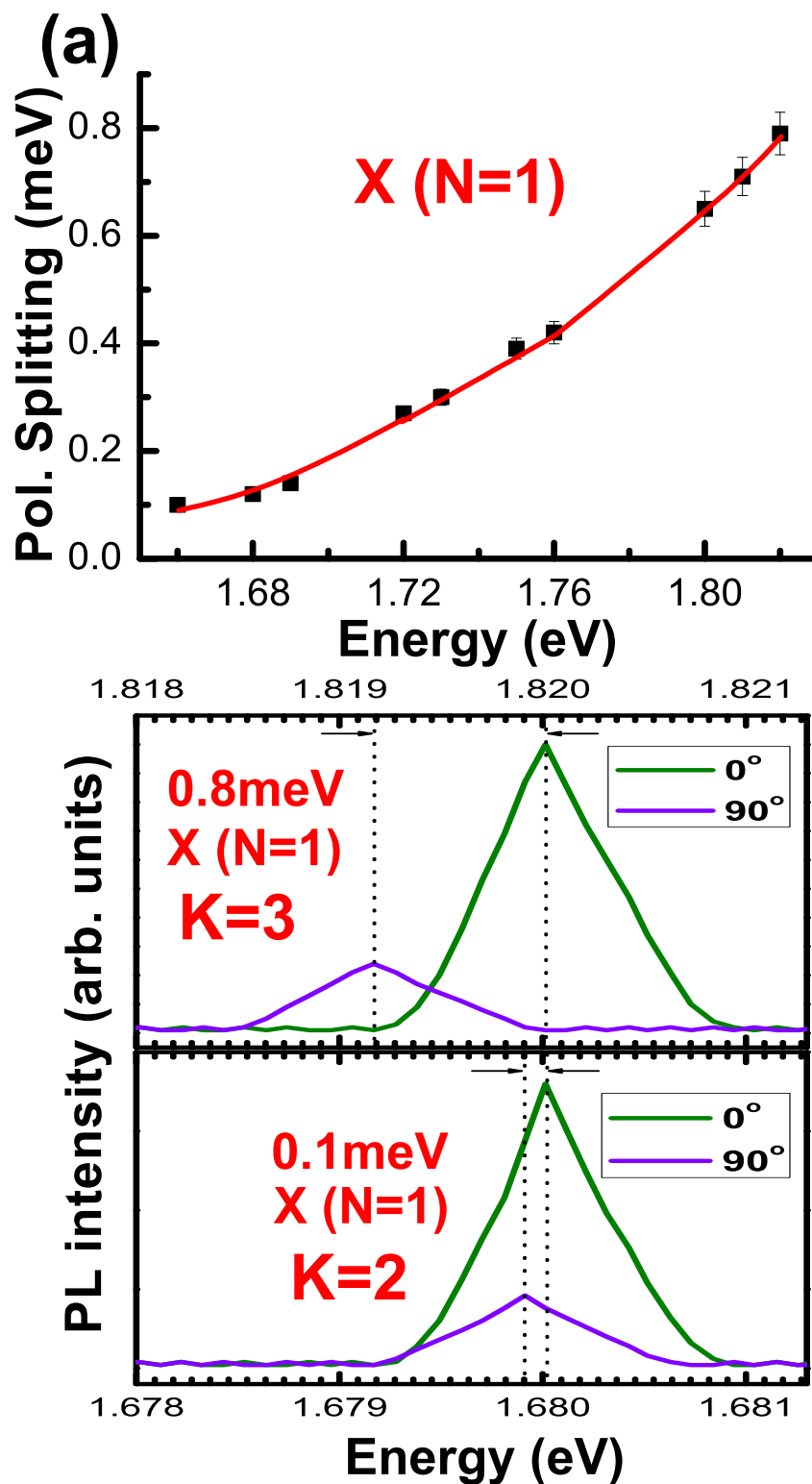


Figure 5.5: The polarization splittings of the $X (N = 1)$ at different confinement energies (a), Comparison of polarization splittings of $X (N = 1)$ between the localized $k = 3$ state and the delocalized $k = 2$ (b).

5.3 Polarization dependence on ring size

We present polarization splittings for various confinement exciton energies in asymmetric QRs in Fig.5.5 (a). The lower the exciton confinement energies are for the QR, the smaller are the polarization splittings seen. This result again strongly supports the assertion that wavefunction localization of the exciton state determines the polarization splittings. In an elliptical QD, the polarization splitting is reported to be 0.1meV by isolation between two orthogonally polarized states of $|X\rangle$ and $|Y\rangle$. However, in an asymmetric QR, the polarization splittings are distributed over a wide range as shown in Fig.5.5 (a). The strong polarization splitting in the $k = 3$ localized X ($N = 1$) state is compared with the weak polarization splitting in the $k = 2$ delocalized X ($N = 1$) state in Fig.5.5 (b).

Based on atomic force microscope (AFM) images of uncapped GaAs QRs (18), a realistic QR morphology is two asymmetric crescent structures. Under these two separate crescent structures, the adiabatic potential $\varepsilon^k(r, \phi)$ can be obtained by solving the vertical part of the Schrödinger equation. Theoretical calculations of the adiabatic potential $\varepsilon^k(r, \phi)$ suggest that the vertical state $k = 3$ is a criterion for a localization. Up to $k = 2$, the wave function of the ground state exciton exists all around the two crescent structures. However, for $k = 3$, the wave function is strongly confined in the bigger crescent structure. So, the wave function of $k = 3$ is localized under strong confinement. The more extended and delocalized wavefunction is less vulnerable to the asymmetry and anisotropy. So, in Fig.5.5 (a), we can deduce that wave function localization makes a difference for polarization splittings. As the exciton confinement energy is decreased, the polarization splittings also decrease (165).

5.4 Conclusion

In conclusion, we have shown that the fine structure of the exciton and biexciton states at the delocalized $k = 2$ state are red-shifted due to the carrier wave function delocalization. The energy difference by polarization is decreased at the $k = 2$ state and also decreases continuously with increasing excitation power density. This reduced polarization dependence strongly supports the existence of a delocalized wave function

5. OPTICAL PROPERTIES OF THE $k=2$ DELOCALIZED STATE

in the QR. To confirm this delocalization, a time-resolved PL was measured at various excitation power densities. An elongated life time with increasing power density implies wave function delocalization due to weak confinement energies. As the various exciton confinement energies vary, the polarization splittings change from 0.8 meV at the localized $k = 3$ state to 0.1 meV at the delocalized $k = 2$ state.

6

Aharonov-Bohm effect in a single QR

6.1 Why Aharonov-Bohm oscillation in a single QR

A canonical manifestation of the Aharonov-Bohm (AB) effect occurs in an experiment in thin solenoid that bears the magnetic flux ϕ in Fig.6.1. In quantum mechanics, the same particle can move between two different points by a variety of paths. So, this phase difference can be obtained in a solenoid between the slits of a double-slit experiment in Fig.6.1. An ideal solenoid encloses a magnetic field B , but there is no magnetic field outside of solenoid cylinder. Therefore, the charged particle passing outside of a solenoid experiences no magnetic field B . However, there is a vector potential A outside of a solenoid cylinder with enclosed flux. The relative phase between different particles passing through one slit or the other slit can be changed by whether the solenoid current is turned on or off.

Recently, quantum ring (QR) structure is of great interest for the optical Aharonov-Bohm (AB) effect, which is analogous to the oscillation of conductance as a function of magnetic flux in an AB interferometer made of a quantum point contact(167, 168). So far, the optical AB-like oscillations have been observed in charged excitons and type-2 quantum dots (QD)(48, 169). However, convincing experiments on the neutral excitonic AB effect is limited(170, 171). The optical Aharonov-Bohm effect is an interesting physical phenomenon that occurs in neutral excitonic systems in which the charge

6. AHARNOV-BOHM EFFECT IN A SINGLE QR

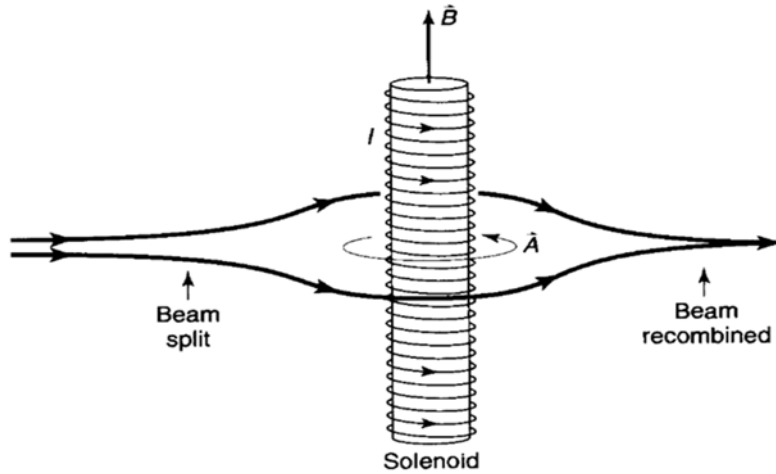


Figure 6.1: Schematic picture of magnetic Aharnov-Bohm effect(166).

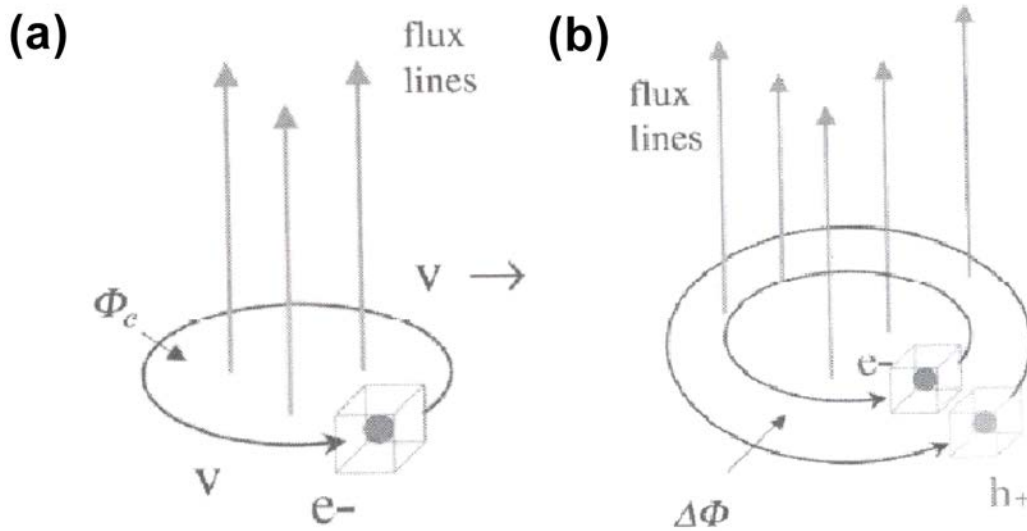


Figure 6.2: (a) The AB effect for a charged particle depends on the magnetic flux (b) For a neutral exciton, the magnetic flux in a closed cylindrical geometry depends on the difference in their relative rotation(3).

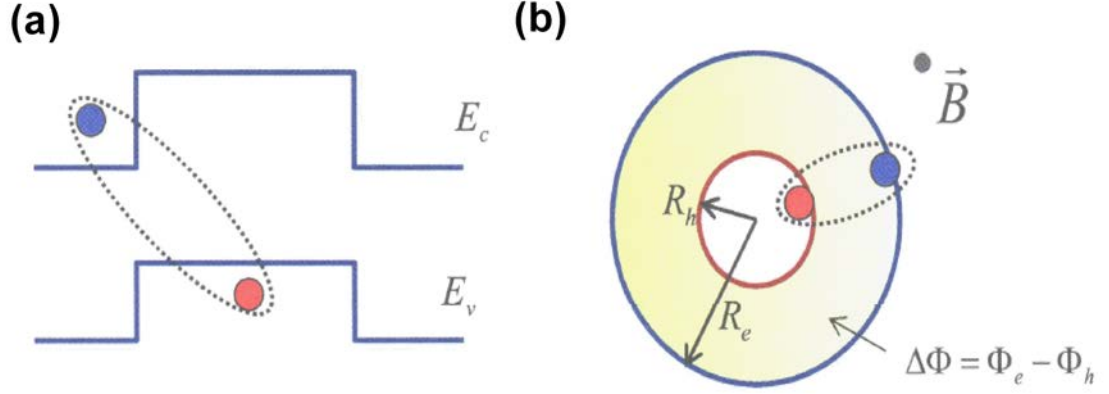


Figure 6.3: (a) Schematic band structure of a single QR. (b) Electron and hole are moving on concentric ring trajectories in the presence of a perpendicular magnetic field. The magnetic flux $\Delta\phi$ through the area between the two trajectories creates a topological Aharonov-Bohm phase in the exciton wavefunction(3).

carriers are confined and polarized in Fig.6.2. A magnetic field which is penetrating the enclosed area of charge carries determines a phase shift of their wavefunctions proportional to the magnetic flux. Normally, the AB effect is observed in charged system, however the neutral exciton in a single QR structure are strongly polarized along the radial direction of a circular orbit in Fig.6.2 (b). So, the magnetic flux area which determines a phase shift of AB effect depends on the radius difference between an electron and hole. One simple model for a neutral exciton, a bound electron-hole pair in a QR is a system with two circular orbits for the carriers in Fig.6.3 (a). If the electron and hole are uncoupled (like very weak Coulomb attraction) and move on two rings with different radius R_e and R_h , in the presence of an external magnetic field, the energy of the electron-hole pair takes

$$E_{exc} = E_g + \frac{\hbar^2}{2m_e R_e^2} \left(l_e + \frac{\phi_e}{\phi_0} \right)^2 + \frac{\hbar^2}{2m_h R_h^2} \left(l_h - \frac{\phi_h}{\phi_0} \right)^2, \quad (6.1)$$

where E_g is term that includes the band gap energy, l_e and l_h represent the angular momenta of the electron and hole, respectively. ϕ_0 is the flux quantum (h/e). The magnetic field B enters through the magnetic fluxes $\phi_e = \pi R_e^2 B$ and $\phi_h = \pi R_h^2 B$ which describe the quantum phases accumulated by the wave function of particles.

6. AHARNOV-BOHM EFFECT IN A SINGLE QR

This equation assumes non-interacting electron and hole, an independent motion of the carriers. If a strong Coulomb attraction between the particles is included, they will rotate together as shown in Fig.6.3 (b). ; the exciton is described by

$$E_{exc} = E'_g + \frac{\hbar^2}{2MR_0^2} \left(L + \frac{\Delta\phi}{\phi_0} \right)^2, \quad (6.2)$$

where $L=l_e + l_h$ is the total momentum of an exciton, $R_0=(R_e + R_h)/2$, and $M=(m_e R_e^2 + m_h R_h^2)/R_0^2$. The magnetic field penetrates via the magnetic flux, $\Delta\phi$, through the area between the particle path area in Fig.6.3 (b). :

$$\Delta\phi = \phi_e - \phi_h = \pi B(R_e^2 - R_h^2). \quad (6.3)$$

6.2 The Aharnov-Bohm oscillation in a localized state $k = 3$

As the exciton state is strongly localized (already confirmed in the previous chapters), delocalisation around the whole rim in a QR is unlikely. However, provided that an external magnetic field (B) is strong enough to overcome the energy barrier between the two separate localised states in an anisotropic QR, a phase coherent delocalisation can be induced; as persistent current(17) was induced in an anisotropic QR beyond ~ 14 T, it is challenging to observe an induced excitonic AB oscillation in an anisotropic QR beyond a threshold magnetic field.

We measured magneto-PL of localised excitons (Fig.6.4 (a)) at around energy ($E(0) = 1.781$ eV) in the absence of B compared to the $X^{N=1}$ (1.812 eV) in Fig.4.1 (chapter 4), which possibly gives rise to more extended localised structure and a reduced threshold magnetic field. Spectral splitting of the localised excitons in an anisotropic QR becomes significant when $B \gtrsim 4$ T, where the Zeeman splitting becomes comparable to the energy difference for perpendicular linear polarizations (~ 2 meV), similar to the case of asymmetric quantum dots(117). The high ($E(\sigma^-)$) and low energy ($E(\sigma^+)$) of the exciton for B (Fig.6.4 (b)) were obtained by Lorentzian fitting, whereby exciton g -factor ($g_X = [E(\sigma^+) - E(\sigma^-)]/\mu_B B \sim -0.2$) and diamagnetic coefficient

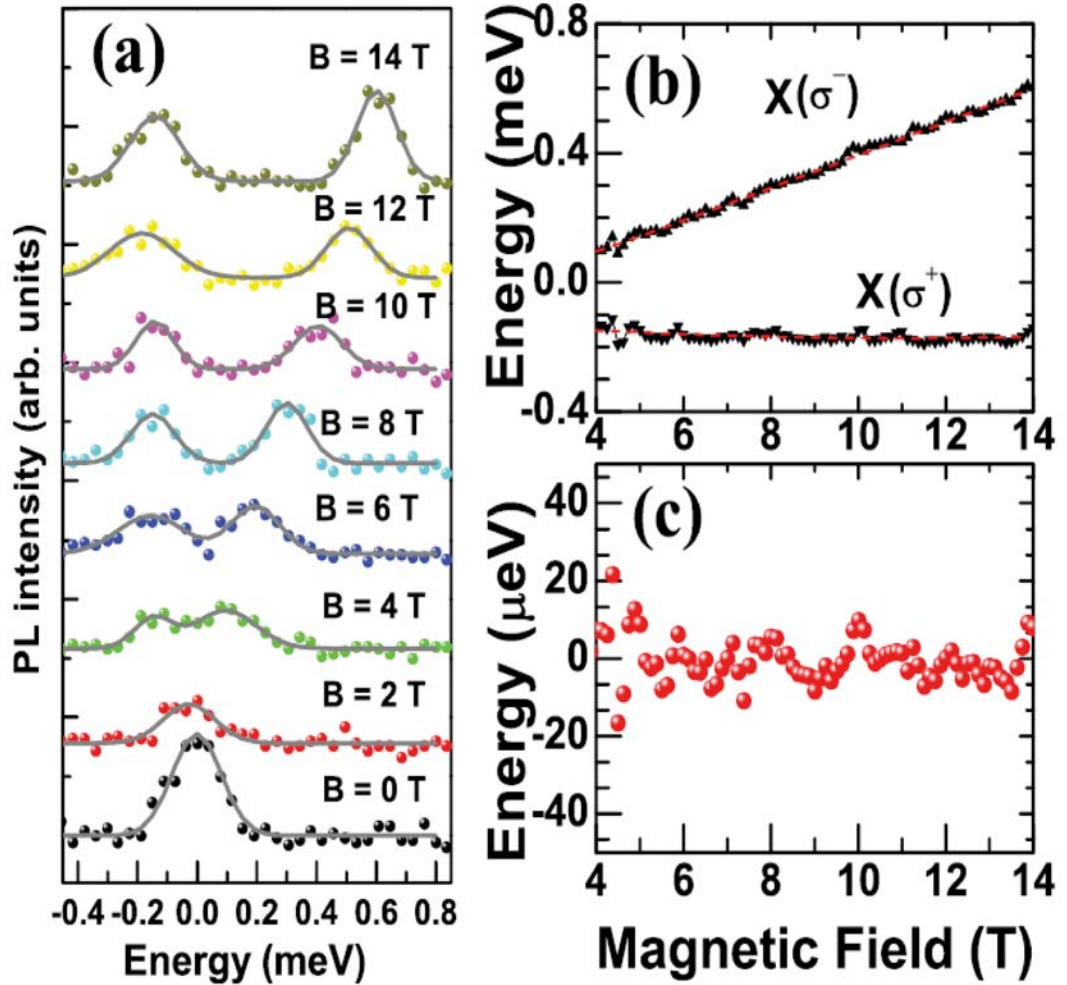


Figure 6.4: The PL spectrum (a) and fitted peak energy (b) of localized exciton Zeeman doublet with increasing an external magnetic field, where the energy oscillation is not significant with an error range of $20 \mu\text{eV}$ after removing Zeeman splitting and diamagnetic shift (c).

6. AHARNOV-BOHM EFFECT IN A SINGLE QR

($\gamma = \frac{[E(\sigma^+) + E(\sigma^-)]/2 - E(B=0)}{B^2} \sim 1.3 \mu\text{eVT}^{-2}$) were also obtained.

These small values can be attributed to the small lateral area of local structure. After removing the Zeeman splitting and diamagnetic shift (Fig.6.4 (c)), an energy drifting for B is seen in an range of $20 \mu\text{eV}$. However, it is difficult to define a significant period. It is therefore possible that 14 T is an insufficient field to produce a phase coherent delocalization around the whole QR.

6.3 Chapter summary

In conclusion, magneto-micro PL at strongly localized state is investigated from 0 T to 14 T. We conclude a phase coherence around the whole rim is inhibited in the case of strong localization, resulting in no significant excitonic AB oscillations up to 14 T. Based on our works, the degree of localization is a important factor to observe the AB oscillation at asymmetric QR structure.

7

Optical properties of other samples

7.1 Single Walled Carbon Nanotubes

Structurally, carbon nanotubes are made up of sp^2 bonded carbon atoms which behave like rolled up sheets of graphene. Single walled carbon nanotubes (SWCNTs) are an especially interesting material in condensed matter physics. They are ideal prototype materials to investigate 1-D physics and strong Coulomb correlations and have been discovered to exhibit exotic Luttinger liquid physics. Their electronic properties are very sensitive to their microscopic structure and symmetry, covering a wide energy spectrum. So they can be either metallic or semiconducting with varying bandgaps upon their diameter and chirality.

7.1.1 Introduction to single walled carbon nanotubes

Carbon nanotubes were discovered in 1991 (173) and have been found to exhibit a wide variety of exceptional electronic and mechanical properties. In particular, single walled carbon nanotubes (SWCNTs) have been investigated with great attention in last ten years as strong PL emitters with good quantum yield.

SWCNTs can be thought as a graphene sheet that has been rolled up to form a seamless cylinder. A single walled carbon nanotube whose chiral vector has coordinates n, m is called an (n, m) nanotube. In Fig.6.1, according to the n, m numbers, nanotubes

7. OPTICAL PROPERTIES OF OTHER SAMPLES

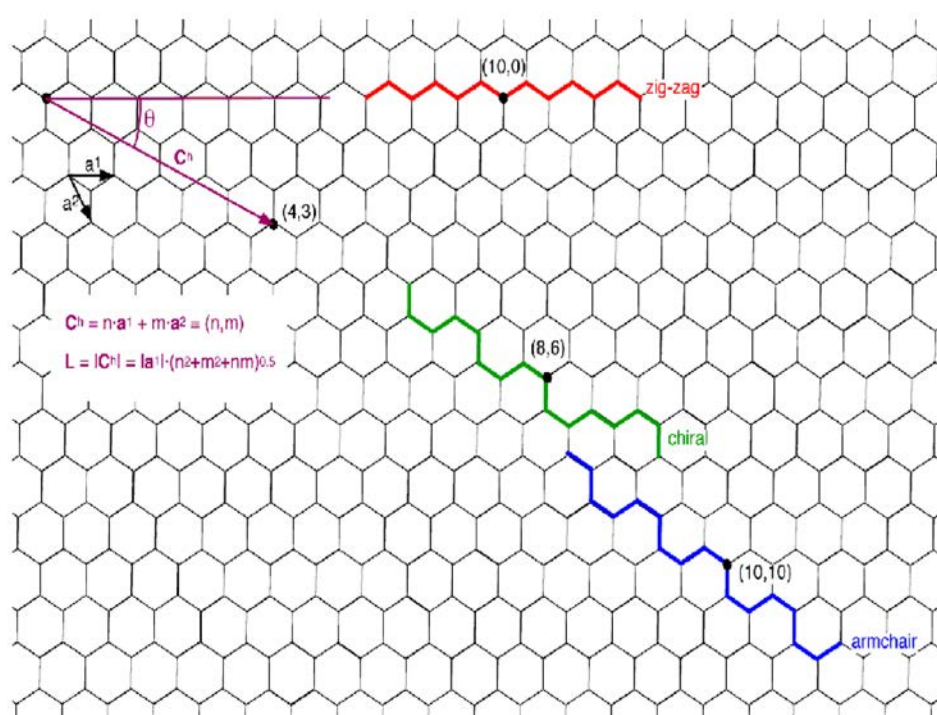


Figure 7.1: Nanotubes that can be formed by rolling up a graphene sheet with coordinates (n, m) showing the different kinds of tubes possible(172).

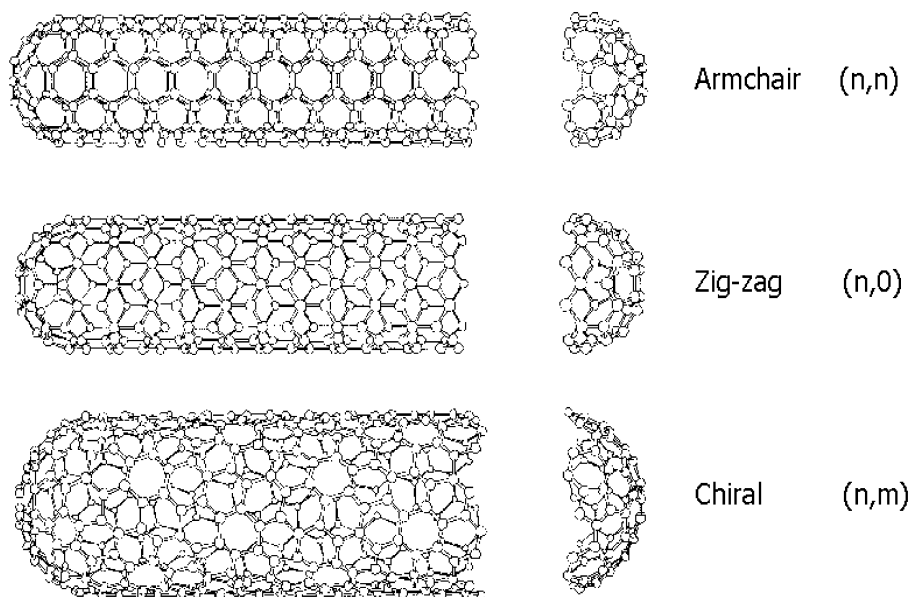


Figure 7.2: The whole family of nanotubes based on different (n, m) coordinates(172).

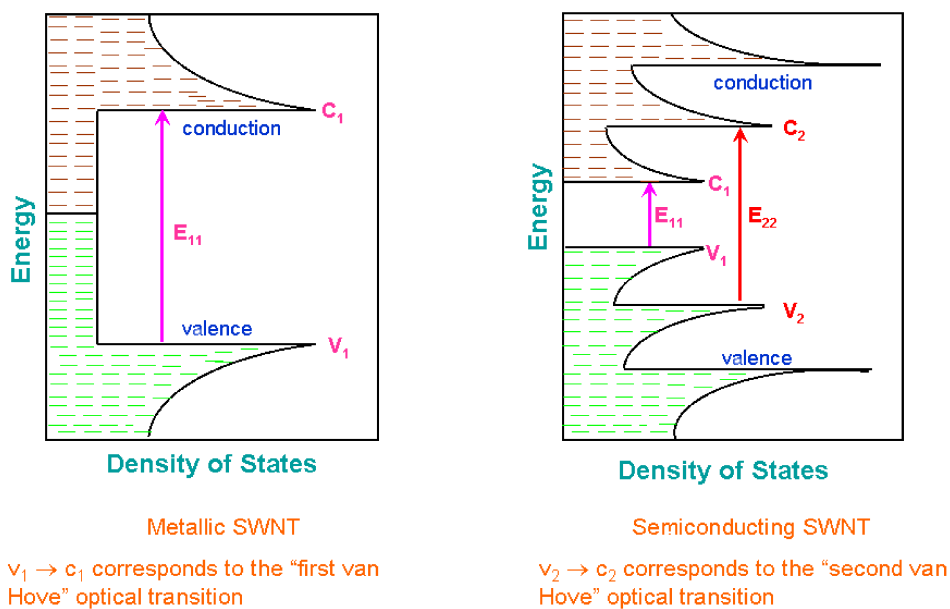


Figure 7.3: The density of states in metallic and semiconducting single walled carbon nanotubes with Van Hove singularities(174).

7. OPTICAL PROPERTIES OF OTHER SAMPLES

can be classified as armchair nanotubes when $n = m$, zigzag nanotubes with $(n, 0)$ and chiral nanotubes for all the other n, m combinations.

Basically, you can roll up the sheet along one of the symmetry axes: this gives either a zig-zag tube or an armchair tube. It is also possible to roll up the sheet in a direction that differs from a symmetry axis: you then obtain a chiral nanotube, in which the equivalent atoms of each unit cell are aligned on a spiral. Besides the chiral angle, the circumference of the cylinder can also be varied. In general, the whole family of nanotubes is classified as zigzag, armchair, and chiral tubes of different diameters in Fig.6.2.

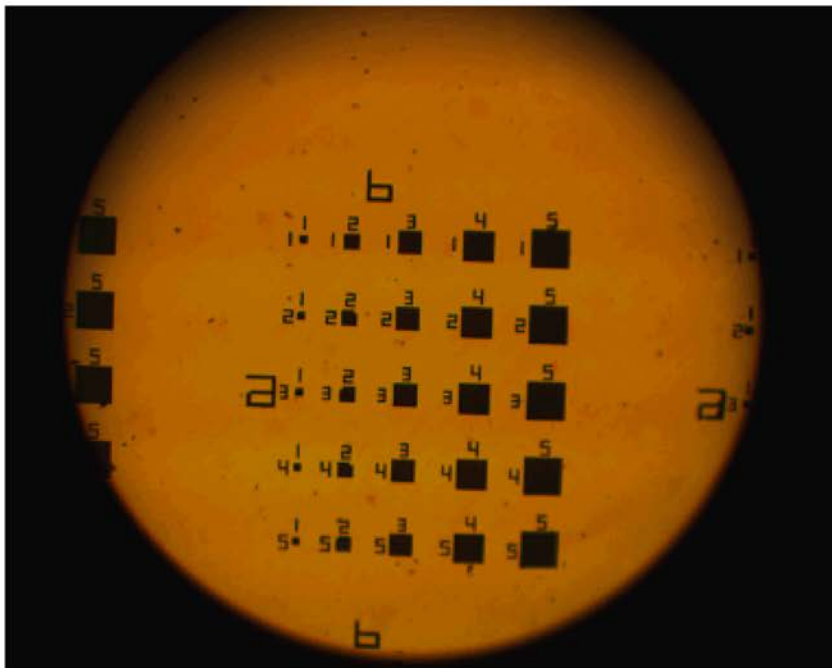
Also, the metallicity of a SWCNT can be determined from its diameter and chirality. When the ratio $n - m/3$ is an integer then the corresponding nanotube is metallic, otherwise it is semiconducting.

The electronic transitions within the one-dimensional density of states (DOS) determine the optical properties of carbon nanotubes. A typical feature of 1D structures is the discontinuous function of energy in their DOS. Because of the one dimensional nature of a carbon anotube, it has a series of van Hove singularities. Electronic transitions are possible between van Hove singularities which are labelled for transitions between C_i and V_j . Fig.6.3 shows density of states in metallic and semiconducting SWCNTs connecting with the valence and conduction energy bands. In a semiconducting material, with larger than band gap excitation energy, an electron in the i^{th} valence band can be excited to the j^{th} conduction band.

7.1.2 Micro-photoluminescence of SWCNTs

Most of previous investigated results on the optical properties of SWCNTs can be explained by classical optics. In this thesis, we try to measure micro-PL from a SWCNT with a sharp Lorentzian lineshape (0.76meV) (in Fig.6.6) and the spatial dispersion of a SWCNT is confirmed by atomic force microscopy (AFM). High density SWCNTs exhibits broad spectral peaks at room temperature. However, to measure single level micro PL, a dilute solution is deposited with a mean density below one nanotube per μm^2 . Then, to confirm the individual SWCNT location on the sample, we used a gold metal mask on the SWCNT sample surface to limit the number of nanotubes illuminated in Fig.6.4 (a). In Fig.6.4 (b), an AFM image was recorded to show the location of the SWCNT with PFO polymer coating to inhibit quenching of the PL near the hole

(a)



(b)

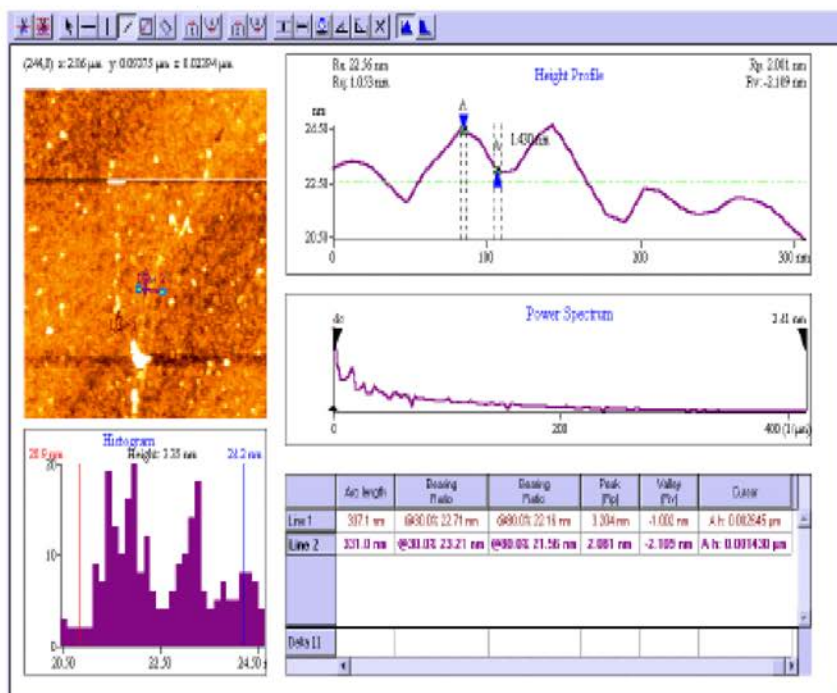


Figure 7.4: (a) Dilute single walled carbon nanotube-PFO polymers on a gold metal mask
 (b) AFM of dilute single walled carbon nanotube-PFO polymers on a gold metal mask

7. OPTICAL PROPERTIES OF OTHER SAMPLES

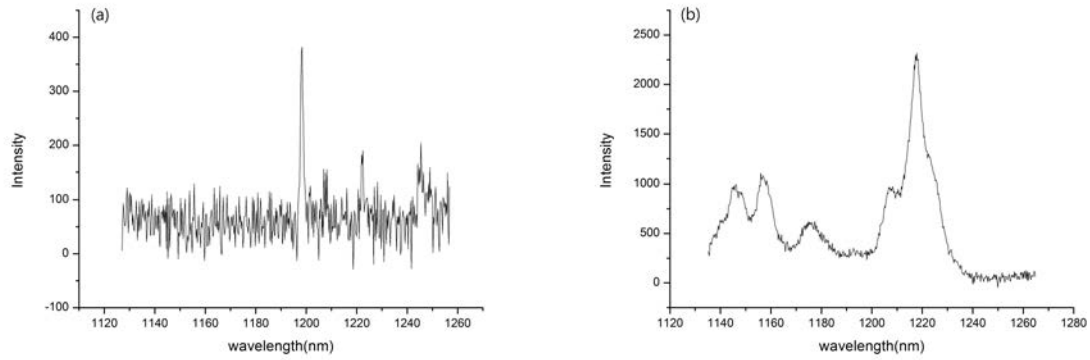


Figure 7.5: (a): Micro photoluminescence from a single carbon nanotube; (b) Micro photoluminescence from a bundle of carbon nanotubes

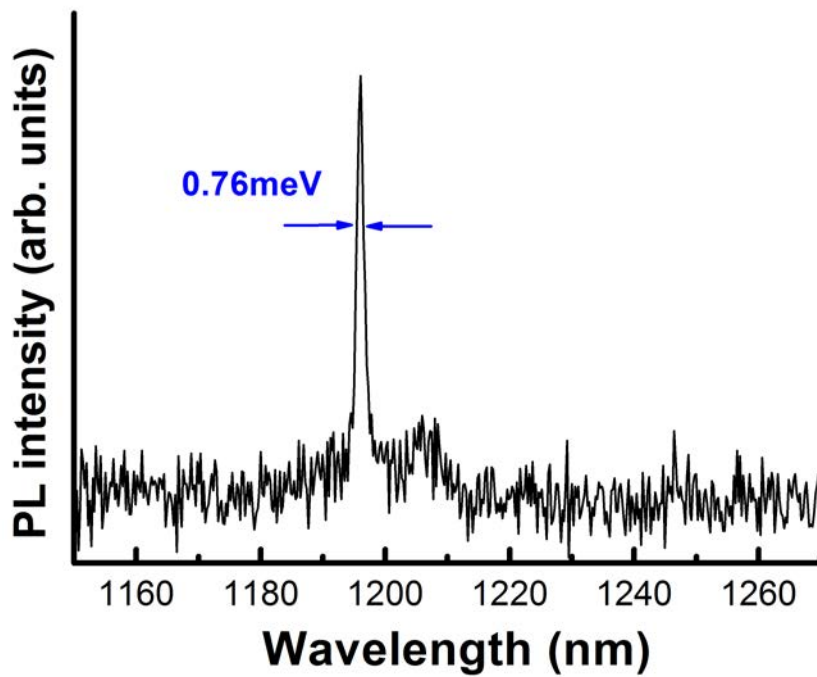


Figure 7.6: An ultranarrow PL from an individual CNT with FWHM of 0.76meV

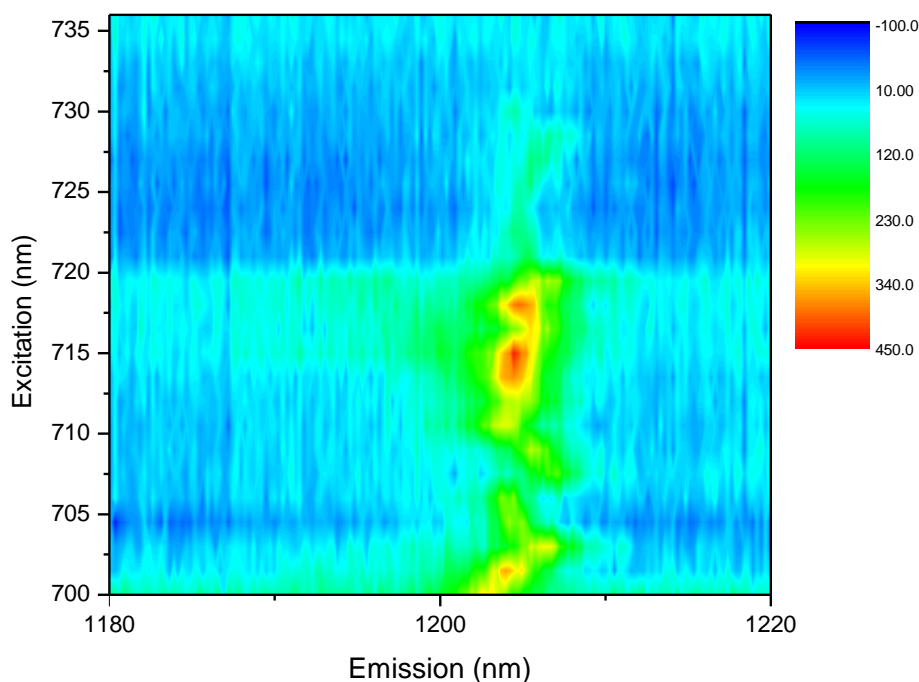


Figure 7.7: A photoluminescence excitation map from a single carbon nanotube

of the Au mask. The SWCNT is approximately $1.5 \mu\text{m}$ in length with a 3 nm diameter.

The term photoluminescence means that light is absorbed by a medium, generating an excited state, and then light with lower frequency is re-emitted to a ground state. The excitation used here was in the energy range of the E_{22} excitonic manifold while the PL was originated from the E_{11} exciton. In Fig.6.5 (a) and (b), micro PL signals of single carbon nanotubes and bundle carbon nanotubes are investigated. Narrow linewidths from single carbon nanotube are measured with a FWHM of $800 \mu\text{eV}$ as shown in Fig.6.5 (a).

7. OPTICAL PROPERTIES OF OTHER SAMPLES

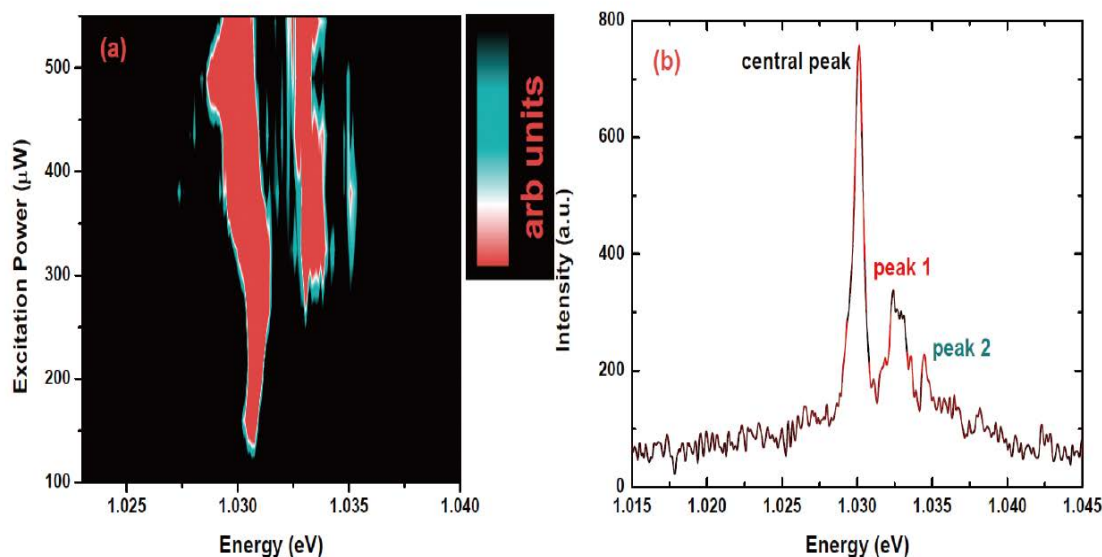


Figure 7.8: (a): Power dependent micro-PL (b) State filling effect from a single carbon nanotube

7.1.3 Photoluminescence excitation of SWCNTs

The energy band structure of a single carbon nanotube which is closely related to the optical absorption is investigated by photoluminescence excitation (PLE) spectroscopy. In PLE, the PL intensity is recorded while the excitation wavelength is changed. The maximum intensity is measured when the excitation energy passes through an absorption resonance from which relaxation to a PL emitting transition occurs. We can draw a three dimensional map which shows luminescent intensity vs emission and excitation wavelength. In Fig.6.7, a PL spectrum is recorded for every excitation energy with a 1.5 nm excitation step size. (Our PLE map is measured from 700nm to 735nm). The observed broad range of excitation energies with a narrow PL emission areas provides an understanding of exciton dynamics inside single carbon nanotube. An exciton can be excited into a number of excited states before the bound electron-hole pair relaxes to the E_{11} band edge and recombines. In the PLE map, along the excitation wavelength for the same band edge emission around 1200nm, intense PL peaks at several special excitation values were observed. The main E_{22} interband transition is around 715nm.

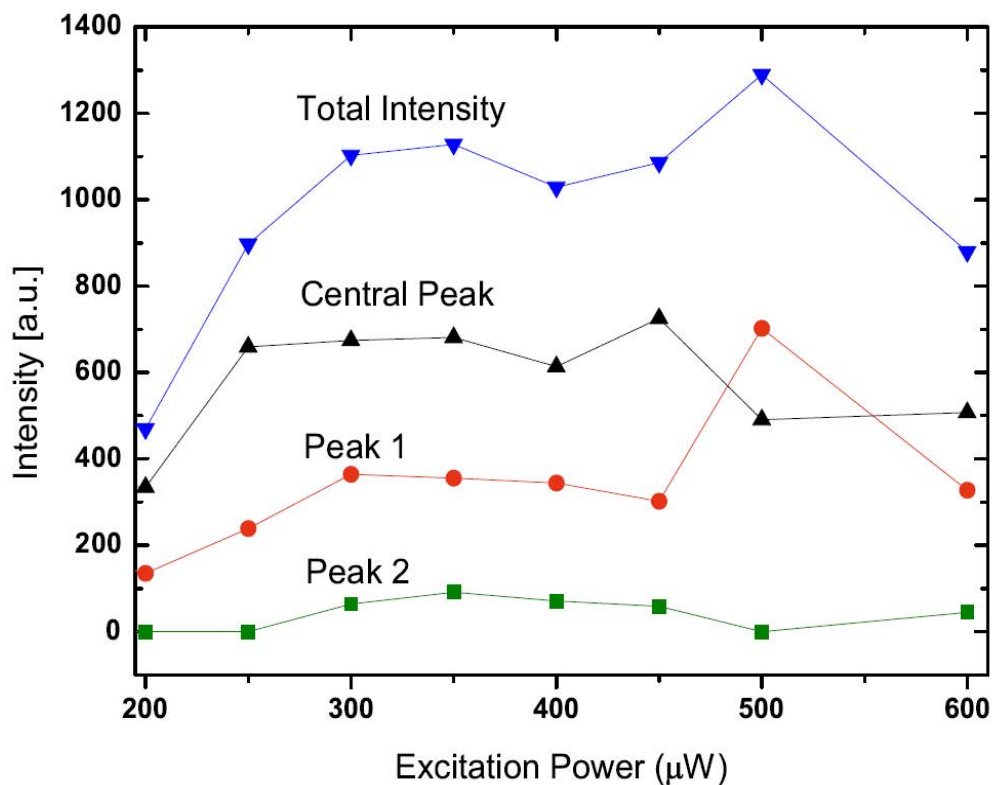


Figure 7.9: Power dependent micro-PL from 3 different peaks in Fig. (b)

In general, PLE spectroscopy is a very powerful and efficient tool for understanding the optical dynamics inside single carbon nanotubes.

7.1.4 Quantum dot confined in single-walled carbon nanotubes

Quantum dot-like states are investigated in small diameter nanotubes, resulting in spatial confinement of excitons along the nanotube axis (175, 176). The strong sharp spectral lines in photoluminescence spectra similar with typical photoluminescence of quantum dots are strong evidence for confinement states in CNTs in Fig.6.6. In confined discrete energy states such as QDs, state filling spectroscopy is a well known phenomenon. In CNTs, a possible exciton states perpendicular to the tube axis will be quantized because of the rolled up structure from graphene (177, 178).

7. OPTICAL PROPERTIES OF OTHER SAMPLES

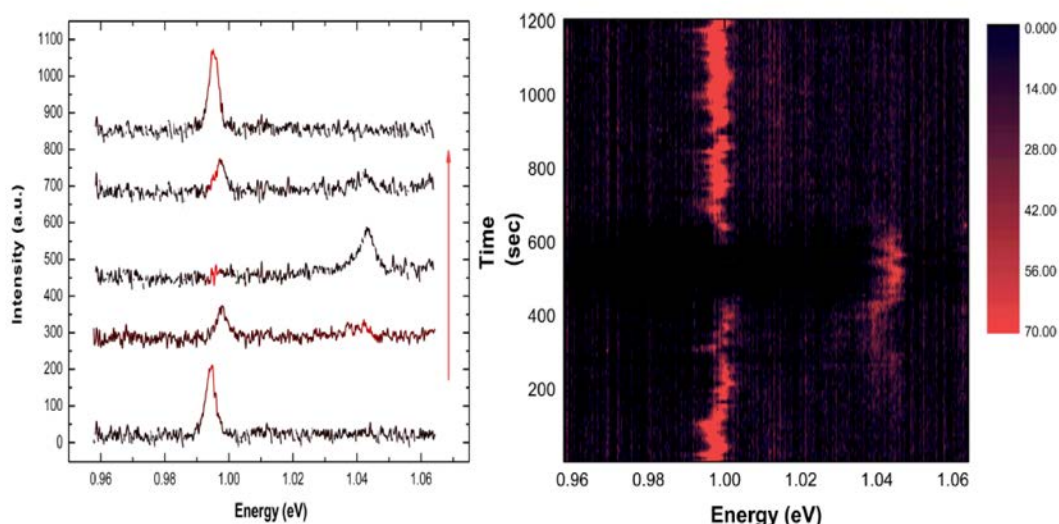


Figure 7.10: Temporal evolution of a single CNT. The figure on the left shows individual spectra taken from one on the right. The data were collected by focusing the laser beam on a single CNT and collect the emission at every 10s. The color changing in the right pane from black to red indicate increasing emission intensity.

Fig.6.8 shows micro-PL of individual CNTs which were excited at different power densities. In the low energy regime, only one sharp peak is observed. A new peak starts to appear when the excitation power density is increased. These emission features look similar to many self-assembled QDs. However, saturation and a red-shift appear at high excitation power densities which are also distinguishing features of three-dimensional confinement of carriers in QDs. Fig.6.9 shows FWHM times the peak intensity vs excitation laser power of each peak depicted in Fig.6.8 (a). The black, red, green and blue lines corresponded to the central peak, peak 1, peak 2 and the sum of the intensity of all 3 peaks in Fig.6.8 (b). Whenever the central peak intensity increases (decreases), peak 1 or 2 decreases (increases). There is a strong correlation between 3 different peaks by power densities change in Fig.6.9. This correlation strongly supports the assertion that these emission peaks arise from the same dot-like states. So, we can understand strong evidence of 3D confinement of carriers in a single carbon nanotube.

In Fig.6.10, five PL spectra from the same spot on a single CNT were taken from

7.2 Future work for a single CdSe nanocrystal

a temporal evolution series with 10s accumulation time at various intervals. Also, each spectrum is measured with 100 to 300 seconds time separation. Color changes in Fig.6.10 with time evolution indicate emission intensity change. These spectral transition can be understood as quantum dots-like regions confined in a single CNT. The exciton can be created in one QD-like state by the same laser excitation in a confocal experimental setup. If this created exciton can be transferred to a neighboring QD-like state, then a different high energy PL peak is seen as we observe in Fig.6.10. However, the mobilized excitons tend to be trapped in lower energetic levels hence the emission energy in the PL spectrum returns again to its original value with temporal evolution. Therefore, based on our measurements in Fig.6.8 ~ 10, QD like localization in a single carbon is strongly supported. Further magnetic field-dependent measurements on this system are underway at present.

7.2 Future work for a single CdSe nanocrystal

Colloidal semiconductor nanocrystals with high photoluminescence (PL) quantum efficiencies have been investigated for both fundamental research and diverse applications (179). Because the size of colloidal nanocrystals can be adjusted by wet chemical methods, the electronic properties can be changed significantly. The emission colour of CdSe nanocrystals can be tuned over almost the whole visible range depending on size variations. Based on these properties, colloidal semiconductor nanocrystals can be applied to potential applications in opto-electronics such as light-emitting diodes (LEDs), lasers, and bio-sensors (156, 180, 181, 182). In our group, we make CdSe and CdTe nano crystal quantum dots by a chemical technique.

To attach these CdSe/CdTe quantum dots (QDs) to a sapphire plate, we undertake additional chemical treatment. The polymer CAPO is layered on the substrate and attaches the CdSe quantum dots, and PMMA then anchors and protects them against ageing for low temperature experiments. To undertake these procedures we used a Layer-by-Layer (LBL) assembly method which is simple, versatile, and inexpensive and is illustrated in Fig.6.1. In general, the LBL process is achieved by alternately exposing a substrate to positively and negatively charged polymers or particles.

7. OPTICAL PROPERTIES OF OTHER SAMPLES

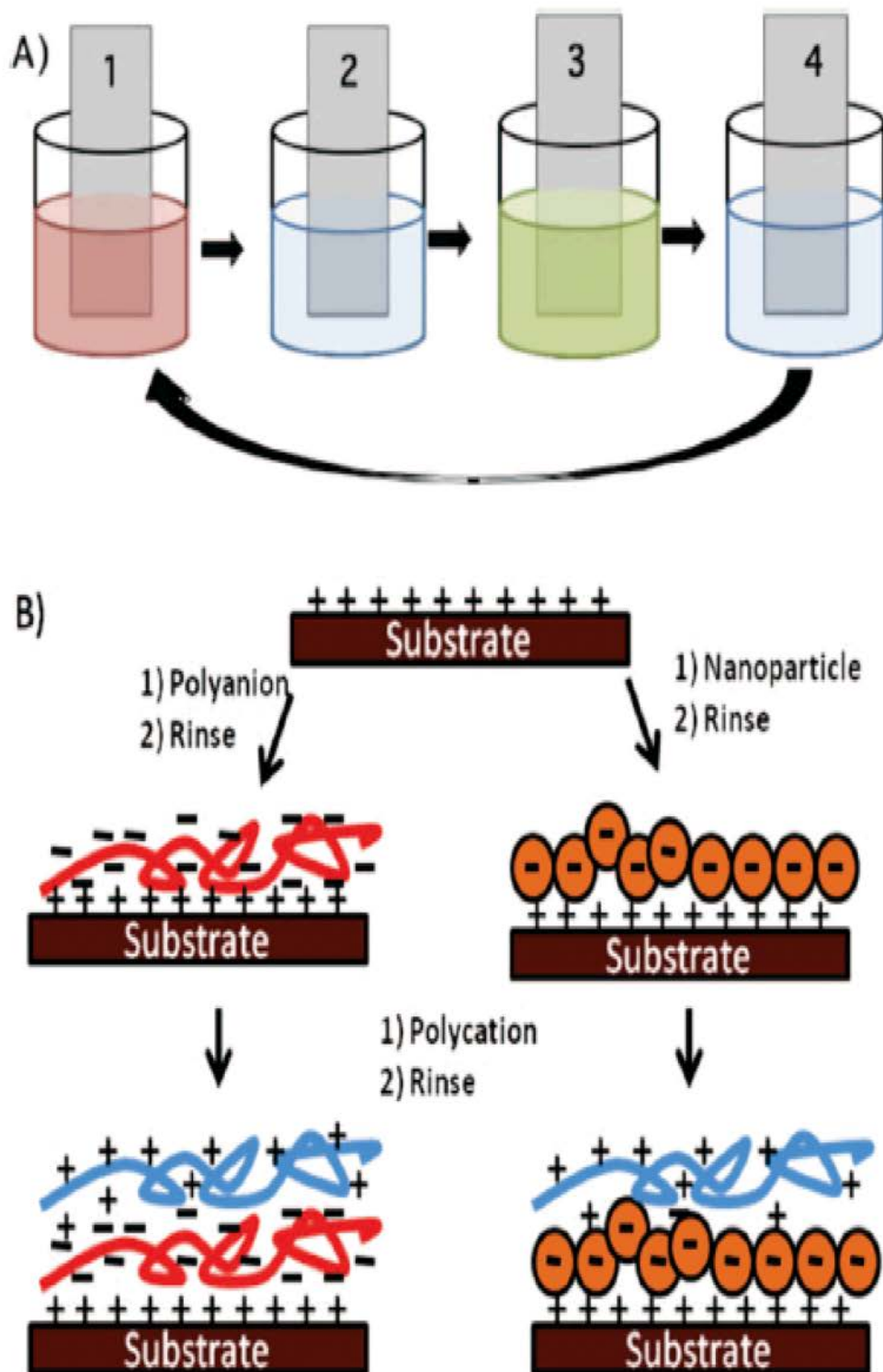


Figure 7.11: A): Scheme for LBL film-deposition. Steps 1 and 3 represent the adsorption of polyanion and polycation, step 2 and 4 are washing steps, B): Two adsorption routes, depicting LBL deposition for polymers and polymers with nanoparticles(183).

7.2.1 Theoretical background

Surface plasmons (SPs) were introduced in the surface science field due to the early work of Ritchie in the 1950s (184). SPs are waves which propagate along the surface of a metal and are light waves which are trapped on the surface due to their interaction with the free electrons of the conductor. In this interaction, the free electrons respond by oscillating in resonance with the light wave. This resonant interaction between the surface charge oscillation and the electromagnetic field of light is illustrated in Fig.6.2.

The main properties of these SPs are: the momentum of the SP mode ($\hbar k_{\text{SP}}$) is greater than that of a free space photon of the same frequency, $\hbar k_0$ ($k_0 = \omega/c$). Using the Maxwell's equations, we can get the SP dispersion relation.

$$k_{\text{PL,metal}} = k_0 \sqrt{\frac{e_{\text{d}} e_{\text{m}}}{e_{\text{d}} + e_{\text{m}}}}, \quad (7.1)$$

(e_{m} is the frequency-dependent permittivity of the metal, and e_{d} is frequency-dependent permittivity of the dielectric material). A SP will propagate but will gradually attenuate due to losses arising from absorption in the metal. This attenuation depends on the dielectric function of the metal at the SP frequency. The propagation length (δ_{SP}) can be calculated from the imaginary part of SP wavevector k_{SP} ($k_{\text{SP}} = k' + ik''$),

$$\delta_{\text{SP}} = \frac{1}{2} k''_{\text{SP}} = \frac{c}{\omega} \left(\frac{e'_{\text{m}} + e_{\text{d}}}{e'_{\text{m}} e_{\text{d}}} \right)^{3/2} \frac{(e'_{\text{m}})^2}{e''_{\text{m}}} \quad (7.2)$$

where e'_{m} and e''_{m} are the real and imaginary parts of the dielectric function of the metal ($e_{\text{m}} = e'_{\text{m}} + ie''_{\text{m}}$). The field perpendicular to the surface decays exponentially with distance from the surface. We call this perpendicular direction field evanescent or near field in nature and is a result of the bound, non-radiative nature of SPs, which prevents power from propagating away from the surface.

The PL intensity of CdSe nanocrystals depends on the absorption, radiative emission, and nonradiative energy dissipation rates in the CdSe nanocrystal QD-Au metal QD complexes. The PL intensity changes are mostly determined by two processes : (1) enhancement of the absorption and radiative emission due to the plasmon-induced

7. OPTICAL PROPERTIES OF OTHER SAMPLES

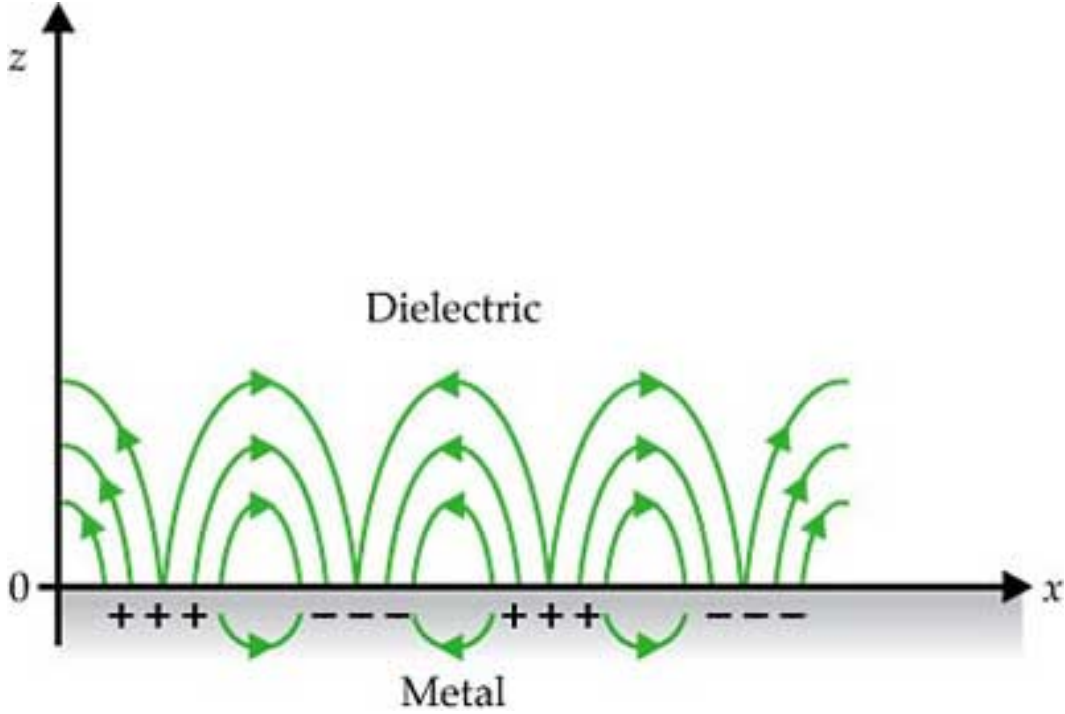


Figure 7.12: Propagating surface plasmon on the the sample boundary surface(185).

electric field, and (2) quenching of the excited nanocrystal state due to energy transfer to the metal surface. The PL intensity is measured by equation (6.3)

$$I_{\text{PL,metal}} = \frac{P\gamma_{\text{rad}}I_{\text{abs}}}{\gamma_{\text{metal}}}, \quad (7.3)$$

I_{abs} is the intensity of light absorption and P is the electromagnetic enhancement factor of absorption and radiative emission on the Au QD. The enhancement parameter P is mainly determined by plasmon-induced absorption enhancement rather than radiative emission enhancement.

$$1/\tau_{\text{PL,metal}} = \gamma_{\text{rad}} + \gamma_{\text{nonrad}} + \gamma_{\text{metal}}, \quad (7.4)$$

The PL lifetime is changed by the radiative and nonradiative recombination rates and nonradiative energy transfer rate from nanocrystals to metal and is given by equation (6.4). The PL lifetime on the sapphire is given by $1/\tau_{\text{PL}} = \gamma_{\text{rad}} + \gamma_{\text{nonrad}}$. On

7.2 Future work for a single CdSe nanocrystal

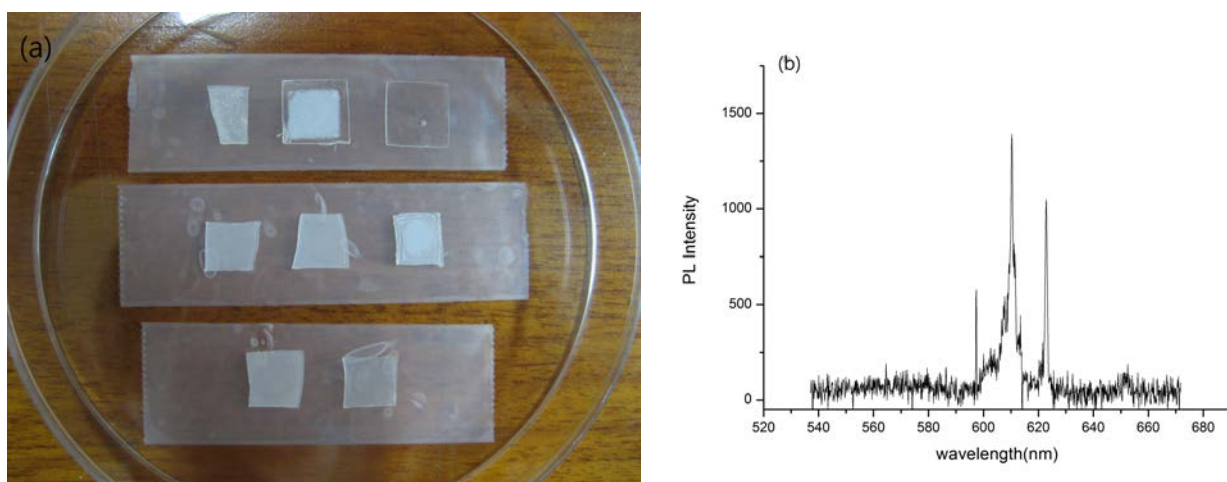


Figure 7.13: (a): Our prepared CdSe QD samples on sapphire plates (b): micro-PL spectrum of a single CdSe QD on a sapphire plate

the Au QD, enormous changes in the PL lifetime are expected, and the energy transfer rate from the CdSe nanocrystals to the Au QDs is much larger than the radiative and nonradiative recombination rate of CdSe nanocrystals alone. The PL lifetime of the CdSe nanocrystal QD-Au QD complex is determined by the nonradiative energy transfer rate from CdSe nanocrystals to the Au metal.

7.2.2 Single QD micro photoluminescence on a sapphire plate

Surface plasmons (SPs) offers the unique ability to localize and enhance electromagnetic fields and have been applied to various optical devices. The SP coupling technique is one of the most effective methods of increasing emission efficiency.

Fig.6.3 shows some CdSe QDs attached to sapphire plates. I measured the micro photoluminescence (micro-PL) signal from a single quantum dot on this sapphire plate with an exposure time of 60 seconds, and a very low excitation power of $5 \mu\text{W}$. To get a single QD PL signal, I needed a long accumulation time with low excitation power. I used this single PL signal as a reference to compare with enhanced PL signals from CdSe QDs coupled to Au nanoparticles. The main purpose of this project was the observation of local-surface plasmon enhancement of the PL emission (185, 186). When metallic nanoparticles (silver, gold, aluminium) are placed near the CdSe semiconduc-

7. OPTICAL PROPERTIES OF OTHER SAMPLES

tor nanoparticles, the local surface plasmon field on the metallic surface affects the CdSe semiconductor nanoparticle emission. Currently, in ensemble systems, a significant PL enhancement of the CdSe and CdTe PL emission has been observed due to local surface plasmon of gold or silver nanoparticles (187).

In our group, we are able to adjust the distance between CdSe and Au by using non-conducting bio-materials (such as SA (streptoavidine) and DB(D-biotin)). Theoretically, the coupling between a semiconductor nanoparticle and a metallic nanoparticle will not only enhance the emission efficiency but also change the energy states. I wanted to observe such energetic changes due to the coupling more quantitatively at the single QD level by adjusting the distance between the QDs and the metallic nanoparticles in a systematic way.

Excitons and plasmons are typical excited states of nanostructure components. I will investigate photoluminescence (PL) enhancement due to the interaction between localized surface plasmon in Au QD and exciton generated in CdSe/ZnS core-shell semiconductor nanocrystal quantum dot. This enhancement result will be compared with previous measured single PL intensity from CdSe QD on the sapphire plate. Also, PL quenching due to energy transfer to the Au QD surface is expected theoretically. Because of this quenching process, the PL lifetime in CdSe QD-Au QD hybrid samples will be shortened significantly compared with CdSe QDs on a bare sapphire plate.

8

Summary of the thesis and future work

The optical properties of GaAs quantum rings have been presented by time-integrated and time-resolved micro-photoluminescence methods. These methods are strong tools for investigating e-h pair dynamics in a single QR.

The presence of an asymmetric localized state in a single GaAs QR was investigated by using the adiabatic potential. To get the adiabatic potential, the vertical part of the Schrödinger equation was solved, where the vertical confinement was represented by the vertical quantum number k . To confirm this theoretical estimation, polarisation-resolved spectroscopy was investigated for ground/excited state exciton and biexciton state (188, 189). The strong polarization dependence of the ground state exciton (N=1) ($\sim 0.8\text{meV}$), excited state exciton (N=2) ($\sim 1.35\text{meV}$) and biexciton ($\sim 1.75\text{meV}$) strongly support the existence of an asymmetric localized state in a single QR. In order to analyse the relation between ground/excited state excitons and biexcitons in these localised states in a single quantum ring, the dependence on excitation power, temperature, polarization asymmetry, and time-resolved photoluminescence have been investigated. Both the excited exciton state and the biexciton state show a large polarization asymmetry, a broad linewidth, and a strong optical phonon-interaction when compared to the ground state exciton because of selection rule changes and a large polarity induced by the asymmetry arising from a local crescent-like structure in the QR. We also found that saturation of the ground state exciton is dominated by a fast dissociation of the biexciton state and slow intra-relaxation of the excited state exci-

8. SUMMARY OF THE THESIS AND FUTURE WORK

ton. Finally, polarization splittings were presented for the various exciton confinement energies. These results showed how localization states were changed by the exciton confinement energies and the presence of strong localization of the exciton state over 1.8eV of exciton confinement energy.

Based on our understanding of the localized states for an asymmetric QR structure, the optical Aharonov-Bohm effect (AB effect) will be investigated under high magnetic fields (190, 191, 192, 193, 194). In the case of a type-2 quantum dot, the rotating charge in the shell (either electron or hole) with respect to the remaining charge in the core determines the AB oscillation period. On the other hand, the different orbital radius of a weakly-bound electron-hole pair is a prerequisite for the optical AB effect as the coupling to the magnetic flux is opposite for the electron and hole. Nevertheless, the individual motion of the e-h pair is not clear; either the hole radius is larger than the electron or vice versa. An ideal isotropic ring shape was often assumed, but the presence of the anisotropic rim height and elliptical shape asymmetry has been overlooked. Concerned with the complicated QR morphology, the so-called volcano-like QR model can be used (17, 195). In this case, the wavefunction delocalization is obtained by tunnelling as the extended state of weak localization, and the holes are likely to be vulnerable to localization due to the heavy mass.

Because of the presence of the height anisotropy and asymmetry, the orbital angular moment competes with the asymmetric exchange interaction and the potential barrier along the azimuthal angle of a ring rim. Therefore, the AB effect will become evident when the Zeeman splitting exceeds the anisotropic and asymmetric energy (196, 197, 198). Also, the diamagnetic shift of neutral excitons is inseparable under low magnetic fields. Therefore, an external magnetic field must be large enough to overcome the anisotropy-induced potential barrier or asymmetric exchange interaction to observe clear AB effect signals. Work on this is in progress, but will not be completed in time for inclusion in this thesis.

References

- [1] Y.Aharonov et.al. Significance of Electromagnetic Potentials in the Quantum Theory. *Phys. Rev.*, 115:485, 1959. 1
- [2] M.Bayer et.al. Optical Detection of the Aharonov-Bohm Effect on a Charged Particle in a Nanoscale Quantum Ring. *Phys.Rev.Lett.*, 90:186801, 2003. 1
- [3] A. O. Govorov et.al. Polarized excitons in nanorings and the optical Aharonov-Bohm effect. *Phys.Rev.B*, 66:081309, 2002. 1, 82, 83
- [4] R. A. Romer et.al. Aharonov-Bohm effect for an exciton. *Phys.Rev.B*, 62:7045, 2000. 1
- [5] Hui Hu et.al. Aharonov-Bohm effect of excitons in nanorings. *Phys.Rev.B*, 63:195307, 2001. 1
- [6] N. H. Bonadeo et.al. Coherent Optical Control of the Quantum State of a Single Quantum Dot. *Science*, 282:1473, 1998. 1
- [7] M. Bayer et.al. Coupling and Entangling of Quantum States in Quantum Dot Molecules. *Science*, 291:5503, 2001. 1
- [8] M. Bayer et.al. Electron-Hole Transitions between States with Nonzero Angular Momenta in the Magnetoluminescence of Quantum Dots. *Phys.Rev.Lett.*, 74:3439, 1995. 1
- [9] A. I. Filin et.al. Effect of nanocrystal growth conditions on exciton decay and spin dephasing in an ensemble of CdSe nanocrystals grown in glass. *Phys.Rev.B*, 73:125322, 2006. 1

REFERENCES

- [10] Igor Zutic et.al. Spintronics: Fundamentals and applications. *Rev. Mod. Phys.*, 76:323, 2004. 1
- [11] T. Mano et.al. Self-assembly of quantum dots and rings by droplet epitaxy and their optical properties. *J. Nanophoton.*, 3:031605, 2009. 2, 4
- [12] J.Kim et al. Different shape of GaAs quantum structures under various growth conditions. *Thin Solids Films*, 518:6500, 2010. 2, 5, 20
- [13] S. Sanguinetti et.al. Electron-phonon interaction in individual strain-free GaAs/Al_{0.3}Ga_{0.7}As quantum dots. *Phys.Rev.B*, 73:125342, 2006. 1
- [14] R. C. Miller et.al. Excitons in GaAs quantum wells. *J. Lumin.*, 30:520, 1985. 1
- [15] V. M. Fomin et.al. *Theory of electron energy spectrum and Aharonov-Bohm effect in self-assembled In_xGa_{1-x}As quantum rings in GaAs*, volume 76. 2007. 1, 39
- [16] Ta-Chun Lin et.al. Impacts of structural asymmetry on the magnetic response of excitons and biexcitons in single self-assembled In(Ga)As quantum rings. *Phys.Rev.B*, 80:081304, 2009. 1, 50
- [17] N.A.J.M. Kleemans et.al. Oscillatory Persistent Currents in Self-Assembled Quantum Rings. *Phys. Rev. Lett.*, 99:146808, 2007. 1, 37, 41, 46, 57, 84, 104
- [18] H. D. Kim et.al. Asymmetry of localised states in a single quantum ring: Polarization dependence of excitons and biexcitons. *Appl. Phys. Lett.*, 102:033112, 2013. 1, 37, 57, 61, 63, 72, 75, 79
- [19] P. Foldi et.al. Spintronic single-qubit gate based on a quantum ring with spin-orbit interaction. *Phys.Rev.B*, 71:033309, 2005. 1
- [20] T. Guenther et.al. Coherent Nonlinear Optical Response of Single Quantum Dots Studied by Ultrafast Near-Field Spectroscopy. *Phys.Rev.L*, 89:057401, 2002. 1
- [21] N. Byers. Theoretical Considerations Concerning Quantized Magnetic Flux in Superconducting Cylinders. *Phys. Rev.Lett.*, 7:46, 1961. 1
- [22] F.Bloch. Josephson Effect in a Superconducting Ring. *Phys. Rev.B*, 2:109, 1970. 1

-
- [23] M. Buttiker et.al. Josephson behavior in small normal one-dimensional rings. *Phys. Lett. A*, 96:365, 1983. 1
- [24] S. Bednarek et.al. Spin Rotations Induced by an Electron Running in Closed Trajectories in Gated Semiconductor Nanodevices. *Phys.Rev.Lett.*, 101:216805, 2008. 3
- [25] J. I. Climente et.al. Magneto-optical transitions in nanoscopic rings. *Phys.Rev.B*, 68:075307, 2003. 3
- [26] J. I. Climente et.al. Magnetization of nanoscopic quantum rings and dots. *Phys.Rev.B*, 70:081301, 2004. 3
- [27] T. Kuroda et.al. Optical transitions in quantum ring complexes. *Phys.Rev.B*, 72:205301, 2005. 3, 4, 37, 39, 46, 57, 58, 59, 60, 72
- [28] R.J. Warburton et.al. Giant permanent dipole moments of excitons in semiconductor nanostructures. *Phys.Rev.B*, 65:113303, 2002. 3, 17
- [29] Benito Alen et.al. Continuum and discrete excitation spectrum of single quantum rings. *Phys.Rev.B*, 72:155331, 2005. 3, 17
- [30] W. H. Kuan et.al. Energy levels of a parabolically confined quantum dot in the presence of spin-orbit interaction. *J. Appl. Phys.*, 95:6368, 2004. 3
- [31] V. D. Kulakovskii et.al. Fine Structure of Biexciton Emission in Symmetric and Asymmetric CdSe/ZnSe Single Quantum Dots. *Phys.Rev.Lett.*, 82:1780, 1999. 3
- [32] U. Aeberhard et.al. Effect of spin-orbit coupling on zero-conductance resonances in asymmetrically coupled one-dimensional rings. *Phys.Rev.B*, 72:075328, 2005. 3
- [33] E. Ribeiro et.al. Aharonov-Bohm Signature for Neutral Polarized Excitons in Type-II Quantum Dot Ensembles. *Phys.Rev.Lett.*, 92:126402, 2004. 3
- [34] T. Mano et.al. Nanometer-scale GaAs ring structure grown by droplet epitaxy. *J. Cryst. Growth*, 278:108, 2005. 3, 72

REFERENCES

- [35] T. Mano et.al. Self-Assembly of Concentric Quantum Double Rings. *Nano Lett.*, 5:425, 2005. 3
- [36] K. Watanabe. Fabrication of GaAs Quantum Dots by Modified Droplet Epitaxy. *Jpn. J. Appl. Phys.*, 39:79, 2000. 3
- [37] J. M. Garcia et.al. Intermixing and shape changes during the formation of InAs self-assembled quantum dots. *Appl. Phys. Lett.*, 71:2014, 1997. 4
- [38] Daniel Granados et.al. In(Ga)As self-assembled quantum ring formation by molecular beam epitaxy. *Appl. Phys. Lett.*, 82:2401, 2003. 4
- [39] R. J. Warburton et.al. Optical emission from a charge-tunable quantum ring. *Nature*, 405:926, 2000. 4
- [40] A. Kuther et.al. Zeeman splitting of excitons and biexcitons in single In_{0.60}Ga_{0.40}As/GaAs self-assembled quantum dots. *Phys.Rev.B*, 58:7508, 1998. 4
- [41] R. Leon et.al. Spatially Resolved Visible Luminescence of Self-Assembled Semiconductor Quantum Dots. *Science*, 267:1966, 1995. 4
- [42] T. E. Schlesinger et.al. Determination of the interdiffusion of Al and Ga in undoped (Al,Ga)As/GaAs quantum wells. *Appl. Phys. Lett.*, 49:519, 1986. 4
- [43] S. Sanguinetti et.al. Effects of post-growth annealing on the optical properties of self-assembled GaAs/AlGaAs quantum dots. *J. Cryst. Growth*, 242:321, 2002. 4
- [44] K. Leosson et.al. Homogeneous linewidth of self-assembled IIIV quantum dots observed in single-dot photoluminescence. *Physica E*, 17:1, 2003. 4
- [45] V. Mantovani et.al. Low density GaAs/AlGaAs quantum dots grown by modified droplet epitaxy. *J. Appl. Phys.*, 96:4416, 2004. 4
- [46] J. R. Guest et.al. Measurement of optical absorption by a single quantum dot exciton. *Phys.Rev.B*, 65:241310, 2002. 4
- [47] Mark Fox. *Optical Properties of Solids*. Oxford University Press, 2001. 7, 8, 10, 11, 12, 13

-
- [48] E. Ribeiro et.al. Aharonov-Bohm Signature for Neutral Polarized Excitons in Type-II Quantum Dot Ensembles. *Phys.Rev.Lett.*, 92:126402, 2004. 17, 81
- [49] A. Madhukar et.al. Nature of strained InAs three-dimensional island formation and distribution on GaAs(100). *Appl. Phys. Lett.*, 64:2727, 1994. 17
- [50] G. S. Solomon et.al. Substrate temperature and monolayer coverage effects on epitaxial ordering of InAs and InGaAs islands on GaAs. *Appl. Phys. Lett.*, 66:991, 1995. 17
- [51] K. Watanabe. Photoluminescence studies of GaAs quantum dots grown by droplet epitaxy. *J. Cryst. Growth*, 227:1073, 2001. 17
- [52] N. Koguchi et.al. New MBE growth method for InSb quantum well boxes. *J. Cryst. Growth*, 111:688, 1991. 17
- [53] L. P. Levy et.al. Magnetization of mesoscopic copper rings: Evidence for persistent currents. *Phys.Rev.Lett.*, 64:2074, 1990. 20
- [54] V. Chandrasekhar et.al. Magnetic response of a single, isolated gold loop. *Phys. Rev. Lett.*, 67:3578, 1991. 20
- [55] A. Lorke et.al. Spectroscopy of Nanoscopic Semiconductor Rings. *Phys.Rev.Lett.*, 84:2223, 2000. 20, 39
- [56] Hong-Shi Ling et.al. Evolution of self-assembled InAs quantum ring formation. *J. Appl. Phys.*, 102:024314, 2007. 20
- [57] Lorenzo Pavesi et.al. Photoluminescence of Al_xGa_{1-x}As alloys. *J. Appl. Phys.*, 75:4779, 1994. 20
- [58] D. Mailly et.al. Experimental observation of persistent currents in GaAs-AlGaAs single loop. *Phys. Rev. Lett.*, 70:2020, 1993. 26
- [59] T. Raz et.al. Formation of InAs self-assembled quantum rings on InP. *Appl. Phys. Lett.*, 82:1706, 2003. 26
- [60] Q. Sun. Persistent Spin Current in a Mesoscopic Hybrid Ring with Spin-Orbit Coupling. *Phys.Rev.Lett.*, 98:196801, 2007. 26

REFERENCES

- [61] T. Chwiej et.al. Few-electron artificial molecules formed by laterally coupled quantum rings. *Phys.Rev.B*, 78:245306, 2008. 26
- [62] K.H.Lee. *Fabrication, Spectroscopy and Modelling of 3-5 nanostructures for Photonics*. PhD thesis, University of Oxford, 2006. 29, 30
- [63] D.P.Collins. *Optical Studies of Wide Bandgap Semiconductor Nanostructures*. PhD thesis, University of Oxford, 2010. 31, 33
- [64] Instruction of Hamamatsu PMT. 32, 33, 35
- [65] P. Michler et.al. A Quantum Dot Single-Photon Turnstile Device. *Science*, 290:2282, 2000. 36
- [66] A. J. Shields et.al. Detection of single photons using a field-effect transistor gated by a layer of quantum dots. *Appl. Phys. Lett.*, 76:3673, 2000. 36
- [67] M. Pelton et.al. Efficient Source of Single Photons: A Single Quantum Dot in a Micropost Microcavity. *Phys.Rev.Lett.*, 89:233602, 2002. 36
- [68] M. Furis et.al. Bright-exciton fine structure and anisotropic exchange in CdSe nanocrystal quantum dots. *Phys.Rev.B*, 73:241313, 2006. 37
- [69] M. V. Berry. Quantal Phase Factors Accompanying Adiabatic Changes. *Proc. R. Soc. London*, A392:45, 1984. 37
- [70] P. Lucignano et.al. Rashba control for the spin excitation of a fully spin-polarized vertical quantum dot. *Phys.Rev.B*, 71:121310, 2005. 37
- [71] O. Heller et.al. Biexcitons bound to single-island interface defects. *Phys.Rev.B*, 56:4702, 1997. 37
- [72] D. A. Kleinman. Binding energy of biexcitons and bound excitons in quantum wells. *Phys.Rev.B*, 28:871, 1983. 37
- [73] K. Brunner et.al. Sharp-Line Photoluminescence and Two-Photon Absorption of Zero-Dimensional Biexcitons in a GaAs/AlGaAs Structure. *Phys.Rev.Lett.*, 73:1138, 1994. 37

-
- [74] J. A. Barker et.al. Electron and hole wave functions in self-assembled quantum rings. *Phys.Rev.B*, 69:035327, 2004. 39
- [75] S. Viefers et.al. Quantum rings for beginners: energy spectra and persistent currents. *Physi*, 21:1, 2004. 39
- [76] Jakyoungh Song et.al. Magnetic field effects on quantum ring excitons. *Phys.Rev.B*, 63:125302, 2001. 39
- [77] A. Fuhrer et.al. Energy spectra of quantum rings. *Nature*, 413:822, 2001. 39
- [78] M. Yamagiwa et.al. Confined electronic structure in GaAs quantum dots. *J. Lumin.*, 108:379, 2004. 39
- [79] T. Chakraborty et.al. Optical Signatures of Spin-Orbit Interaction Effects in a Parabolic Quantum Dot. *Phys.Rev.Lett.*, 95:136603, 2005. 39
- [80] J. D. Koralek et.al. Emergence of the persistent spin helix in semiconductor quantum wells. *Nature*, 458:610, 2009. 39
- [81] S. V. Goupalov. Anisotropy-induced exchange splitting of exciton radiative doublet in CdSe nanocrystals. *Phys.Rev.B*, 74:113305, 2006. 39
- [82] J. Hours et.al. Single photon emission from individual GaAs quantum dots. *Appl. Phys. Lett.*, 82:2206, 2003. 39
- [83] D. Gammon et.al. Homogeneous Linewidths in the Optical Spectrum of a Single Gallium Arsenide Quantum Dot. *Science*, 273:87, 1996. 39
- [84] P. Offermans et.al. Atomic-scale structure of self-assembled In(Ga)As quantum rings in GaAs. *Appl. Phys. Lett.*, 87:131902, 2005. 39
- [85] P. Offermans et.al. Atomic-scale structure and formation of self-assembled In(Ga)As quantum rings. *Physica E (Amsterdam)*, 32:41, 2006. 39
- [86] J. A. Barker et.al. Theoretical analysis of electron-hole alignment in InAs-GaAs quantum dots. *Phys. Rev. B*, 61:13840, 2000. 39
- [87] J. Y. Marzin et.al. Calculation of the energy levels in InAs/GaAs source quantum dots. *Solid State Commun.*, 92:437, 1994. 40

REFERENCES

- [88] M. Califano et.al. Presentation and experimental validation of a single-band, constant potential model for self-assembled InAs/GaAs quantum dots. *Phys.Rev.B*, 61:10959, 2000. 40
- [89] O. Stier et.al. Electronic and optical properties of strained quantum dots modeled by 8-band k-p theory. *Phys.Rev.B*, 59:5688, 1999. 40
- [90] M. Grundmann et.al. InAs/GaAs pyramidal quantum dots: Strain distribution, optical phonons, and electronic structure. *Phys. Rev. B*, 52:11969, 1995. 42
- [91] Chris G. Van de Walle. Band lineups and deformation potentials in the model-solid theory. *Phys.Rev.B*, 39:1871, 1989. 42
- [92] C. E. Pryor et.al. Band-edge diagrams for strained III/V semiconductor quantum wells, wires, and dots. *Phys.Rev.B*, 72:205311, 2005. 43
- [93] Gabriel Bester et.al. Effects of linear and nonlinear piezoelectricity on the electronic properties of InAs/FGaAs quantum dots. *Phys.Rev.B*, 74:081305, 2006. 42
- [94] V. Fock. Bemerkung zur Quantelung des harmonischen Oszillators im Magnetfeld. *Z. Phys.*, 47:446, 1928. 42
- [95] C. G. Darwin. The Diamagnetism of the Free Electron. *Proc. Cambridge Philos. Soc.*, 27:86, 1930. 42
- [96] R. B. Dingle. Some Magnetic Properties of Metals. I. General Introduction, and Properties of Large Systems of Electrons. *Proc. R. Soc. London. Ser. A*, 211:500, 1952. 42
- [97] P. Hawrilyak L. Jacak and A. Wojs. *Quantum Dots*. Springer, Berlin, 1998. 42
- [98] M. Grundmann D. Bimberg and N. N. Ledentsov. *Quantum Dot Heterostructures*. Wiley, Chichester, 1999. 42
- [99] T. Chakraborty. *Quantum Dots: A Survey of the Properties of Artificial Atoms*. Elsevier, Amsterdam, 1999. 42

-
- [100] Paillard et.al. Spin Relaxation Quenching in Semiconductor Quantum Dots. *Phys.Rev.Lett.*, 86:1634, 2001. 42
- [101] A. J. Steinfort et.al. Strain in Nanoscale Germanium Hut Clusters on Si(001) Studied by X-Ray Diffraction. *Phys.Rev.Lett.*, 77:2009, 1996. 46
- [102] I. Kegel et.al. Interdependence of strain and shape in self-assembled coherent InAs islands on GaAs. *Europhys. Lett.*, 45:222, 1999. 46
- [103] H. Lipsanen et.al. Luminescence from excited states in strain-induced $\text{In}_x\text{Ga}_{1-x}\text{As}$ quantum dots. *Phys.Rev.B*, 51:13868, 1995. 46
- [104] K. Nishibayashi et.al. Luminescence quantum beats of strain-induced GaAs quantum dots. *Phys.Rev.B*, 68:035333, 2003. 46
- [105] P. W. Fry et.al. Inverted Electron-Hole Alignment in InAs-GaAs Self-Assembled Quantum Dots. *Phys.Rev.Lett.*, 84:733, 2000. 47
- [106] G. D. Sanders et.al. Effect of band hybridization on exciton states in $\text{GaAs-Al}_x\text{Ga}_{1-x}\text{As}$ quantum wells. *Phys.Rev.B*, 32:5517, 1985. 47
- [107] M. Furis et.al. Time- and Polarization-Resolved Optical Spectroscopy of Colloidal CdSe Nanocrystal Quantum Dots in High Magnetic Fields. *J. Phys. Chem. B*, 109:15332, 2005. 47
- [108] S. A. Empedocles et.al. Three-dimensional orientation measurements of symmetric single chromophores using polarization microscopy. *Nature*, 399:126, 1999. 47, 61, 72
- [109] S. Saikin et.al. Semiclassical Monte Carlo model for in-plane transport of spin-polarized electrons in III-V heterostructures. *J. Appl. Phys.*, 94:1769, 2003. 47
- [110] U. Woggon et.al. Huge binding energy of localized biexcitons in CdS/ZnS quantum structures. *Phys.Rev.B*, 61:12632, 2000. 48, 61, 72
- [111] W. Langbein et.al. Localization-enhanced biexciton binding in semiconductors. *Phys.Rev.B*, 59:15405, 1999. 48

REFERENCES

- [112] J. Tulkki et.al. Confinement effect in a quantum well dot induced by an InP stressor. *Phys.Rev.B*, 52:8239, 1995. 48
- [113] J. M. Garcia et.al. Intermixing and shape changes during the formation of InAs self-assembled quantum dots. *Appl. Phys. Lett.*, 71:2014, 1997. 48
- [114] N. Liu et.al. Nonuniform Composition Profile in In_{0.5}Ga_{0.5}As Alloy Quantum Dots. *Phys.Rev.Lett.*, 84:334, 2000. 48
- [115] S. V. Nair. *Semiconductor Quantum Dots: Physics, Spectroscopy and Applications*. Springer-Verlag, Berlin, 2002. 48
- [116] L. Banyai. *Semiconductor Quantum Dots*. World Scientific, 1993. 48
- [117] H.Htoon et.al. Anomalous Circular Polarization of Photoluminescence Spectra of Individual CdSe Nanocrystals in an Applied Magnetic Field. *Phys. Rev. Lett.*, 102:017402, 2009. 48, 50, 63, 84
- [118] H. Htoon et.al. Linearly polarized fine structure "V" of the bright exciton state in individual CdSe nanocrystal quantum dots. *Phys.Rev. B*, 77:035328, 2008. 48, 50, 63
- [119] Luis G. G. V. Dias da Silva et.al. Polarization and Aharonov-Bohm oscillations in quantum-ring magnetoexcitons. *Phys.Rev.B*, 72:125327, 2005. 48
- [120] T. M. Hsu et.al. Quantum-confined Stark shift in electroreflectance of InAs/In_xGa_{1-x}As self-assembled quantum dots. *Appl. Phys. Lett.*, 78:1760, 2001. 48
- [121] S. A. Empedocles et.al. Quantum-Confined Stark Effect in Single CdSe Nanocrystallite Quantum Dots. *Science*, 278:2114, 1997. 48
- [122] I. Kegel et.al. Nanometer-Scale Resolution of Strain and Interdiffusion in Self-Assembled InAs/GaAs Quantum Dots. *Phys.Rev.Lett.*, 85:1694, 2000. 48
- [123] X. Li et.al. An All-Optical Quantum Gate in a Semiconductor Quantum Dot. *Science*, 301:809, 2003. 48

-
- [124] I. Favero et. al. Fast exciton spin relaxation in single quantum dots. *Phys. Rev. B*, 71:233304, 2005. 50, 52
- [125] D.P. DiVincenzo et.al. Quantum Computation. *Science*, 270:255, 1995. 50
- [126] Al. L. Efros et.al. Band-edge exciton in quantum dots of semiconductors with a degenerate valence band: Dark and bright exciton states. *Phys.Rev.B*, 54:4843, 1996. 50
- [127] Michio Ikezawa et.al. Biexciton binding energy in parabolic GaAs quantum dots. *Phys. Rev. B*, 73:125321, 2006. 50
- [128] Jun-Wei Luo et.al. Geometry of epitaxial GaAs/(Al,Ga)As quantum dots as seen by excitonic spectroscopy. *Phys. Rev. B*, 84:235317, 2011. 50
- [129] M. P. Nowak et.al. Spin-orbit coupling effects in two-dimensional circular quantum rings: Elliptical deformation of confined electron density. *Phys.Rev.B*, 80:195319, 2009. 50
- [130] H. Giessen et.al. Femtosecond optical gain in strongly confined quantum dots. *Opt. Lett.*, 21:1043, 1996. 50
- [131] J. Hours et.al. Exciton radiative lifetime controlled by the lateral confinement energy in a single quantum dot. *Phys. Rev. B*, 71:161306, 2005. 52
- [132] C. Santori et.al. Time-resolved spectroscopy of multiexcitonic decay in an InAs quantum dot. *Phys.Rev.B*, 65:073310, 2002. 55
- [133] G. Bacher et.al. Biexciton versus Exciton Lifetime in a Single Semiconductor Quantum Dot. *Phys.Rev.Lett.*, 83:4417, 1999. 55, 73
- [134] S. Pedersen et.al. Observation of quantum asymmetry in an Aharonov-Bohm ring. *Phys.Rev.B*, 61:5457, 2000. 55
- [135] F. Findeis et.al. Photocurrent and photoluminescence of a single self-assembled quantum dot in electric fields. *Appl. Phys. Lett.*, 78:2958, 2001. 57
- [136] E. Bucks et.al. Dephasing in electron interference by a 'which-path' detector. *Nature*, 391:871, 1998. 57

REFERENCES

- [137] R. A. Webb et.al. Observation of h/e Aharonov-Bohm Oscillations in Normal-Metal Rings. *Phys.Rev.Lett.*, 54:2696, 1985. 57
- [138] P.Borri et.al. Well-width dependence of exciton-phonon scattering in $\text{In}_x\text{Ga}_{1-x}\text{As}/\text{GaAs}$ single quantum wells. *Phys.Rev.B*, 59:2215, 1999. 57
- [139] I. A. Yugova et.al. Exciton fine structure in $\text{InGaAs}/\text{GaAs}$ quantum dots revisited by pump-probe Faraday rotation. *Phys.Rev.B*, 75:195325, 2007. 57
- [140] D. Gammon et.al. Fine Structure Splitting in the Optical Spectra of Single GaAs Quantum Dots. *Phys.Rev.Lett.*, 76:3005, 1996. 57
- [141] Adam Babinski et.al. Single-dot spectroscopy in high magnetic fields. *Physica E*, 26:190, 2005. 59
- [142] Ming-Fu Tsai et.al. Diamagnetic Response of Exciton Complexes in Semiconductor Quantum Dots. *Phys.Rev.Lett.*, 101:267402, 2008. 59
- [143] R. J. Young et.al. Inversion of exciton level splitting in quantum dots. *Phys.Rev.B*, 72:113305, 2005. 59
- [144] J. J. Finley et.al. Fine structure of charged and neutral excitons in $\text{InAs}_{10.6}\text{Ga}_{0.4}\text{As}$ quantum dots. *Phys.Rev.B*, 66:153316, 2002. 59
- [145] E. L. Ivchenko et.al. Fine Structure of Excitonic Levels in Semiconductor Nanostructures. *Phys.Status Solidi A*, 164:487, 1997. 59
- [146] J. A. Gupta et.al. Spin coherence in semiconductor quantum dots. *Phys.Rev.B*, 59:10421, 1999. 59
- [147] M. Bayer et.al. Spectroscopic study of dark excitons in $\text{In}_x\text{Ga}_{1-x}\text{As}$ self-assembled quantum dots by a magnetic-field-induced symmetry breaking. *Phys.Rev.B*, 61:7273, 2000. 59
- [148] F. Kreller et.al. Role of Biexcitons in the Stimulated Emission of Wide-Gap II-VI Quantum Wells. *Phys.Rev.Lett.*, 75:2420, 1995. 59
- [149] T. F. Albrecht et.al. Disorder mediated biexcitonic beats in semiconductor quantum wells. *Phys.Rev.B*, 54:4436, 1996. 59

-
- [150] T. Baars et.al. Biexcitons in In_xGa_{1-x}As/GaAs quantum wells subject to high magnetic fields. *Phys.Rev.B*, 63:153312, 2001. 59
- [151] M. Casse et.al. Temperature dependence of the Aharonov-Bohm oscillations and the energy spectrum in a single-mode ballistic ring. *Phys.Rev.B*, 62:2624, 2000. 63
- [152] P. F. Gomes et.al. Exciton binding energy in type II quantum dots. *Phys.stat.sol(c)*, 2:385, 2007. 63
- [153] M.Gurioli et.al. Recombination kinetics of InAs quantum dots: Role of thermalization in dark states. *Phys.Rev.B*, 73:085302, 2006. 63
- [154] Z.Y.Xu et.al. Carrier relaxation and thermal activation of localized excitons in self-organized InAs multilayers grown on GaAs substrates. *Phys.Rev.B*, 54:11528, 1996. 63
- [155] S.Logothetidis et.al. Temperature dependence of the dielectric function and the interband critical points of CdSe. *Phys.Rev.B*, 34:2458, 1986. 67
- [156] Klimov V I et.al. Quantization of Multiparticle Auger Rates in Semiconductor Quantum Dots. *Science*, 287:1011, 2000. 69, 97
- [157] W. Langbein et.al. Control of fine-structure splitting and biexciton binding in In_xGa_{1-x}As quantum dots by annealing. *Phys.Rev.B*, 69:161301, 2004. 71
- [158] A. V. Filinov et.al. Influence of well-width fluctuations on the binding energy of excitons, charged excitons, and biexcitons in GaAs-based quantum wells. *Phys.Rev.B*, 70:035323, 2004. 71
- [159] L. Besombes et.al. Exciton and Biexciton Fine Structure in Single Elongated Islands Grown on a Vicinal Surface. *Phys.Rev.Lett.*, 85:425, 2000. 71
- [160] M. Bayer et.al. Electron and Hole g Factors and Exchange Interaction from Studies of the Exciton Fine Structure in In_{0.60}Ga_{0.40}As Quantum Dots. *Phys.Rev.Lett.*, 82:1748, 1999. 71
- [161] J. Puls et.al. Magneto-optical study of the exciton fine structure in self-assembled CdSe quantum dots. *Phys.Rev.B*, 60:16303, 1999. 71

REFERENCES

- [162] S. Corni et.al. Size dependence of the electron-hole recombination rates in semiconductor quantum dots. *Phys.Rev.B*, 67:045313, 2003. 71
- [163] R. Seguin et.al. Size-Dependent Fine-Structure Splitting in Self-Organized InAs/GaAs Quantum Dots. *Phys.Rev.Lett.*, 95:257402, 2005. 71
- [164] J.H. Rice et.al. Biexciton and exciton dynamics in single InGaN quantum dots. *Nanotechnology*, 16:1477, 2005. 73
- [165] D. J. Norris et.al. Size dependence of exciton fine structure in CdSe quantum dots. *Phys.Rev.B*, 53:16347, 1996. 79
- [166] Griffiths.D.J. *Introduction to quantum mechanics*. Prentice Hall, 1995. 82
- [167] M. S. Kushwaha et.al. Magneto-optics of single Rashba spintronic quantum dots subjected to a perpendicular magnetic field: Fundamentals. *J. Appl.Phys*, 104:083714, 2008. 81
- [168] O. Kalman et.al. Magnetoconductance of rectangular arrays of quantum rings. *Phys.Rev.B*, 78:125306, 2008. 81
- [169] L. R. Sellers et.al. Aharonov-Bohm Excitons at Elevated Temperatures in Type-II ZnTe/ZnSe Quantum Dots. *Phys.Rev.Lett.*, 100:136405, 2008. 81
- [170] F. Ding et.al. Gate controlled Aharonov-Bohm-type oscillations from single neutral excitons in quantum rings. *Phys.Rev.B*, 82:075309, 2010. 81
- [171] M. D. Teodoro et.al. Aharonov-Bohm Interference in Neutral Excitons: Effects of Built-In Electric Fields. *Phys.Rev.Lett.*, 104:086401, 2010. 81
- [172] M.J.M. Daenen. Wondrous World of Carbon Nanotubes. *Online webpage*, 2003. 88, 89
- [173] Sumio Iijima. Helical microtubules of graphitic carbon. *Nature*, 354:56, 1991. 87
- [174] R. Bruce Weisman. Carbon nanotubes. *The Electrochemical Society Interface*, page 42, 2006. 89
- [175] C. Galland et.al. Non-Markovian Decoherence of Localized Nanotube Excitons by Acoustic Phonons. *Phys.Rev.Lett.*, 101:067402, 2008. 95

-
- [176] V. Perebeinos et.al. Radiative Lifetime of Excitons in Carbon Nanotubes. *Nano Lett.*, 5:2495, 2005. 95
- [177] A. Hogele et.al. Photon Antibunching in the Photoluminescence Spectra of a Single Carbon Nanotube. *Phys.Rev.Lett.*, 100:217401, 2008. 95
- [178] P.L.McEuen et.al. Disorder, Pseudospins, and Backscattering in Carbon Nanotubes. *Phys.Rev.Lett.*, 83:5098, 1999. 95
- [179] G. D. Scholes et.al. Nanocrystal Shape and the Mechanism of Exciton Spin Relaxation. *Nano Lett.*, 6:1765, 2006. 97
- [180] Paul Alivisatos. The use of nanocrystals in biological detection. *Nature Biotech.*, 22:47, 2004. 97
- [181] Klimov V I et.al. Optical gain and stimulated emission in nanocrystal quantum dots. *Science*, 290:314, 2000. 97
- [182] Mikhailovsky A A et.al. Multiparticle interactions and stimulated emission in chemically synthesized quantum dots. *Appl. Phys. Lett.*, 80:2380, 2002. 97
- [183] Sudhanshu srivastava. Composite Layer-by-Layer (LBL) Assembly with Inorganic Nanoparticles and Nanowires. *Accounts of chemical research*, 41:1831, 2008. 98
- [184] R. H. Ritchie. Plasma Losses by Fast Electrons in Thin Films. *Phys.Rev.*, 106:874, 1957. 99
- [185] William L. Barnes et.al. Surface plasmon subwavelength optics. *Nature*, 424:824, 2003. 100, 101
- [186] Jaebeom Lee et.al. Exciton-plasmon interactions in molecular spring assemblies of nanowires and wavelength-based protein detection. *Nat. Mater.*, 6:291, 2007. 101
- [187] Seonghoon Kim et.al. Photoluminescence Up-Conversion of Bioconjugated Hybrids on CdTe and Au Nanoparticles. *Journal of Nanoscience and nanotechnology*, 9:7061, 2009. 102

REFERENCES

- [188] E. Dekel et.al. Multiexciton Spectroscopy of a Single Self-Assembled Quantum Dot. *Phys.Rev.Lett.*, 80:4991, 1998. 103
- [189] A. Kiraz et.al. Photon correlation spectroscopy of a single quantum dot. *Phys.Rev.B*, 65:161303, 2002. 103
- [190] D. Magana et.al. Perturbation of the magneto-optical properties of nanocrystalline CdSSe. *Phys.Rev.B*, 77:115337, 2008. 104
- [191] P. Chen et.al. Magneto-optical response of CdSe nanostructures. *Phys.Rev.B*, 70:045311, 2004. 104
- [192] M. Bayer et.al. Optical Detection of the Aharonov-Bohm Effect on a Charged Particle in a Nanoscale Quantum Ring. *Phys.Rev.Lett.*, 90:186801, 2003. 104
- [193] P. Pietilainen et.al. Energy levels and magneto-optical transitions in parabolic quantum dots with spin-orbit coupling. *Phys.Rev.B*, 73:155315, 2006. 104
- [194] G. Timp et.al. Observation of the Aharonov-Bohm effect for $\omega_c T > 1$. *Phys.Rev.Lett.*, 58:2814, 1987. 104
- [195] Ta-Chun Lin et.al. Impacts of structural asymmetry on the magnetic response of excitons and biexcitons in single self-assembled In(Ga)As quantum rings. *Phys.Rev.B*, 80:081304, 2009. 104
- [196] N. J. Traynor et.al. Zeeman splitting and g factor of heavy-hole excitons in In_xGa_{1-x}As/GaAs quantum wells. *Phys.Rev.B*, 51:7361, 1995. 104
- [197] R. Kotlyar et.al. Zeeman spin splittings in semiconductor nanostructures. *Phys.Rev.B*, 63:085310, 2001. 104
- [198] B. Szafran et.al. Selective suppression of Dresselhaus or Rashba spin-orbit coupling effects by the Zeeman interaction in quantum dots. *Phys.Rev.B*, 79:235303, 2009. 104